Optically addressing semiconductor electron-spin ensembles with tunable nuclear-spin environments

de Jong, Jakko Pieter

Optically addressing semiconductor electron-spin ensembles with tunable nuclear-spin environments

university of groningen

zernike institute for advanced materials

European Research Council
Established by the European Commission

Zernike Institute PhD thesis series 2016-17
ISSN: 1570-1530
ISBN: 978-90-367-8894-6 (printed version)
ISBN: 978-90-367-8893-9 (electronic version)

The work described in this thesis was performed in the research group Physics of Nanodevices of the Zernike Institute for Advanced Materials at the University of Groningen, the Netherlands. The project was funded by the European Research Council via ERC Starting Grant 279931. The project did profit from facilities funded through the Dutch national NanoLabNL initiative, and from collaboration with projects funded via the research programmes of the Dutch Foundation for Fundamental Research on Matter (FOM) and the Netherlands Organisation for Scientific Research (NWO).

Thesis cover design: J. P. de Jong

Printed by Ipskamp Drukkers, Enschede

university of groningen

Optically addressing semiconductor electron-spin ensembles with tunable nuclear-spin environments

PhD thesis

to obtain the degree of PhD at the
University of Groningen
on the authority of the
Rector Magnificus Prof. E. Sterken
and in accordance with
the decision by the College of Deans.

This thesis will be defended in public on

Friday 16 September 2016 at 14.30 hours

by

Jakko Pieter de Jong

born on 18 May 1986
in Deventer, the Netherlands

Supervisor
Prof. C. H. van der Wal

Assessment committee
Prof. R. A. Hoekstra
Prof. P. W. H. Pinkse
Prof. M. Atatüre

Contents

Chapter 1

Introduction –
Coherent electron-spin ensembles in inhomogeneous environments

1.1 Quantum information

We live in a curious age. One and a half centuries ago, physics was thought to be almost completely understood, when Max Planck and Albert Einstein came up with explanations for two last unsolved mysteries of physics: black-body radiation and the photoelectric effect. During the first decades of the twentieth century, however, their theories gave rise to the development of a new paradigm in physics that became *quantum mechanics*. Quantum mechanics changed everything in physics: Light, proven to be a wave in 1801 with experiments by Thomas Young, was predicted to consist out of indivisible particles called *photons*. On the other hand, atoms, named after the ancient Greek word for 'indivisible', suddenly were shown to have a wave-character as well by De Broglie. One of the consequences of quantum mechanics was the phenomenon *entanglement*, where the physical properties of two objects are intertwined to such an extent that their states cannot be described independently anymore. The consequences of entanglement, which has no classical counterpart, were so counter-intuitive and paradoxical that it led even one of the founding fathers (Einstein) to doubt the completeness of quantum mechanics [1], leading to the so-called Einstein-Podolsky-Rosen paradox. Decades later, Bell defined a sharp criterion for testing the validity of the predictions of quantum mechanics [2] and Bohm and Aharonov proposed experiments to resolve the paradox using entangled photons [3]. In chronological order, cryogenics, laser physics, nano-imaging and nano-fabrication provided tools to not only validate the consequences of quantum mechanics, but to manufacture quantum systems with desired properties and their mutual interaction and their coupling to the environment to create quantum devices. Over the years, quantum mechanics has been thoroughly tested in many experiments (note for example the work by Alain Aspect [4]) and the counter-intuitive implications of entanglement have been validated [5].

Simultaneously, advances in the development of semiconductor materials and the invention of the transistor effect at Bell labs gave rise to the birth of modern electronics and the first electrical computer (a mechanical steam-powered computer was already designed by Charles Babbage in 1821). Electrical computing uses physical properties of materials (i.e. stored charge, electric currents, small magnetic moments, etc.) to represent units of information and to perform operations on this information. After initial diversity in the physical representation of information (see for example ternary computing, that uses trits with three values instead of bits), the world settled on the use of the smallest unit of information with two values (0 and 1), known today as the *bit*. The notion that information is, much like energy and momentum, a fundamental property of nature gave rise to the field of information science, which developed the laws to quantify information, relate it to energy and entropy, i.e. treat it physically.

The coming of quantum mechanics made it even more obvious that information is a key parameter in nature, for it created questions as: 'How many quantum numbers describe all information of a quantum state?', 'With what fundamental precision do observables have a certain value?' and 'What happens if we measure (extract information from) a quantum system?'. When scientists started to recognize that quantum mechanics could potentially revolutionize the way we transport information, *quantum information science* was born [6].

The fundamental unit of information in quantum mechanics, the *qubit*, consists of two states, represented by the physical eigenstates of a quantum system, like its classical counterpart the bit. Unlike the bit, which attains either of its two values, the qubit can exist in both states at the same time, called a *superposition*. This property, and the entanglement of two or more qubits, makes quantum information very promising for a couple of new technologies: quantum sensors with increased sensitivity as compared to classical sensors, quantum communication for hundred percent secure transport of information over distance and the quantum computer that promises to perform certain algorithms orders of magnitude faster than current computers, possibly at a fraction of the energy.

The majority of quantum information applications requires the combination of the local temporary storage of quantum information in *quantum memory* and the communication of information over distance using *flying qubits*. The properties of photons make them ideal for information transport (we will get back to that in a minute), but it is challenging to store them locally in a way that provides on demand manipulation. Hence, for quantum memory applications, matter degrees of freedom are often preferred. Candidates for the storage and manipulation of quantum information in matter have become numerous: The eigenstates of individual trapped ions [7] or atomic clouds [8, 9], the sign or the phase of superconducting currents in Josephson junctions [10], the spin states of localized particles [11] in gated quantum dots [12], self-assembled quantum dots [13, 14] and defects [15, 16] and impurities [17, 18] in semiconductor host lattices. This list is neither exhaustive, nor does it credit all the contributors to this broad field.

Two matter qubits can interact directly by placing them so close together that their wavefunctions overlap. However, increasing the number of qubits in a network requires distant mediation between nodes. While techniques exist that transport quantum information without the use of light, by moving coherent spins electrically through a semiconductor [19], inductive coupling via a quantum bus with Josephson junctions [20] or by capacitive coupling between quantum dots [21], it is hard to ignore optical photons as the ideal candidate for the scale-up of quantum networks beyond a couple of qubits and transport over distances longer than micrometers. Besides being the fastest mediator between distant matter qubits, photons have low interaction with the environment and hence long coherence times.

1.2 Why use ensembles in solid-state?

A few years ago, the author of this thesis got the pleasure to speak with David DiVincenzo, who proposed the use of electron spins as qubits for quantum computing [11]. When asked which system would likely yield the first reliable commercial quantum computer, he answered that above all it would prove important to study a wide variety of quantum systems with diverse advantages, to be prepared for unforeseen but inevitable future problems. The robustness and scalability of quantum optics using solid-state ensembles makes them a very interesting topic of research, despite their difficulties, as we will try to explain in the next paragraphs.

As mentioned above, photons can mediate coherent interaction between matter quantum systems. The low interaction of the degrees of freedom of a photon field with its environment provides a fast and robust way of quantum information transport over distance. This weak interaction with matter becomes problematic for the deterministic exchange of information between a photon and a matter qubit. A main requirement for reliable quantum optical applications is deterministic interaction between light and matter: the probability that a single photon exchanges information with a matter quantum system should be close to unity for reproducible behavior of a quantum optical device. Therefore, a central theme in quantum optics is the tailoring of light-matter interactions. This is generally achieved in two ways, and the combination of these:

1, Increase the electromagnetic field amplitude at the quantum system. This is not as simple as increasing the intensity of the light source: while increasing the number of photons in a field will higher the probability that one of them will interact with the matter system, it does not improve the interaction efficiency for a single photon (it might even decrease when the number of photons is high enough). Instead, each photon has to pass the quantum system multiple times from a particle point of view or, in a wave description, the local intensity of the field has to be enhanced by creating a standing wave. This is realized by placing the quantum system in or close to an optical cavity with reflective boundaries, designed to exhibit optical modes with highly increased field amplitudes that overlap spectrally and spatially with the quantum system. Cavity quantum electrodynamics, pioneered by Haroche [22] and Wineland [23], has yielded many cavities and resonators for optical quantum systems of both atomic [24, 25, 26] and solid-state nature [27, 28, 29], increasing the light-matter interaction by many orders of magnitude. To be complete, we note that electromagnetic fields can also be strongly enhanced locally via the use of plasmon nano-antenna's.

2, Use a spatial ensemble of N identical matter quantum systems. These systems will interact with passing photons as a single collective mesoscopic system, and the light-matter coupling is increased $\sqrt{N}$-fold as compared to the case of a single quantum system [30]. The absorption of a single photon by an ensemble of quantum systems does not simply result in one of the systems absorbing the photon. Rather, the ensemble absorbs the photon collectively, which results in a coherent superposition of absorption by individual ensemble members. This is illustrated for a tiny ensemble of three identical two-level systems in figure 1.1 and equations 1.1 and 1.2. Figure 1.1 schematically shows the situation before absorption of a single photon, with 1 photon in the optical field and the matter system in its ground-state with all three systems in $|a\rangle$, as represented by equation 1.1. Then, the photon interacts coherently with the ensemble, resulting in a delocalized absorption that leaves the optical field empty and the ensemble in a collective excited mode, as represented by equation 1.2.

$$|\Phi\rangle_{before} = \ |1\rangle_{photon} |a_1 a_2 a_3\rangle \tag{1.1}$$

$$|\Phi\rangle_{after} = \ c_1 |0\rangle_{photon} |b_1 a_2 a_3\rangle + c_2 |0\rangle_{photon} |a_1 b_2 a_3\rangle + c_3 |0\rangle_{photon} |a_1 a_2 b_3\rangle \tag{1.2}$$

Re-emission of photons from these kind of coherent ensembles have a big advantage over single point-emitters: they emit in a certain direction instead of omni-directionally, due to the phase-matching necessary for the ensemble to collectively emit a photon [30, 31, 32]. In practice this will reduce the loss of emitted photons in the experimental setup, which increases detection and enables further use of the photons. Single emitters also emit directional when placed in optical

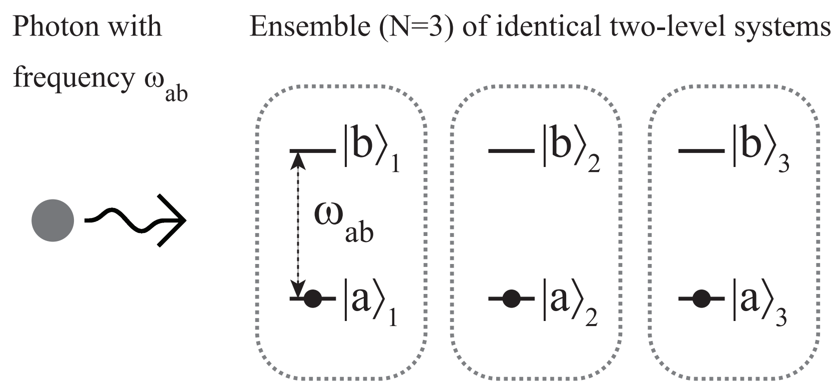

Figure 1.1: An ensemble of three identical two-level systems with transition energy $\hbar\omega_{ab}$ and an incident photon before interaction. All two-level systems are in their ground state $|a\rangle$

cavities, but this is technically very demanding. The simplicity and robustness of (quantum) ensembles makes them an interesting topic of research, especially for feasible upscaling of device fabrication with existing industrial semiconductor-processing.

Feasible upscaling is also the most important reason to use solid-state devices for quantum storage. While atomic gases and trapped ions are naturally coherent systems due to their isolated nature, controlling them requires vacuum containers, vapor cells, laser traps or other macroscopic setups. Although of prime importance for studying the fundamental laws of nature and the expansion of scientific knowledge, this limits the scalability of potential quantum applications. On the contrary, solid-state systems open the way for one of the holy grails of quantum optics: a quantum optical device fully integrated on a chip, including the emission, manipulation and detection of single photons. Optical waveguides can keep photons confined on the chip and transport them between matter qubits. The fabrication of defects or impurity ensembles in semiconductors can be incorporated in the growth of semiconductor wafers. For ensembles, besides the fabrication of waveguides, no further fabrication steps are necessary to tune the light-matter interaction or the directionality of emission.

Coherent storage and retrieval of photon states in ensembles has been performed in atomic ensembles [9, 33], and macroscopic-scale non-local entanglement between two separated rubidium clouds was demonstrated [34]. For solid-state, storage of photon states using ensembles has been demonstrated in rare-earth ion doped crystals [35, 36] and only recently was this storage taken to the single photon level [37].

1.3 Aim of this thesis research

As illustrated with some examples above, groundbreaking experiments have been performed that use the entanglement of a few qubits for quantum information applications. However, it is still an open question whether vast networks of connected qubits can be practically realized and in what material system. We aim to contribute to the ongoing search for the ideal material, physical degrees of freedom and control strategies for quantum memory. Our goal is to address one of the fundamental questions for quantum systems in solid-state: What determines the coherence time for our system and to what extent can we control its environment to enhance this coherence time? We explore control strategies that can be applied to a variety of material systems, and study these strategies using ensembles of localized electrons in GaAs. GaAs was a suitable system for first experiments, given that it is well characterized and can be grown with very high quality.

As mentioned above, coherent ensembles consist of identical systems. *Identical* is a key word here and reveals the largest disadvantage of ensembles. The quality of a quantum memory is measured by its dephasing time, i.e. the time it can store quantum information before interactions with the environment randomize the phase of the coherent superposition. Single quantum systems dephase because of temporal fluctuations in their environment due to lattice vibrations, electric and magnetic noise, etc. When using an ensemble of these systems collectively, additional dephasing occurs due to spatial inhomogeneities in the material.

In this thesis, we study ensembles of localized electron spins in an insulating gallium arsenide host lattice, bound at silicon impurities that are very shallow dopants. These donor-bound electrons (D^0) have spin $S = 1/2$, with two spin eigenstates that serve as the qubit. These spin states have optical transitions to a common excited state, formed by a donor-bound trion (D^0X, an additional electron-hole pair bound at the D^0 site), providing optical control over the electron spin. Since GaAs can be grown extremely pure and with a very low level of (unintended) defects, the inhomogeneous linewidth of these optical transitions is very narrow at about ten gigahertz. Furthermore, phonon-sidebands are negligible for the D^0-D^0X transitions due to the nature of the confinement and the size of the D^0 and D^0X wavefunctions. However, GaAs has a major setback that deteriorates the coherence of localized spins: both gallium and arsenide atoms have a non-zero nuclear spin. The orientation of these spins show random thermal fluctuations and, via the hyperfine interaction, are the dominant dephasing mechanism for localized electron-spins in GaAs, and reduce the inhomogeneous dephasing time of a bound-electron spin ensemble to a mere 2 nanoseconds.

Numerous techniques have been developed to suppress the nuclear spin fluctuations in semiconductors or to decouple localized spins from the nuclear spin bath. Experiments using microwave spin-echo techniques to decouple electron spins in gallium arsenide quantum dots from dephasing by the nuclear-spin have shown that the intrinsic homogeneous dephasing time of localized electron-spins in GaAs is around a millisecond. However, spin-echo techniques require complicated microwave pulse sequences, during which no other operations can be performed. On top of that, it is extremely challenging to perform on ensembles.

We design and demonstrate a fully optical two-laser technique to control the nuclear-spin in GaAs via the hyperfine interaction with an ensemble of localized D^0 electrons. Our approach does not rely on decoupling from spin noise, but focuses on reducing fluctuations in the nuclear-spin to enhance the dephasing time of localized electron-spins. The feedback scheme, that is self-improving and requires no active correction besides laser-intensity and laser-frequency stabilization, uses the sharp spectral two-photon phenomenon known as *coherent population trapping* (CPT) [38]. We use *dynamic nuclear polarization* (DNP) around CPT conditions to stabilize the nuclear spin in a configuration with either one or two stable points, depending on the sign of laser detuning from the optical transitions. A similar technique was applied by Xu and Sun *et al.* [39, 40] to self-assembled InAs quantum dots in GaAs, and yielded increased dephasing times of more than a microsecond for a single localized electron. Xu and Sun report a dominant role for the excited-state hole spin in DNP with InAs quantum dots. In our case, we show that electron-nuclear spin flip-flops are the dominant contribution to DNP. Our method is able to resolve the dominant contribution to DNP by looking at the number of stable points with laser detuning (chapter 3).

Note that while we apply our two-laser technique on an ensemble of localized electron-spins in GaAs, it is applicable to a wide range of quantum systems in semiconductor materials with non-zero nuclear-spin.

Non-uniformities in the laser field present a challenge for addressing ensembles, when the spatial dimensions of the ensemble are larger than the laser wavelength. For epilayer devices (and to some extent also for optical waveguides), reflections inside the semiconductor host layer cause spatial variations of the laser intensity. Further, in dispersive materials, the intensity patterns for two lasers with different wavelength do not overlap in general. On top of this, laser fields generally have a non-uniform transverse intensity profile. The above yields a non-uniform distribution of laser intensities driving the ensemble dynamics, which complicates the light-ensemble coupling, and compromises our two-laser feedback technique. We analyze in detail how non-uniform laser intensities arise and study their effect on the suppression of nuclear-spin fluctuations. We discuss how the uniformity of laser intensity throughout the ensemble can be improved and show our progression in this regard.

The research for this thesis was performed in close collaboration with Alexander Onur [41], who provided a large part of the theoretical framework. While this thesis is written to be self-contained, we want to focus the attention of the reader to reference [42], where the theory behind our two-laser feedback technique is explained in more detail.

1.4 Outline of this thesis

Chapter 2 provides a concise introduction into the basic concepts necessary to understand this thesis. First, the energy-level structure of the D^0-D^0X system is presented. Then, we introduce the non-linear optical effect of coherent population trapping (CPT), used for coherent optical manipulation of the bound-electron spin. Finally, we treat the hyperfine interaction of the bound electrons with the surrounding nuclear spin bath. We show how the hyperfine interaction can be used to optically polarize the nuclear spin, a process known as dynamic nuclear polarization (DNP).

Chapter 3 presents a two-laser feedback technique that combines CPT and DNP to optically control the nuclear spin in hyperfine contact with an ensemble of the localized electrons in GaAs. We use this technique to stabilize the distribution of nuclear-spin polarization in a non-thermal split configuration that is reflected in the CPT lineshape in transmission experiments. We study the role of the Knight field in the decoupling of nuclear spins around bound electrons from the bulk nuclear-spin bath, by monitoring the relaxation of the split CPT lineshape over time.

Chapter 4 builds on the two-laser technique described in chapter 3, and shows experimental results of DNP feedback at CPT condition to suppress nuclear-spin fluctuations around an ensemble of donor-bound electrons, effectively enhancing the inhomogeneous electron-spin dephasing time T_2^* by a factor 2. We describe how Fabry-Perot effects yield standing waves inside epilayer GaAs and we simulate how non-uniform laser fields throughout the ensemble of bound electrons compromise our two-laser feedback and prevent a further increase in dephasing time. We also analyze the prospects for better dephasing times when the uniformity of the laser field is technically improved.

In order to suppress nuclear-spin fluctuations as described in chapter 3 and 4, an ensemble of electron-spins in a homogeneous strain environment and uniform laser field is required. **Chapter 5** describes how optical characterization and careful fabrication of GaAs epilayers on sapphire can improve uniform addressing of an ensemble of optical impurities in a semiconductor epilayer. We demonstrate correlations between optical microscope images at room temperature and spatial laser scans at cryogenic temperatures for the analysis of strain homogeneity throughout the GaAs layer. We simulate and measure the effect of anti-reflection coatings on the uniformity of optical fields inside the GaAs epilayer. We provide fabrication techniques to make optical apertures on top of the sample, to shape the Gaussian intensity profiles of laser beams into top-hat profiles.

Chapter 6 provides an in-depth analysis of the measurement technique called *differential transmission spectroscopy (DTS)*, used to perform spectroscopy with high resolution on (among others) the donor-bound exciton complex in GaAs. Although similar techniques have been used to perform detailed spectroscopy for decades, we found surprisingly little literature that presents a detailed signal analysis to explain its strengths and flaws, and therefore present an analysis of the measurement signal in considerable depth here. We simulate the use of DTS on four-level-systems and compare the results with our experimental spectroscopy on donor-bound electrons.

Chapter 2

Optical manipulation of localized electron spins and nuclear spins in GaAs

Abstract

In this chapter we introduce basic concepts necessary to understand this thesis. We present the energy-level structure of the D^0-D^0X system and show how it gives rise to the two-photon resonance known as coherent population trapping (CPT). CPT is used for coherent optical manipulation of the bound-electron spin, and as a probe of the electron-spin ensemble inhomogeneous broadening. We explain the hyperfine interaction of the bound electrons with the surrounding nuclear spin bath and show how it is used to optically polarize the nuclear spin in a process known as dynamic nuclear spin polarization (DNP). Experimental CPT traces are used to monitor the nuclear spin polarization, and show an Overhauser shift of 500 megahertz after DNP. Finally, we discuss the relaxation of nuclear spin polarization at the bound electrons by nuclear-spin diffusion.

2.1 Optical control of D^0-D^0X in GaAs

This thesis treats the optical manipulation of ensembles of donor-bound electrons in gallium arsenide. The bound electrons are provided by silicon atoms that substitute gallium atoms in the semiconductor lattice. At temperatures below the ionization temperature of $\approx$ 70 K, the donor electron becomes localized at the silicon atom, resulting in a neutral donor atom (D^0) that can be viewed as an artificial hydrogen atom. The ground state of D^0 resembles the 1s atomic orbit and consists of two spin states. Multiple excited states are provided by a donor-bound trion (D^0X, an additional electron-hole pair bound at the D^0 site).

Figure 2.1 shows a schematic picture of the D^0-D^0X level structure. The excited state levels that are lowest in energy consist of two electron spins in a singlet and a hole spin. Because of the spin-orbit interaction in GaAs, these excited states have allowed optical transitions to both spin ground-states. Since GaAs can be grown extremely pure and with a very low level of (unintended) defects, the inhomogeneous linewidth of these optical transitions is narrow at about ten gigahertz. Furthermore, phonon sidebands are negligible for the D^0-D^0X transitions due to the nature of the confinement and the size ($\approx$ 10 nm) of the D^0 and D^0X wavefunctions. Throughout this thesis, we address the optical transitions to the lowest excited state, unless otherwise specified.

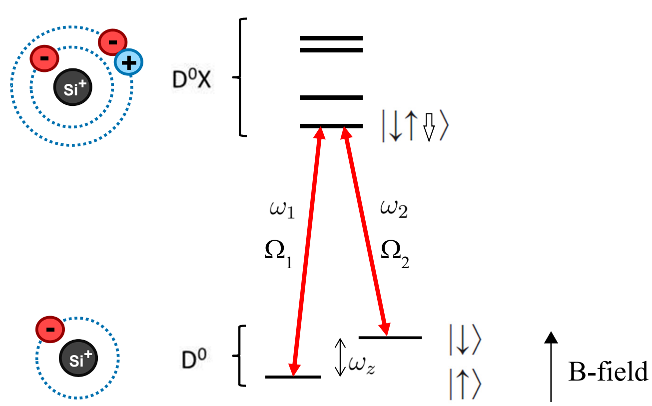

Figure 2.1: Schematic view of the lambda energy level system. The ground state (D^0) consists of a single donor-bound electron in a 1s-like orbital, split into two degenerate spin states by an external magnetic field. A bound trion provides excited states with optical transitions to both ground states. The transitions to the lowest excited state have transition frequency ω_1 and ω_2, and the coupling strength of the laser fields with the transitions is depicted by the Rabi frequency Ω_1 and Ω_2.

The two ground states and the excited state form a Λ-level system. Because the excited state has optical transitions with both ground states, optical orientation of the ground-state spin can take place at rates much faster than the relaxation rate of the electron spin. In an applied external magnetic field, the spin levels of the ground state are Zeeman-split, and the transitions from both spin states become spectrally selective (see ω_1 and ω_2 in figure 2.1).

2.2 Coherent population trapping

If the ground-state coherence time is sufficiently long-lived, Λ level systems give rise to a non-linear two-photon resonance known as electromagnetically induced transparency (EIT) [17, 18, 38]. EIT occurs as a narrow frequency window of increased transmission when the difference frequency of two laser fields corresponds to the ground-state splitting. Figure 2.2 shows two-laser transmission scans, where one laser is fixed resonantly with frequency ω_2, and the other laser's frequency is scanned around ω_1. The scans show a broad single photon absorption with a linewidth of approximately 10 GHz. A narrow peak occurs at two-photon resonance, where single photon absorption is suppressed (hence the increased transmission) and the material system is trapped in a coherent superposition of the two spin states:

$$|\Psi\rangle = \frac{\Omega_1 |\downarrow\rangle - \Omega_2 |\uparrow\rangle}{\sqrt{\Omega_1^2 + \Omega_2^2}} \tag{2.1}$$

This controlled trapping is known as coherent population trapping (CPT). Figure 2.2a shows a trace obtained with differential transmission spectroscopy where one of the laser fields was modulated to enhance the visibility of the optical transition. As motivated in chapter 6, this technique provides a distorted view of the height of spectroscopic features. To determine the increase in transmittance at CPT conditions, we perform two-laser spectroscopy without modulation, as shown in figure 2.2b. The single photon absorption in the center of the lineshape is roughly five percent, with a reduction of one percent at two-photon resonance.

When probing an ensemble of donor-bound electrons, the lineshape of the CPT peak is a summation of the lineshapes for all members of the ensemble. Hence it resembles the distribution of electron spin splittings, providing a measure of the collective spin dephasing time T_2^*. Chapter 3 explains this in detail.

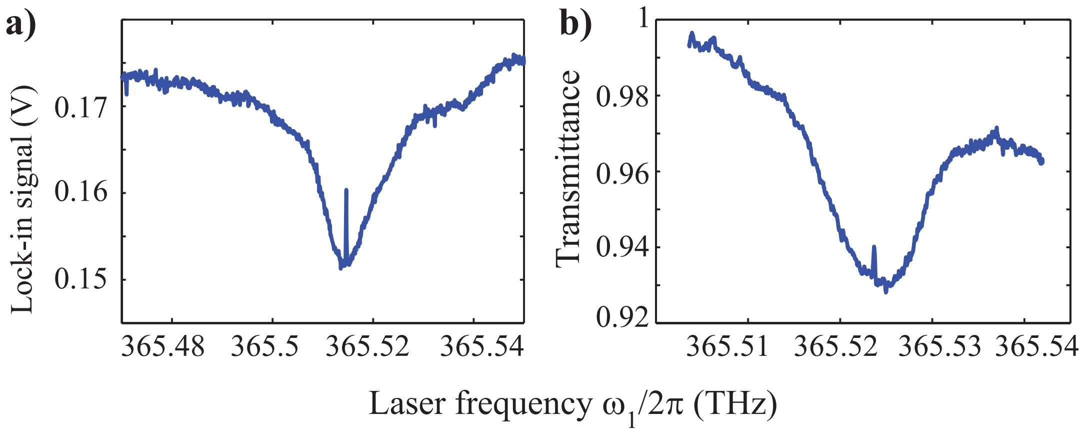

Figure 2.2: Signatures of coherent population trapping (CPT) in two-laser transmission traces. One laser is fixed at resonance with frequency ω_2 of the D^0-D^0X system, the other is scanned around frequency ω_1. The optical absorption lineshape shows a full-width-half-max $\Delta\omega/2\pi \approx 10$ GHz. A narrow CPT-peak of enhanced transmission is observed at two-photon resonance, where the difference frequency of the two laser fields corresponds to the electron-spin splitting ω_z (see figure 2.1). **a**, CPT-peak observed in the lock-in signal using differential transmission spectroscopy. The laser fixed at ω_2 is modulated. **b**, CPT-peak measured without modulation techniques. The two traces were taken at slightly different sample spots, hence the frequency shift of the optical transition.

2.3 Dynamic nuclear polarization and nuclear spin diffusion

Gallium and arsenic have non-zero nuclear spin. The D^0 electron is weakly bound and its large wavefunction contains in the order of 10^5 gallium arsenide lattice sites. Since the electron has an s-like Bloch function with highest probability density at the position of the nuclei, the electron spin has a strong hyperfine interaction with the surrounding nuclear spins. In effect, the electron spin experiences the nuclear spin dynamics as a mesoscopic magnetic field known as the Overhauser field, which influences the electron-spin splitting. Vice versa, the nuclear spin feels the vicinity of the electron spin as an effective magnetic field called the Knight field.

If the electron spin is polarized out-of-equilibrium, stochastic relaxation of the electron spin causes random fluctuations in the Knight field. If the Knight-field spectrum contains a frequency component that resonates with the nuclear spin splitting, angular momentum can be exchanged in a flip-flop process between the electron and nuclear spin. This phenomenon of driving the nuclear spin polarization out-of-equilibrium via the hyperfine interaction is known as dynamic nuclear polarization (DNP). Equation 2.3 describes the motion of a single nuclear spin perturbed by the electron spin's Knight field [41]:

$$\langle \dot{I}_z \rangle = -\Gamma_h \left(\langle I_z \rangle - \langle \overline{I_z} \rangle - \frac{I^2 + I}{S^2 + S} \left[\langle S_z \rangle - \langle \overline{S_z} \rangle \right] \right). \tag{2.2}$$

Here, the spin flip rate Γ_h contains the strength of the hyperfine interaction and the frequency overlap of the Knight-field's spectrum with the nuclear spin splitting. The overbars denote thermal equilibrium values of the spins' expectation values. $\langle I_z \rangle$ can be driven in both positive and negative direction by polarizing the electron spin out of thermal equilibrium.

As mentioned in the previous section, the shape and position of the CPT peak in two-laser transmission scans reveal the ensemble probability distribution of electron-spin splittings. In figure 2.3a, we optically polarize the nuclear spin bath at the position of D^0 using DNP, by keeping one laser resonant with frequency ω_2 for 30 minutes. During DNP pumping, a nuclear spin polarization builds up at the donor sites, resulting in a non-zero Overhauser field that effects the electron-spin splitting and thus shifts two-photon resonance. The CPT peak at thermal equilibrium is taken as a reference. We observe a frequency shift of the average two-photon resonance of 500 MHz after DNP, which corresponds to a nuclear spin polarization of 2 percent (as explained in chapter 3). Subsequently, the sample is put in the dark. CPT traces after 20 s and 40 s show relaxation of the CPT peak to its thermal equilibrium position.

Nuclear spin diffusion

Built-up nuclear spin polarization relaxes to thermal equilibrium via different channels. Firstly, angular momentum can be transferred to the electron spin, described by term $\langle I_z \rangle - \langle \overline{I_z} \rangle$ in equation 2.3. At magnetic fields much larger than the average and variance of the Overhauser field, this process becomes slow and can be neglected as compared to another relaxation mechanism: diffusion of nuclear spin polarization away from D^0 via nuclear spin dipole-dipole coupling. Figure 2.3b indicates two scenarios of nuclear spin diffusion that will yield different relaxation timescales. In the left panel, nuclear spin polarization that built up at D^0-sites within the laser spot diffuses into the unpolarized bulk nuclear spin bath. In the right panel, a bulk nuclear spin polarization has built up within the laser spot. The diffusion of bulk nuclear spin out of the laser spot will be substantially slower than the diffusion rate of nuclear spin away from D^0.

Figure 2.3c shows relaxation of the CPT-peak position, after DNP pump periods of varying duration. The maximum CPT shift of 500 MHz (for this particular pump laser intensity) was reached within 5 minutes and indicates the nuclear spin polarization for which the rates of DNP and nuclear spin diffusion are equal and opposite. Exponential fits yield a relaxation time of ≈ 30 s, independent of DNP pump duration. We attribute this to nuclear spin diffusion into the bulk surrounding the donor sites, as in the left panel of figure 2.3b. After the initial relaxation, the CPT peak has an offset from its position before DNP pumping, that increases with pump duration. This offset suggests the build up of bulk nuclear spin within the laser spot, as in the right panel of figure 2.3b. These results agree qualitatively with earlier work on nuclear spin diffusion at localized electrons [68].

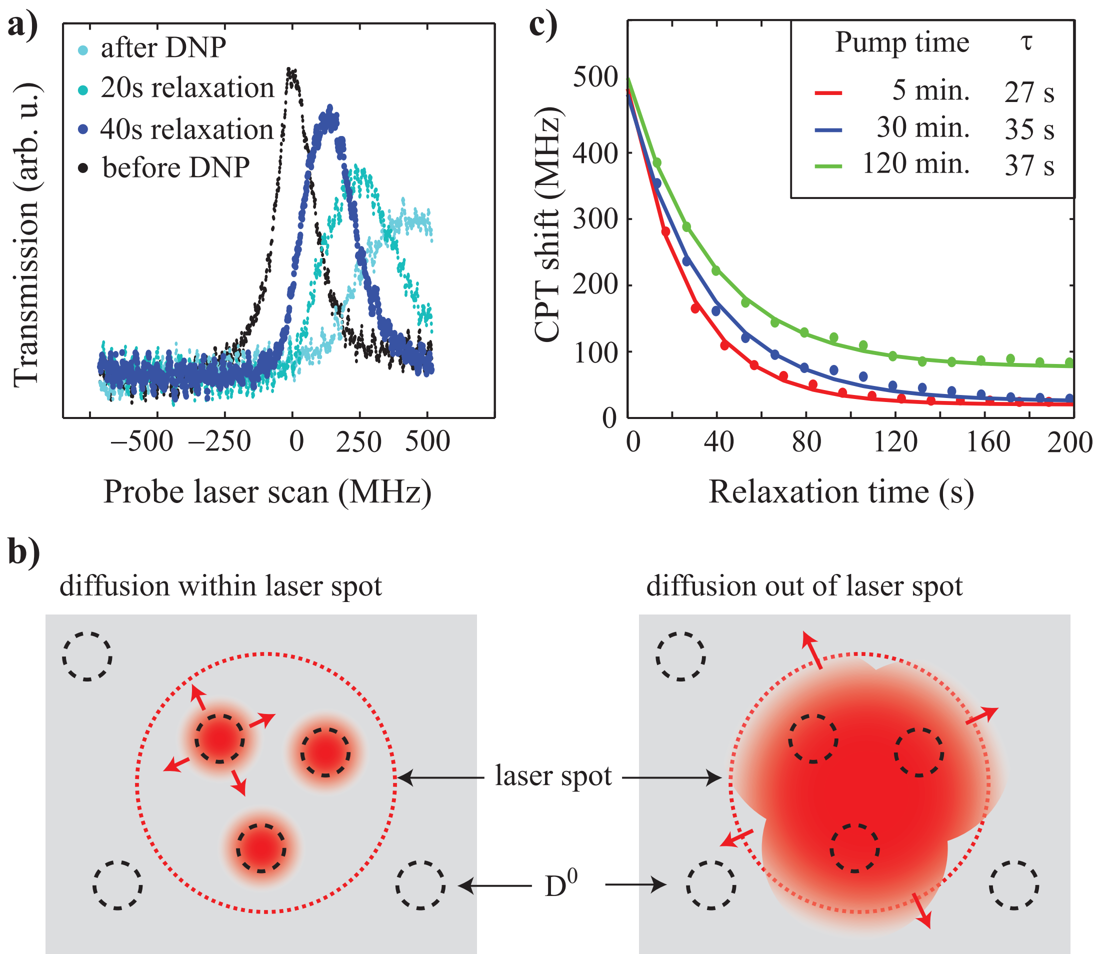

Figure 2.3: **a**, CPT signatures of dynamic nuclear polarization (DNP) after a 30 minute DNP pump period by a laser fixed at ω_2. CPT traces are taken right before and after the pump period, and after relaxation periods of 20 s and 40 s in the dark (both laser beams blocked). **b**, Schematic view of two qualitatively different scenarios of nuclear spin diffusion. In the left panel, nuclear spin polarization that built up at D^0-sites within the laser spot diffuses into the unpolarized bulk nuclear spin bath. In the right panel, diffusing nuclear spin polarization from the D^0-sites has build up a bulk nuclear spin polarization within the laser spot. The rate of diffusion of this bulk nuclear spin polarization increases with the laser spot size. **c**, CPT peak position after a DNP pumping period of varying duration, as a function of relaxation time in the dark. The lines indicate exponential fits, for which the time constants are presented in the legend. All DNP pumping periods used the same laser intensity.

Chapter 3

Stabilizing nuclear spins around semiconductor electrons via the interplay of optical coherent population trapping and dynamic nuclear polarization

Abstract

We experimentally demonstrate how coherent population trapping (CPT) for donor-bound electron spins in GaAs results in autonomous feedback that prepares stabilized states for the spin polarization of nuclei around the electrons. CPT was realized by excitation with two lasers to a bound-exciton state. Transmission studies of the spectral CPT feature on an ensemble of electrons directly reveal the statistical distribution of prepared nuclear spin states. Changing the laser detuning from blue to red detuned shows a transition from one to two stable states. Our results have importance for ongoing research on schemes for dynamic nuclear spin polarization, the central spin problem and control of spin coherence.

Part of this chapter was published in *Physical Review B* **93**, 161204(R) (2016)

3.1 Introduction

Following the emergence of electron spins in quantum dots and solid state defects as candidates for spin qubits it has become a major goal to realize control over the nuclear spins in such nanostructures. In many experimental settings, interaction with disordered nuclear spins in the crystal environment is detrimental to the coherent evolution of carefully prepared electron spin states [43, 44, 45]. Preparation of nuclear spins in a state that has reduced spin fluctuations with respect to the thermal equilibrium state will help to overcome this problem [46]. Proposals to achieve this goal have been put forward for electron spin resonance (ESR) on one- or two-electron quantum dots [47, 48], and for optical preparation techniques that either rely on a quantum measurement technique [49, 50] or a stochastic approach [51, 52, 53]. Experimental advances have been made with ESR and optical techniques on single quantum dots [39, 54, 55, 56, 57, 58, 59] and nitrogen-vacancy centers [60], and on quantum dot ensembles [61, 62].

Several of these works [39, 50, 51, 52, 53, 59, 60] make use of the optical response of the electronic system near the coherent-population-trapping resonance (CPT, explained below) because it is highly sensitive to perturbations from nuclear spins. Notably, these experiments so far have focussed on quantum dots where, due to the particular anisotropic confinement, hyperfine coupling with a hole-spin in the excited state is reported to dominate [39]. In recent work [42] we discussed how the interplay between electron-nuclear spin interaction and CPT influences the stochastics of the nuclear spin bath for a class of systems where hyperfine interaction with the ground-state electron spin dominates.

Here we report experiments on this latter class of systems. We demonstrate an all-optical technique that stabilizes the nuclear spin bath around localized donor electrons in GaAs into a non-thermal state under conditions of two-laser optical pumping. We show that the nuclear spin system is directed either towards a single stable state or (probabilistically) towards one of two stable states, depending on laser detuning from the excited state. Our results show how feedback control arises from the interplay between CPT and dynamic nuclear spin polarization (DNP), and confirm that the electron-spin hyperfine interaction dominates for our system (despite the strong similarity with the negatively charged quantum dot). Our results indicate that this interplay can be used to create stable states of nuclear polarization with reduced fluctuations.

3.2 Experimental methods

We perform measurements on the nuclear spin dynamics in a 10-μm thick MBE-grown film of GaAs doped with Si donors at a concentration of $\sim 3\times 10^{13}$ cm^{-3}, which is well below the metal-insulator transition (at $\sim 10^{16}$ cm^{-3}). The wafer is cleaved in 2-by-2 mm^2 parts along the $\langle 110\rangle$ crystal axes. The film is removed from a GaAs substrate by wet etching an AlAs buffer layer in HF. The film is then transferred to a sapphire substrate which allows us to do transmission measurements in a cryogenic microscope [63]. Measurements are performed at a temperature of $T = 4.2$ K and magnetic field of $B_{ext} = 5.9$ T. The sample is mounted such that the magnetic field direction is along the $\langle 110\rangle$ axis. Light from tunable continuous-wave lasers (Coherent MBR-110) is delivered to the sample by a polarization-maintaining fiber and passes through the sample along the $\langle 100\rangle$ axis. Transmitted light is collected in a multimode fiber and detected by an avalanche photodiode outside the cryostat. For getting reproducible data it was essential to stabilize laser powers within 1% and laser frequency drift within 10 MHz.

The optical transitions that we address are from the donor-bound electron spin states ($|\uparrow\rangle$, $|\downarrow\rangle$) to a level of the bound trion ($|D^0X\rangle$), that consists of two electrons and one hole bound at the silicon donor. These three states form a Λ-type energy level configuration, further defined in Fig. 3.1(a). The magnetic field is applied perpendicular to the light propagation direction (Voigt geometry) such that the optical transitions have polarization selection rules discriminating between horizontally ($\sigma_{+,-}$, coupling to $|\uparrow\rangle - |D^0X\rangle$) and vertically ($\pi$, coupling to $|\downarrow\rangle - |D^0X\rangle$) polarized light.

3.3 Measurement of the nuclear spin distribution by CPT

We start with reproducing CPT for our system [17, 18]. CPT is a narrow resonance in two-laser driving as in Fig. 3.1(a) [17] where the system gets trapped in a dark state (for ideal spin coherence $|\Psi\rangle \propto \Omega_2 |\uparrow\rangle - \Omega_1 |\downarrow\rangle$). In transmission this appears as a narrow window of increased transparency within the broader absorption dip when one laser is scanning while the other is fixed (Fig. 3.1(b)). Its position signals two-photon resonance, and occurs where $\omega_1 - \omega_2$ equals the the electron spin splitting. The lineshape of the CPT resonance can reveal information about the electron spin states, which can be obtained by fitting the curve in Fig. 3.1(b) to the Lindblad equation for the Λ-system [38]. Our n-GaAs samples yield an inhomogeneous dephasing time $T_2^* \approx 3$ ns [17]. However, the

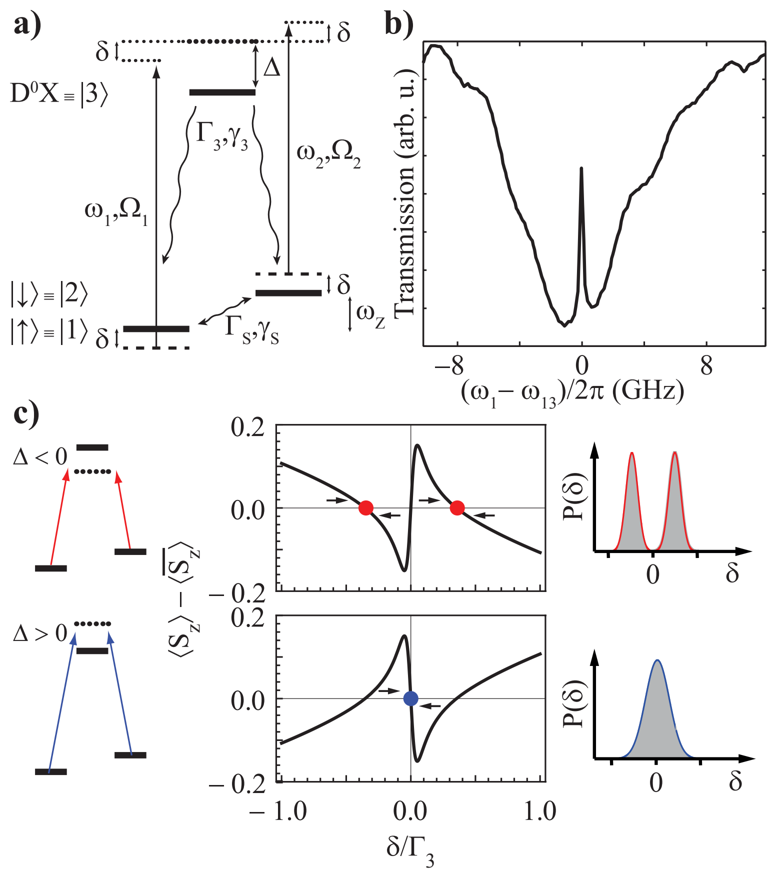

Figure 3.1: Energy levels and feedback control scheme. (a) Thick black lines are the spin states $|1\rangle$, $|2\rangle$ and optically excited state $|3\rangle$. Γ_s, γ_s and Γ_3 ,γ_3 are spin and excited state decay and dephasing rates, respectively. Two lasers at frequencies ω_1, ω_2 couple to the system with Rabi strengths Ω_1 and Ω_2, excited state detuning Δ, and Overhauser shift δ (see main text). The energy splittings ω_{13}, ω_{23} and ω_Z are fixed at the values for $\delta = 0$ ($\hbar$ omitted for brevity). (b) Measured CPT signature in the n-GaAs sample (here for $\omega_2 = \omega_{23}$ and $\delta = 0$). (c) Left panel: two distinct control regimes for nuclear spin control. Middle panel: optically-induced electron spin polarization ($\langle S_z\rangle - \langle \overline{S}_z\rangle$) as a function of Overhauser shift δ, with lasers fixed at $\omega_1 = \omega_{13}+2\pi\Delta$ and $\omega_2 = \omega_{23}+2\pi\Delta$, displays two stable states of the nuclear spin bath for $\Delta < 0$ (red dots) and one stable state for $\Delta > 0$ (blue dot). Right panel: expected steady state Overhauser shift distributions. Calculations with parameters $\gamma_3 = 10$, $\Gamma_s = 10^{-4}$, $\gamma_s = 10^{-3}$, $\Omega_1 = \Omega_2 = 0.5$, $\Delta = \pm 1$ normalized to $\Gamma_3 \equiv 1$ [42].

homogeneous dephasing time T_2 has been estimated to be at least 7 μs [64] with a spin-echo technique. The discrepancy between T_2 and T_2^* is largely due to dephasing caused by $\sim 10^5$ disordered nuclear spins per electron.

Due to the Fermi contact hyperfine interaction, a non-zero nuclear spin polarization exerts an effective magnetic (Overhauser) field B_n on the electron spin and causes a shift of the electron spin levels, denoted by δ in Fig. 3.1(a). The value of $\delta = p\delta_{\max}$ is proportional to the nuclear spin polarization $p \in [-1, 1]$, where $\delta_{\max}$ is the maximum shift set by the hyperfine interaction strength. For the donor electron in GaAs $\delta_{max} = 24.5$ GHz (obtained from the maximum Overhauser field [65] via $\delta = g\mu_B B_n/2\hbar$ with g-factor $g = -0.41$ [17]). The thermal equilibrium properties of the nuclear spin bath are well approximated by considering N non-interacting spins I with gyromagnetic ratio γ. Then p and its variance σ_p^2 are in the high temperature limit $\hbar\gamma B_{ext}/k_{\mathrm{B}}T \ll 1$ (our experimental conditions) $p = \hbar\gamma B_{ext}(I+1)/3k_{\mathrm{B}}T \approx 0$ and $\sigma_p^2 = (I+1)/3IN - p^2$ [46].

Because nuclear spin dynamics is slow as compared to the electron's, light interacting with the system sees a snapshot of the Overhauser shift taken from a distribution $P(\delta)$. A measurement on an ensemble of these systems should account for averaging over $P(\delta)$. The CPT lineshape of Fig. 3.1(b) arises from the transmittance, with a susceptibility that is averaged over $P(\delta)$,

$$T(\omega_i) = \exp\left(-\rho\frac{\omega_i d}{c}\int_{-\infty}^{+\infty} P(\delta)\chi_i''(\omega_i,\delta)\mathrm{d}\delta\right), \tag{3.1}$$

where d is the thickness of the medium, ρ the density of donors, c the speed of light, $i = 1, 2$ labels the laser fields. Here χ_i is the susceptibility for the laser field for a fixed δ. It can be calculated from the Lindblad equation and depends on other system parameters implicitly [42]. At thermal equilibrium $P(\delta)$ is a Gaussian centered at zero with variance $\sigma_\delta^2 = \delta_{\max}\sigma_p^2$. For $I = 3/2$ and $N = 10^5$ it has a width (FWHM) of $2\sqrt{2\log(2)}\sigma_\delta = 136$ MHz, which roughly corresponds to the width of the measured CPT.

3.4 DNP near the CPT resonance

However, $P(\delta)$ can undergo changes when the electron spin is brought out of thermal equilibrium by optical orientation. An optically-induced electron spin polarization will in turn induce nuclear spin polarization via a hyperfine-mediated cross-relaxation process known as DNP. In Ref. [42] it was described how the interplay between the laser-induced electron spin polarization near CPT resonance and DNP can change the shape of $P(\delta)$ by autonomous feedback control, leading to the formation of stable states for the nuclear spin polarization and offering the potential of reducing the variance σ_δ^2. The essence of this method is pictured schematically in Fig. 3.1(c). It shows two distinct control regimes (color coded, red and blue) where both lasers are either red ($\Delta < 0$) or blue ($\Delta > 0$) detuned from the excited state. The change in laser coupling strength with δ is asymmetric when $\Delta \neq 0$ (one laser approaches resonance while the other moves away from it). For a single system with a particular Overhauser shift this causes a sharp change in the optically-induced electron spin polarization $\langle S_z \rangle - \langle \overline{S}_z \rangle$ (where the overbar implies that the expectation value is taken at thermal equilibrium), shown in the middle panels as a function of δ (the Overhauser shift is here normalized to Γ_3). The blue and red dots indicate stable points, where $\langle S_z \rangle = \langle \overline{S}_z \rangle$ and $\partial/\partial\delta(\langle S_z \rangle - \langle \overline{S}_z \rangle) < 0$. We thus expect $P(\delta)$ to evolve from the initial Gaussian to either a distribution with two maxima, or to a distribution with one maximum. Such steady-state distributions are non-thermal and can thus have reduced fluctuations if the system's feedback response (slope of $\langle S_z \rangle - \langle \overline{S}_z \rangle$ near the stable point) is strong enough [42].

3.4.1 Competition of DNP with nuclear spin diffusion

The final steady-state configuration of $P(\delta)$ around CPT resonance depends on the competition between DNP driving the nuclear spin to a stable configuration and processes by which the nuclear spin decays back to its thermal distribution. The polarization relaxation of a single nuclear spin in contact with an electron is given by [42]:

$$\langle \dot{I_z} \rangle = -\Gamma_h \left(\langle I_z \rangle - \langle \overline{I_z} \rangle - \frac{I^2 + I}{S^2 + S} \left[\langle S_z \rangle - \langle \overline{S_z} \rangle \right] \right). \tag{3.2}$$

Here, I and I_z (S and S_z) are the spin quantum number and spin z-component of the nuclear (electron) spin. Γ_h is the hyperfine relaxation rate [66] and the overbars depict the expectation values of the spin polarizations at thermal equilibrium. When we sum the relaxation of all nuclei in contact with a single bound electron, we get the time evolution of the Overhauser shift δ, as felt by the electron:

$$\dot{\delta} = -\Gamma_h \left[\delta - K(\langle S_z \rangle - \langle \overline{S_z} \rangle) \right] - \Gamma_d \delta. \tag{3.3}$$

The first part $-\Gamma_h \delta$ describes the relaxation of $\langle I_z \rangle$ to its value at thermal equilibrium. The second part describes dynamic nuclear polarization by the polarized electron spin, where K is a constant determined by the strength of the hyperfine coupling. The last part $\Gamma_d\delta$ represents another relaxation channel for nuclear spin polarization: nuclear spin diffusion, where angular momentum is exchanged between neighboring nuclear spins by direct dipole-dipole coupling. Technically, this is not a relaxation term, since nuclear spin polarization is not lost but rather spread out spatially. However, it effectively acts as a decay channel for the polarization of the nuclear spins contained within the wavefunction of the D^0-electron, because angular momentum diffuses away from the volume of interest. The rate Γ_d is assumed constant for all theoretical fits presented in this chapter. Nevertheless, the electron spin polarization $\langle S_z \rangle$ is known to have an effect on this nuclear spin diffusion rate through the hyperfine interaction. The electron spin acts as an effective magnetic field felt by each nucleus, known as the Knight field [67], that causes a shift on the nuclear spin states of nucleus I_i describes by Hamiltonian

$$H_k = A^i I_z^i \langle S_z \rangle \propto |\Psi_e(R^i)|^2 \; I_z^i \langle S_z \rangle \, . \tag{3.4}$$

Here, A^i is the hyperfine coupling constant, which is proportional to the probability distribution of the electron $|\Psi_e(R^i)|^2$, where R^i is the position of the nucleus. Since $|\Psi_e(R^i)|^2$ is non-uniform (the ground state of D^0 has an s-like orbital envelope), the Knight field will show a gradient that lifts the degeneracy of nuclear dipoles, which suppresses nuclear spin diffusion.

3.5 Experimental observation of one and two stable states

We investigate this interplay between CPT and DNP for the donor-bound electrons in GaAs by monitoring the changes in the CPT lineshape induced by two-laser optical pumping, with both lasers at equal intensity near two-photon resonance. Figures 3.2(a,b) show the CPT lineshape before (gray lines) and after 10 min of optical pumping with blue- and red-detuned lasers. While scanning over the ensemble CPT peak, the probe laser meets exact two-photon resonances (near-ideal CPT peaks) of individual electrons for a range of δ-values. The susceptibility is thus proportional to the number of electron spins experiencing a particular Overhauser shift δ, hence reflecting the underlying nuclear spin distribution. The nuclear spin distribution stabilizes as predicted in both cases, observed as a non-shifted single CPT peak in Fig. 3.2(a) and a non-shifted split CPT peak in Fig. 3.2(b) (the splitting directly reflects the doubly peaked $P(\delta)$ of Fig. 3.1(c)). This is in clear contrast with a CPT peak recorded after 10 min of single-laser optical pumping (inset Fig. 3.2(a)), which shifts the CPT peak by $\sim$400 MHz since DNP gives here a net nuclear spin polarization.

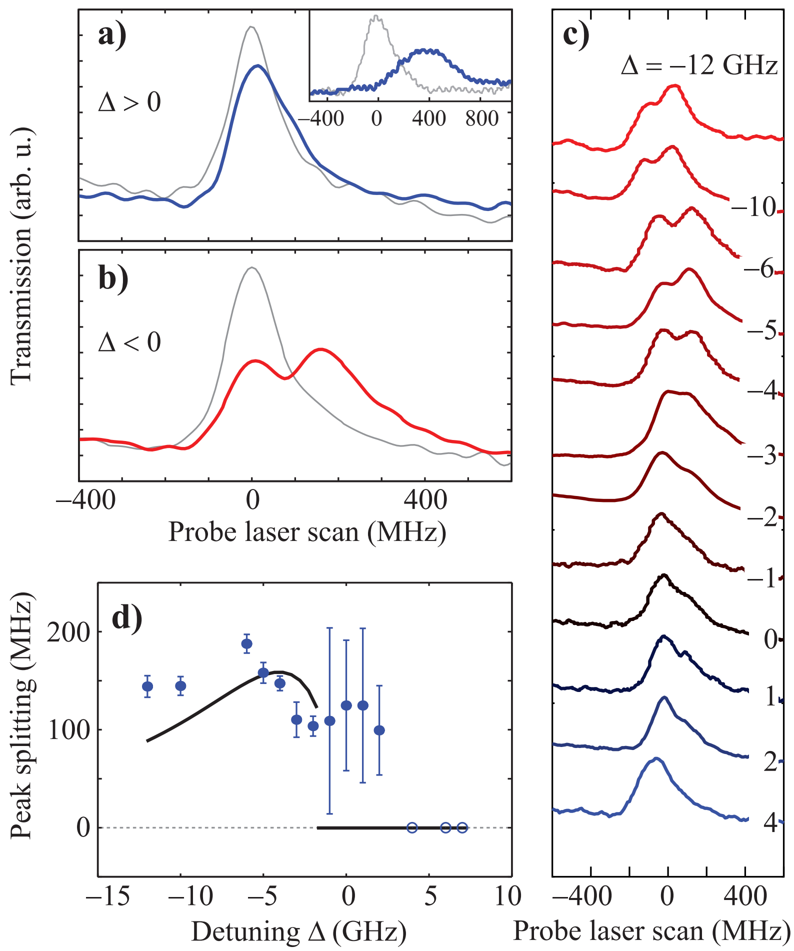

Figure 3.2: CPT signatures of DNP feedback. (a) The CPT peak in the transmission signal as a function of probe laser frequency, before (gray) and after (blue) a DNP pumping period with two lasers fixed on two-photon resonance (Fig. 1(c)) and detuning $\Delta = +4$ GHz. The inset shows how DNP pumping by one laser (on the $|\uparrow\rangle - |D^0X\rangle$ transition) causes a shift of the CPT resonance. Two-laser pumping stabilizes the nuclear spin polarization at its thermal equilibrium value (here without observing a significant narrowing). (b) Results obtained as for panel (a), but with $\Delta = -6$ GHz. In this case the CPT peak after DNP pumping (red) shows a splitting. (c) CPT traces taken after DNP pumping, for various values of Δ. (d) Values of the peak splitting, obtained from traces as in panel (c). All data was taken with both laser intensities stabilized at values of about 3 Wcm^{-2} (for DNP pumping and CPT probing). Black line: simulation with parameters as in Ref. [42], except $\Gamma_d/\overline{\Gamma}_h = 4000$ and $\gamma_3 = 20$ GHz.

The lineshape in the main panel of Fig. 3.2(a) remains similar, while a narrower and higher CPT peak is expected if the width of the stabilized $P(\delta)$ would indeed be reduced. In Ref. [42] it was pointed out that for an open system the narrowing by the feedback mechanism is in competition with nuclear spin diffusion. For donors in GaAs this plays a stronger role than for quantum dots, where a material barrier surrounding the dot suppresses this spin diffusion. Not observing a narrowing of the CPT peak is also due to non-uniform laser intensities for the electron ensemble (further discussed below).

Figure 3.2(c) shows the transition from red- to blue-detuned two-laser pumping, for a range of detunings Δ. Splittings in these CPT peaks are analyzed in Fig. 3.2(d), obtained by fitting two Gaussians to each CPT peak. Where the fit does not improve with respect to a single-Gaussian fit we take the splitting to be zero. The data reproduces the essential features of the model [42] (black line), showing a discontinuous transition and a maximum splitting when the pump lasers are tuned to the slope of the transition line at $\Delta \approx -5$ GHz, where the response to a shift of δ is largest. We analyzed that this transition is a unique feature that confirms the dominance of the electron spin for the relevant DNP mechanism [42]. For $\Delta \gtrsim 0$ there is no good match, but the fitting also yields larger error bars. We attribute this to inhomogeneous broadening in the optical transitions (effective spread in detunings Δ) which prevents all systems from making the transition simultaneously.

3.6 Laser power and frequency dependence of the CPT splitting

We now focus on the control regime $\Delta < 0$ to examine the dependence of the stabilization on the control parameters during the optical pumping phase. Figure 3.3(a) shows the importance of carefully tuning the relative frequencies for getting a balanced distribution. A detuning as small as 31 MHz for one of the lasers gives a significant shift within $P(\delta)$ to either one of the stable states. Figure 3.3(b) shows values for the splitting as a function of the laser powers (varied simultaneously). The splitting shows a discontinuous onset and subsequent increase due to power broadening of the CPT peak. The data qualitatively matches the prediction ([42], black line) but the slope is lower than the simulation. We attribute this to standing wave patterns in the GaAs layer (which acts as a weak cavity). The patterns for the two lasers do not fully overlap since they differ in frequency. This prohibits addressing the entire ensemble with equal laser intensities, and gives for the ensemble an averaged, less effective feedback mechanism.

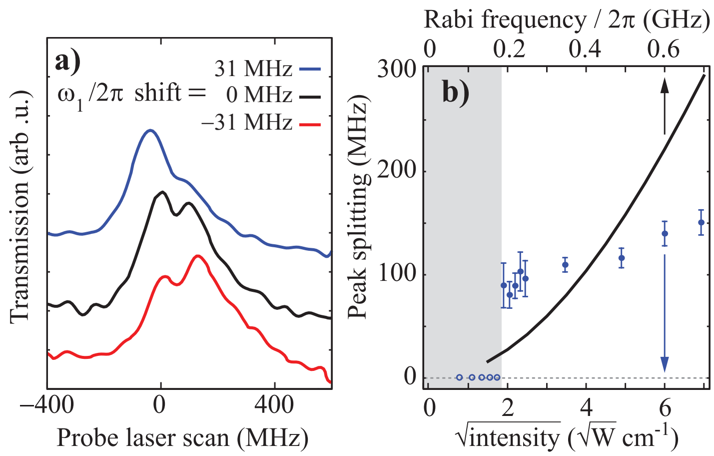

Figure 3.3: (a) CPT traces after DNP pumping with two lasers at $\Delta \approx -3.5$ GHz. The trace labeled $\omega_1 = 0$ MHz is taken after pumping on exact two-photon resonance. The blue (red) trace is measured after pumping with $\omega_1/2\pi = +(-)31$ MHz detuned from exact two-photon resonance (see Fig. 1(c)). (b) The peak splitting in CPT traces after pumping with $\Delta \approx -4$ GHz and exact two-photon resonance, as a function of the intensity of the two lasers (keeping the intensity ratio fixed near 1). The gray background shows the range where the CPT peak shape was analyzed as a single peak. Significant double-peak character was observed for the total laser intensity above $\sim$3 Wcm^{-2}. CPT traces were all taken with both lasers intensities at $\sim$3 Wcm^{-2}. Black line: simulation with same parameters as in Fig. 3.2, the top axis shows the Rabi frequency corresponding to the simulation [42].

This also provides a limitation for the amount of CPT-peak narrowing in the blue-detuned case. The narrowing effect relies on carefully balanced laser intensities, and this is compromised due to the intensity variation inside the sample. Studying the achievable narrowing of $P(\delta)$ requires an experiment with uniform intensities for the ensemble.

3.7 Build-up and decay of the bistable nuclear spin polarization

Figure 3.4 presents time evolution of the effects. Figure 3.4(a) shows build-up of the splitting, obtained by taking CPT traces during the optical pumping phase every 30 s (each trace is collected within 1 s). The splitting stabilizes after approximately 4 min. Figure 3.4(b) shows decay of the splitting. It consists of traces collected after the optical pumping phase. After 10 min of optical pumping (repeated before each trace) the system is kept in the dark for a time ranging from 1 to 10 s. The splitting fades away in seconds, consistent with the relaxation of the

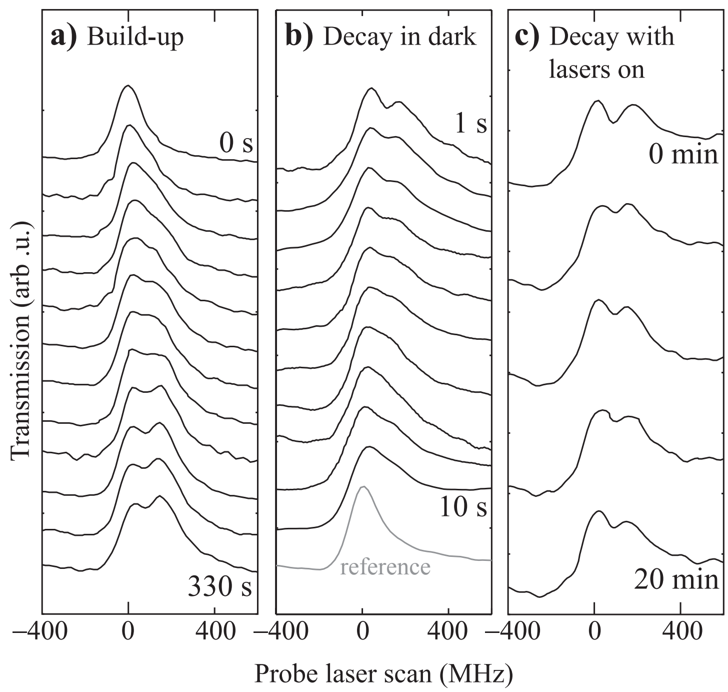

Figure 3.4: Time evolution of build-up (a) and decay (b,c) of stabilized nuclear spin ensembles, measured during and after the DNP pumping period (subsequent traces top to bottom, as labeled). Panel (b) gives a reference for the CPT peak before pumping. The data in (a) is obtained from CPT scans of 1 s in between periods of 30 s DNP pumping with two lasers fixed at two-photon resonance ($\Delta = -4$ GHz). Panel (b) presents CPT scans of 1 s, taken after a fully dark period of 1 s (top trace) to 10 s (bottom trace) after DNP pumping ($\Delta = -4$ GHz). The results in (c) are from continuously taking CPT scans of 1 s (only four traces shown), after a DNP pumping period at $\Delta = -2$ GHz. All data was taken with both laser intensities stabilized at values of about 3 Wcm^{-2} (for DNP pumping and CPT probing).

lattice nuclear spins by spin diffusion away from the electron [68]. However, when CPT scans are taken continuously after the optical pumping phase the splitting decays much slower and persists up to at least 20 min (Fig. 3.4(c), we verified that taking such scans without the preceding pumping phase does not induce a splitting). We attribute this to a suppression of the spin diffusion while the system is illuminated: under optical excitation (during CPT scans) the electron spin is most of the time significantly polarized, creating an inhomogeneous Knight field for the surrounding nuclear spins that suppresses nuclear spin diffusion [69, 70] (notably, our DNP pumping with $\Omega_1 = \Omega_2$ gives zero Knight field).

To further investigate the suppression of nuclear spin diffusion using the Knight field, we study the effect of varying CPT laser intensities on the decay of the split peak. Since the Knight field felt by nuclei in the vicinity of the donor electron is proportional to $\langle S_z \rangle$ (as shown in equation 3.4), the suppression should depend on the laser intensities used during CPT scans. Figure 3.5a shows the decay of two identically prepared split nuclear spin polarizations while continuously taking CPT traces (similar as in 3.4c) with equal (left panel) and unequal (right panel) laser intensities. The traces demonstrate how a distribution of nuclear spin ensembles that are slightly polarized relaxes back to its thermal equilibrium configuration centered around zero polarization. The transition from a split peak to a single peak takes tens of seconds in the case of equal laser intensities, while for unequal intensities the split peak character is still visible after 90 s.

We quantify the relaxation of the split nuclear spin configuration in figure 3.5b, by fitting the separation of the split peak over time, for different CPT intensities. The decay timescale changes from 9 s for symmetric intensity (blue triangles) up to 756 s for the most asymmetric intensity (black dots). The fast decay of 9 s coincides with the timescale of decay in the absence of optical fields, as in figure 3.4b (and [71]). The peak splitting for the slowest decay of 756 s stabilizes after a partial decay in the first 20 s, showing the same evolution as the traces in figure 3.4c.

We explain this strong dependence on relative laser intensity by looking at the Knight field felt by the nuclear spin ensembles at the donor sites. As discussed earlier, the Knight field has a gradient around each donor, which lifts the degeneracy of neighboring nuclear dipoles, suppressing nuclear-nuclear flip-flops. During a CPT scan with equal laser Rabi frequencies, $\langle S_z \rangle$ fluctuates around zero, as shown in figure 3.2c. At periods in the scan where $\langle S_z \rangle \approx 0$, the Knight field vanishes and nuclear spins at the donor site can exchange momentum with the bulk nuclear spin unimpeded. A scan with asymmetric Rabi frequencies will show a similar CPT lineshape, but the electron spin is significantly polarized during the whole CPT scan, which results in a continuous Knight field that impedes nuclear spin diffusion.

This trend qualitatively agrees with theoretical predictions on the effect of localized electrons on nuclear spin diffusion [70] that take into account both the Knight field and electron-mediated nuclear spin exchange. It should be noted that electron-mediated nuclear spin exchange, where the presence of a localized electron enhances diffusion by enabling nuclear long-range interactions via the hyperfine interaction, is very small as compared to nuclear dipole-dipole coupling at our magnetic field $B_{ext} = 5.9$ T [70, 72]. Hence, mediated diffusion will only be a significant factor when direct spin diffusion is strongly suppressed by the Knight field (as for the 756 s relaxation).

We can rule out that the relaxation times discussed above are influenced by the accumulation of nuclear polarization in the bulk GaAs between D^0-centers. In the bistable nuclear configuration after red detuned CPT feedback, approximately half of the addressed donor sites in the laser spot contain a nuclear spin ensemble that is slightly polarized along the external magnetic field, while the other half is polarized in the opposite direction. Hence, angular momentum diffusing to the bulk will cancel out and result in a bulk nuclear spin polarization with much smaller magnitude than the polarization at the donor sites. Thus, nuclear spin polarization at the donor sites can decay to the unpolarized bulk unhindered.

The suppression of nuclear spin diffusion at the donor sites could be used to improve the strength of the feedback control and the amount of narrowing: if the temperature of the experiment would be lower or the magnetic field stronger (increased $\langle \overline{S}_z \rangle$) the thermal-equilibrium electron spin polarization can suppress nuclear spin diffusion. Studies of these effects are partly addressed in the next chapter.

3.8 Conclusion

Our results open the possibility to use the interplay between CPT and DNP to operate a mesoscopic spin system as a feedback loop that converges towards a well defined steady state, determined by laser power and detuning, with the possibility of reduced nuclear spin fluctuations and less electron spin dephasing. The mechanism is generally applicable to localized spins where DNP is dominated by electron-nuclear spin hyperfine coupling and can also be used for other paramagnetic defects, as ensembles or single systems. A notable example is the fluorine donor in ZnSe [73, 74], a II-VI material with dilute nuclear spins (in GaAs all atoms have non-zero nuclear spin). Nuclear spin diffusion, mediated by dipole-dipole interaction (inversely proportional to distance between nuclear spins to the power 6), will here be much less a limitation for narrowing.

We thank A. U. Chaubal and R. S. Lous for help and valuable discussions, and acknowledge financial support from the Dutch FOM and NWO, ERC Starting Grant 279931, the Research school Ruhr-Universität Bochum, and the German programs BMBF Q.com-H 16KIS0109, Mercur Pr-2013-0001, and the DFH/UFA CDFA-05-06.

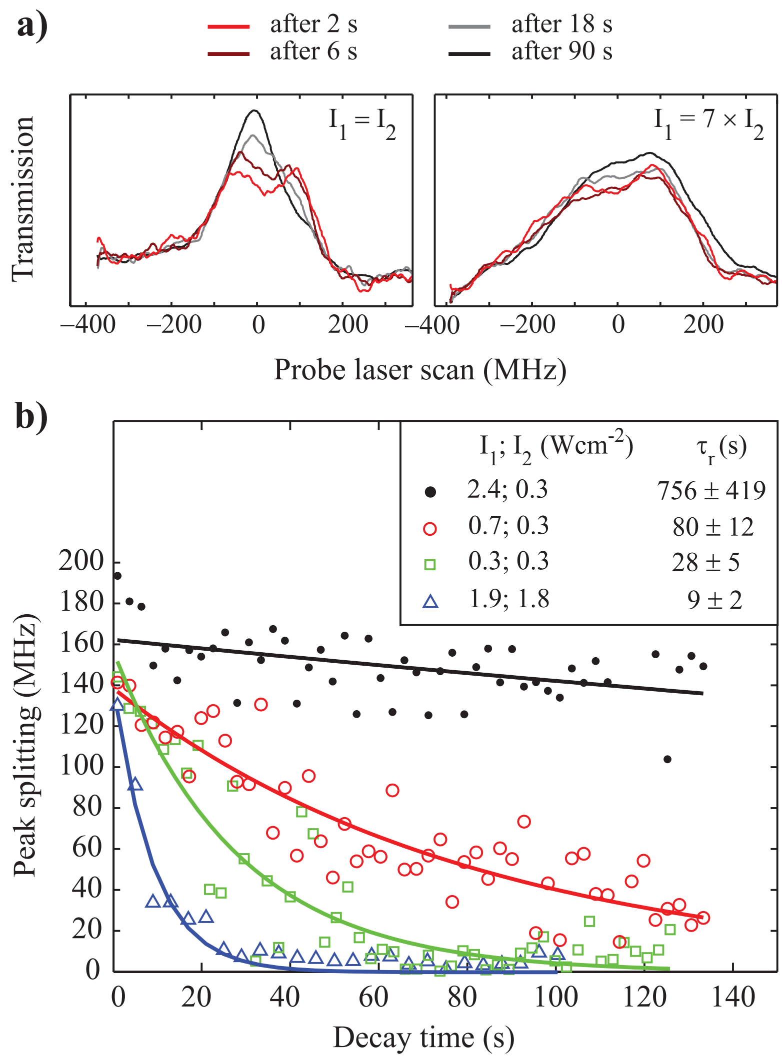

Figure 3.5: Decay of split nuclear spin ensembles, as a function of CPT laser intensities. **a**, CPT traces at various moments after red detuned DNP pumping, obtained by continuously taking CPT traces. The left (right) panel shows traces taken with equal (different) laser intensities I_1 and I_2. Both decay experiments were preceded by an equal DNP pumping period of 6 minutes at $\Delta = -4$ GHz, with laser intensities $I_1 \approx 0.7$ Wcm^{-2} and $I_2 \approx 8.1$ Wcm^{-2}. **b**, Time evolution of the peak splitting after red detuned DNP pumping (same as in **a**), for varying intensities during the CPT scans. Peak splittings were determined by fitting CPT lineshapes with two Gaussians. The relaxation time of the double-peak nuclear spin distribution back to thermal equilibrium clearly depends on the intensity ratio, where asymmetric intensities result in slower relaxation. τ_r depicts the relaxation times extracted from exponential fits.

Chapter 4

Self-improving coherent population trapping in ensembles with non-uniform laser intensity

Abstract

In this chapter, we show experimental evidence on self-improving optical coherent population trapping (CPT) with an ensemble of donor-bound electrons in hyperfine contact with a nuclear spin bath, by suppressing polarization fluctuations of the nuclear spin using a two-laser feedback technique that combines CPT with dynamic nuclear polarization. We analyze how standing wave formation and the transverse intensity profile of the laser fields lead to non-uniform driving of the ensemble dynamics, and simulate its effect on the two-laser feedback.

This chapter is based on references 1 and 2 on page 133

4.1 Introduction

In chapter 3, we presented optical experiments on an ensemble of donor-bound electrons (D^0) in GaAs, where each electron couples to a large number of nuclear spins via the hyperfine interaction. We drove the two optical transitions from the electron spin states to an excited state formed by a bound exciton (D^0X) around the spectrally sharp two-photon transition known as coherent population trapping (CPT). We used the transfer of angular momentum between the electron and nuclear spin known as dynamic nuclear polarization (DNP) and the fact that around CPT conditions the sign of DNP is dependent on the polarization of the nuclear spin, to suppress nuclear spin fluctuations and improve the homogeneity of the environment of the ensemble electrons. We provided experimental evidence for all-optical control on these nuclear spin ensembles. The case where two lasers drive the optical transitions red-detuned, resulting in a split CPT lineshape, was used to demonstrate the validity of our model. However, a narrowed CPT lineshape as predicted for blue-detuned driving was not yet observed. This chapter focuses on blue-detuned two-laser DNP pumping and shows successful experimental observations of narrowed CPT, indicating the suppression of nuclear spin fluctuations. Still, the amount of narrowing, and thereby the increase in spin dephasing time of the electron spin ensemble that was observed experimentally is more than a factor 3 lower than predicted by our simulations [42]. We attribute this to non-uniform driving-laser fields inside the GaAs film.

In this chapter, we therefore set out to better analyze the mismatch between predictions of our model and experimental observations. We design changes in the experimental approach to remove the technological shortcomings that prevent the observation of the optimal narrowing. Firstly, we quantify the fluctuations in laser intensity due to self-interference of the laser in the film. We then expand our model to include the detrimental effects of non-uniform laser intensity across the electron ensemble on narrowing of the nuclear spin configuration. We show how these expanded simulations on DNP-feedback can explain our experimental data, and discuss how the experimental approach can be improved to yield more successful suppression of nuclear spin fluctuations. We then show additional experimental traces on the dependence of laser intensity and the time evolution of the distribution of nuclear spin polarization under blue detuned driving conditions. At the end of this chapter, we discuss more extensively (based on chapter 3) how the Knight field plays a role also during DNP feedback and how this might change the requirements on the driving-laser intensities during DNP pumping.

4.2 Experimental observation of suppressed nuclear-spin fluctuations

To reduce the uncertainty of ground-state splittings for our ensemble of electron spins, we drive the lambda-systems provided by the donor-bound exciton complex with two lasers, as schematically depicted in figure 3.1a. As discussed in the previous chapter, to lock the ensemble distribution of nuclear spin polarizations at a single value for the Overhauser field, both optical transitions are driven blue-detuned in the high energy tail of the optical resonance. The two lasers are frequency-stabilized with a difference in energy that equals the electron spin splitting in the absence of nuclear spin polarization (or Overhauser shift $\delta = 0$). In theory, DNP now drives the combined electron-nuclear spin system towards a configuration with both a reduced difference in Overhauser shift between electron spins and suppressed temporal fluctuations of the nuclear spin polarization at each single electron. For realistic estimations of relaxation and decoherence parameters for the electron lambda-system, for the hyperfine coupling rate Γ_h and for the nuclear spin diffusion rate Γ_d, our model predicts a factor $\sim$6 narrowing of the Overhauser shift distribution and an equal increase in the ensemble electron-spin dephasing time.

Although clearly predicted by our theoretical model, observing the blue-detuned narrowing of the CPT lineshapes turned out to be more elusive than the red-detuned split character. After a time-consuming search for the optimal experimental settings, we were able to reach the situation where CPT improves itself by pushing the nuclear spin environment in an ordered configuration. Successful narrowing of the CPT lineshape after blue-detuned driving was harder to observe than red-detuned splitting of CPT because of multiple reasons: Since we lack precise knowledge of the transition dipole moments of the D^0X transitions, we vary both laser intensities over a large range during the DNP pumping, to get near-equal Rabi frequencies for the driving of the two lasers. The requirements on DNP pumping intensity are stricter in the blue-detuned than in the red-detuned case. As figure 3.3b showed, a pronounced CPT splitting occurs when the pump laser intensities exceed a minimum value. On the contrary, narrowing of the CPT lineshape only occurs for a small range of pumping intensities in between a minimum and a maximum threshold, as we observe in figure 4.9b. Also, the intensities during CPT traces are more critical in the blue-detuned case. During CPT traces, a trade-off occurs between signal-to-noise, where high intensity is favored, and power broadening of the CPT lineshape, as discussed in the supplementary information. For red-detuned driving, the amount of splitting in the

CPT lineshape was studied, which is not influenced by power broadening, while the shape of a narrowed CPT lineshape that is expected for blue-detuned driving is easily affected by power broadening. Therefore, first signatures of a split CPT lineshape are far easier to recognize than a minor narrowing of the lineshape, making it less challenging to find the right values for experimental parameters.

The investment of more measurement time, incremental optimizations of the experimental setup and possibly a sample spot with a more homogeneous strain eventually lead to the successful observation of suppressed nuclear spin fluctuations; Results are shown in figure 4.1.

Figure 4.1 shows experimental traces of the transmission of 10-μm thick GaAs films on a sapphire substrate, with a silicon doping that gives a donor density $n = 3 \times 10^{13}$ cm^{-3}. We focus on the CPT lineshape at two-photon resonance and compare CPT before (gray lines) and after a DNP feedback period of 5-10 minutes at a detuning of $\Delta \approx 6$ GHz (blue lines). To take CPT traces, the laser that couples the electron spin-down state to the excited state is kept fixed at frequency $\omega_{23} + \Delta$, while the other laser is scanned around $\omega_{13} + \Delta$ (see figure 3.1). CPT scans were typically taken with $5 - 10$ times lower laser intensities than the intensities during DNP pumping. We varied the two laser intensities during DNP over a range of absolute and relative values. Figure 4.1 presents the most pronounced CPT-narrowing observed to date.

The traces shown in the top panel are taken on a sample consisting of a GaAs film directly on sapphire, without an anti-reflection layer in between. As analyzed later in this chapter, this causes both laser intensities to vary independently with a factor $\sim$4 throughout the sample. The CPT lineshape after DNP pumping has a width that is reduced with a factor $\sim$2 as compared to the equilibrium lineshape before pumping, much lower than the predicted factor $\sim$6. Also, the amount of transmission at the CPT lineshape stays approximately the same, while a narrowed distribution of the electron ground-state splittings should enhance transmission at the center of the lineshape (i.e. should give an enhanced CPT peak height).

The lower panel shows similar results, for a sample with an anti-reflection layer between GaAs and sapphire, that reduces the amplitude of the laser intensity oscillations inside the film with a factor $\sim$2 as compared to the top panel. As analyzed in later sections, this is still far from ideal, and the results on the improved sample as presented in this chapter should be viewed as preliminary results. Investing more time into the search for a sample spot with far lower amplitude of the intensity oscillations should lead to more pronounced narrowing

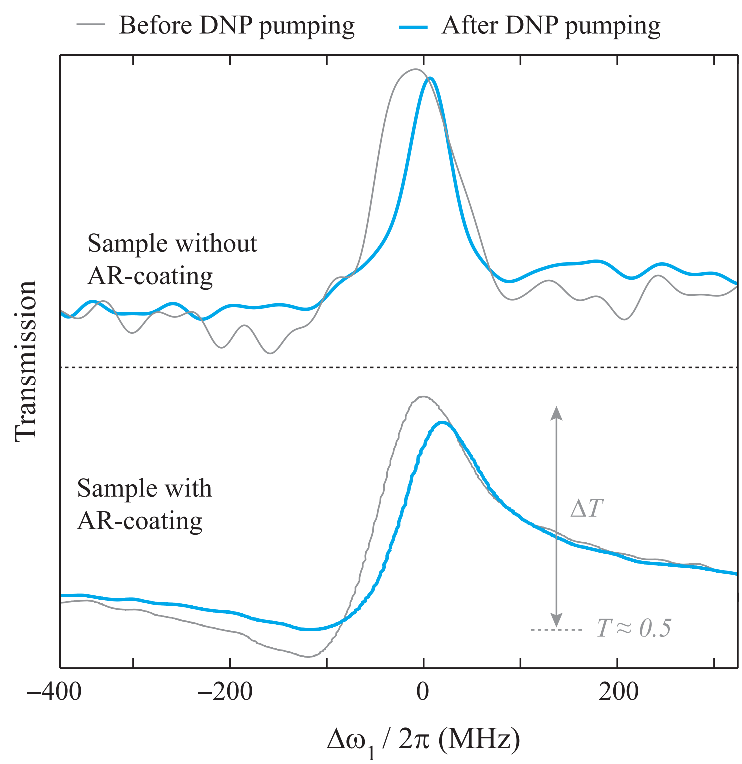

Figure 4.1: CPT traces after a period of two-laser DNP pumping at a detuning of 6 GHz. Similar traces before (gray lines) and after the pumping (blue lines) are shown for two different samples. The top traces were obtained while addressing an ensemble of donor-bound electrons in a 10-μm-thick GaAs film on sapphire without any anti-reflection coating, as used in chapter 3. Interference in the film gives rise to a standing wave intensity profile with an intensity modulation amplitude I_a that is 0.6 times the average intensity $\bar{I}$. The bottom traces were taken with a similar sample, with anti-reflection coatings to improve the uniformity of the laser intensities throughout the ensemble, to $I_a \approx 0.3\bar{I}$. Both CPT lineshapes after pumping reveal a distribution of the nuclear spin polarization that is stabilized at a reduced width as compared to equilibrium. The intensities during DNP pumping were $I_1 = 4.7$ Wcm^{-2} and $I_2 = 8.7$ Wcm^{-2} for the top panel, and $I_1 = 1.4$ Wcm^{-2} and $I_2 = 6.5$ Wcm^{-2} for the bottom panel. The change in transmission ΔT, as indicated by the gray arrow, quantifies the enhanced transmission at two-photon-resonance. $\Delta T \approx 0.1 \pm 0.05$ for all experimental traces in this chapter, where 1 is the transmission with the scanning laser detuned off-resonance from the optical transition (not visible in this figure). Measurement of the CPT traces were done at $I_1 = 0.6$ Wcm^{-2} and $I_2 = 2.2$ Wcm^{-2} for the top panel and $I_1 = 0.5$ Wcm^{-2} and $I_2 = 0.2$ Wcm^{-2} for the bottom panel.

of the CPT lineshape. The traces on this sample show a less noisy signal than the top panel. This can not be explained by the addition of the anti-reflection coating. Rather, it can be due to the difference in spotsize. We estimate that the spot diameter for the lower panel was $\sim$3 times larger than for the top panel. With increased spotsize, higher laser power is required to reach equal laser intensity, which increases the signal-to-noise ratio. The narrowing of the CPT lineshape is slightly less pronounced as in the top panel, and the transmission at the CPT peak has diminished as compared to before DNP pumping. Furthermore, we can clearly see an increased level of transmission for a broad detuning range red-detuned from the central CPT lineshape ($\Delta\omega_1/2\pi < -50$ MHz).

Overall, though improvements can be made with the sample with anti-reflection coating, we can still already conclude that the best suppression of nuclear spin fluctuations that we reach experimentally shows a mismatch with the values predicted by our model. We expect non-uniformities in the laser intensities to be the major cause of this mismatch.

4.3 Non-uniform intensity due to standing wave formation

Figure 4.2a schematically shows the intensity of a laser field that is focused on a thin GaAs film on a sapphire substrate. The laser has a spatial mode with a 2D-Gaussian transverse intensity profile: the lowest order transverse electromagnetic mode TEM_{00}. The GaAs film has two perpendicular surfaces, each reflecting light due to the mismatch in refractive index with the surrounding vacuum and sapphire. If the laser field inside the film is (partly) incident upon itself (typically when close to normal incidence and for film thickness order of magnitude or smaller than the focal volume of the laser), it gets a standing wave component with non-uniform spatial intensity. Figure 4.2b shows the same sample, where measures have been taken to improve the uniformity of the laser intensity throughout the film. The transverse Gaussian profile is shaped into a top-hat profile by a circular aperture in a gold mask blocking the light.

We simulated the intensity of a laser field propagating through the GaAs film as used in chapter 3, to analyze its spatial uniformity. Appendix A shows the approach that was taken for this simulation and explains how the refractive index of GaAs at wavelengths around the spectral lines of D^0X was approximated by fitting the free-exciton absorption. Figure 4.3a shows the impact of reflections in the GaAs film on the transmitted intensity and the spatial intensity distribution inside the film, as a function of laser wavelength. The top panel shows

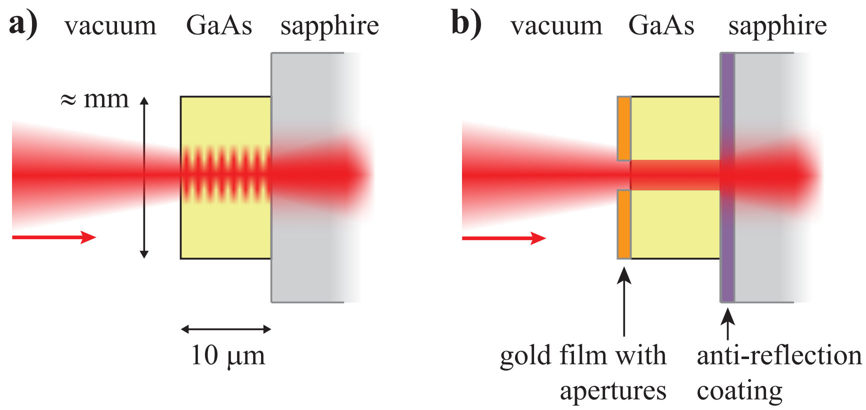

Figure 4.2: Schematic view of a laser field that is focussed on a GaAs film on sapphire. **a**, Reflections of the laser inside the GaAs at its interfaces with vacuum and sapphire result in standing waves in the film. This effect, combined with the Gaussian intensity profile of the laser field, creates a non-uniform spatial intensity distribution in the GaAs film. **b**, An (ideal) anti-reflection coating between GaAs and sapphire (fully) suppresses the non-uniformity of the laser field along the propagation direction. An aperture mask partly blocking the laser field, shapes the Gaussian intensity distribution into a top-hat profile, further improving the uniformity.

Fabry-Perot oscillations in the intensity of the transmitted light after the GaAs film, normalized by the intensity of the laser before the GaAs film. The transmitted signal is largest when an integer number of half wavelengths fits in the film, or in other words: when the laser is resonant with a mode of the weak cavity that the GaAs film forms. The Fabry-Perot pattern is chirped by a gradient in the refractive index, caused by the strong free exciton absorption at ∼8166.5 Å. This transmission signal closely resembles experimental data, as is shown in appendix A.

The other panels in figure 4.3a show the intensity distribution in the film along the propagation direction, revealing a standing wave pattern that changes with laser wavelength. The dotted white lines represent the lasers with wavelengths λ_1 and λ_2 used in two-laser CPT feedback, with a separation that resembles the electron Zeeman-splitting of D^0 at $B_{ext} \approx 6$ T. The first observation we make, is that the overall intensity at λ_2 inside the film is lower than at λ_1. However, we can correct for this difference by increasing the intensity at λ_2, since the ratio between maximum and minimum intensity is equal for both wavelengths. A second, more important observation is, that the spatial intensity distributions

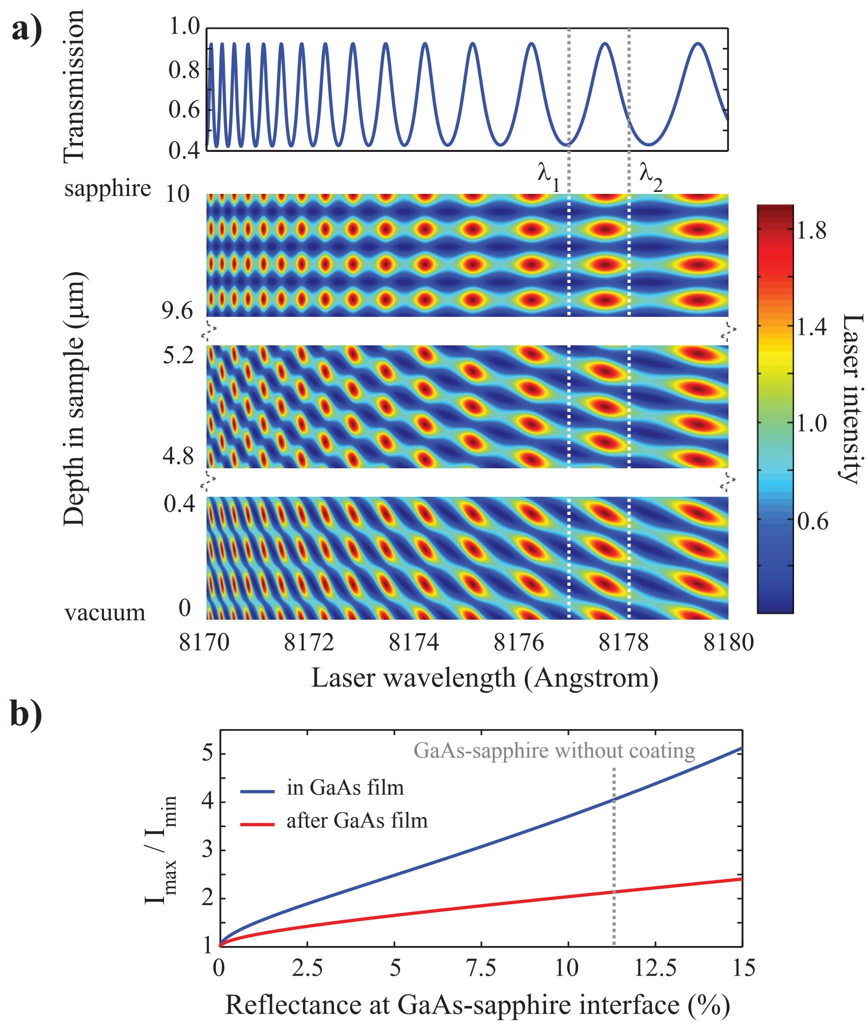

Figure 4.3: Simulations on standing waves inside a 10 μm thick GaAs film on sapphire, as shown in figure 4.2. **a**, Reflections at the vacuum-GaAs and GaAs-sapphire interfaces cause optical fields to form standing waves inside the GaAs film. The bottom three panels show the resulting intensity in the GaAs film as a function of laser wavelength and position along the propagation direction. The top panel shows the corresponding transmission signal after the GaAs film. The dotted lines (marked λ_1 and λ_2) show typical wavelengths for D^0X transitions used in two-laser DNP feedback. Intensities are normalized with respect to the intensity before the GaAs film. **b**, Ratio between maximum and minimum intensity of a laser field in the GaAs film (blue line) and the Fabry-Perot oscillations in the transmitted intensity after the GaAs film (red line), as a function of reflectance at the GaAs-sapphire interface. The dashed line marks the reflectance of a GaAs-sapphire interface without an anti-reflection coating.

for the two wavelengths do not overlap throughout the film. While the intensity pattern close to the GaAs-sapphire interface is equal for all wavelengths, deeper in the sample the positions that have maximum intensity are wavelength dependent.

A single optical defect at an arbitrary position in the GaAs will experience a single laser intensity anywhere between I_{min} and I_{max}, which are respectively the minimum and maximum intensity that a standing wave attains in the film. An ensemble of these defects in a two-laser experiment will experience all possible combinations of intensities I_1 and I_2 varying between I_{min} and I_{max}, with a probability distribution that depends on the overlap of the standing wave patterns (described in detail in appendix A). As a consequence, the ratio between intensities I_1 and I_2 varies with $(I_{max}/I_{min})^2$ throughout the ensemble. This is problematic for precise optical feedback on the defect ensemble, since the defect dynamics are strongly dependent on the (relative) intensities of the involved optical fields. A possible solution for this problem is to suppress the formation of standing waves by lowering the reflectance of the GaAs-sapphire interface. In practice, this could be obtained by placing an anti-reflection coating between the sapphire and the GaAs (see also chapter 5). Figure 4.3b shows the effect of the reflectance of the GaAs-sapphire on the ratio I_{max}/I_{min}, of both the spatial intensity distribution in the film (blue line) and in the Fabry-Perot spectrum in transmission (red line). The vertical dotted line marks the reflectance of GaAs on sapphire without an anti-reflection coating. We see that the spatial variations in intensity vanish when the reflectance goes to zero. Also, the magnitude of Fabry-Perot oscillations in transmission proves to be a good experimental probe to quantify the amount of intensity fluctuations inside the film.

4.4 Modeling two-laser CPT feedback with non-uniform laser intensities

In this section we simulate the behavior of the composite system of an ensemble of donor electrons and the nuclear spins surrounding them, under two-laser pumping at CPT conditions. Similar simulations in chapter 3 and reference [42] were performed with the assumption that all electron lambda-systems within the laser spot are addressed uniformly by the two lasers. Here, we specifically look at the case where blue-detuned feedback is applied to suppress nuclear spin fluctuations (at approximate optimal detuning $\Delta = 4$ GHz), but with a distribution of intensities that is non-uniform (and thus non-ideal) across the ensemble. Table 4.1 shows the parameters used for the simulations in this chapter. Note that for simplicity, we assume equal electric dipole moments for the optical transitions from the two electron ground states to their common bound-exciton excited state. As a result, equal intensities yield equal Rabi frequencies. The driving-laser frequencies during feedback are fixed such that they are exactly at two-photon resonance for electrons that feel an Overhauser shift of $\delta = 0$.

The hyperfine relaxation rate Γ_h, as used in equation 3.3, is proportional to the electron spin correlation time τ_c. This correlation time is modulated around CPT due to repeated excitation and spontaneous emission (as shown in figure 4.12 in the supplementary information). $\overline{\Gamma}_h$ is the equilibrium value for Γ_h in the absence of laser fields.

D^0-D^0X and sample parameters			
Γ_3	1 GHz	N	3×10^{13} cm^{-3}
γ_3	10 GHz	d	10 μm
Γ_s	0.1 MHz	T	4.2 K
γ_s	1 MHz	Δ	4 GHz
$\overline{\Gamma}_h/\Gamma_d$	0.01	$\mu_1 = \mu_2$	2.56×10^{-28} C m

Table 4.1: Simulation parameters for the dynamics of D^0-D^0X, for its interaction with the nuclear spin bath and for sample transmission.

4.4.1 Feedback with a Gaussian laser spot

We start our analysis by looking at the effect of a non-uniform transverse intensity profile on DNP feedback with an ensemble of donor-bound electrons. Instead of a laser spot with uniform intensity (top-hat profile), we use a spot that is radially falling-off as a Gaussian, where σ is the radius where the laser intensity has dropped with a factor $1/e^2$ as compared to its center value, see figure 4.4a. The two lasers have equal intensity at every donor electron, but throughout the addressed ensemble this intensity varies. As a result, the ensemble electron dynamics are driven by a non-uniform distribution of Rabi frequencies, dependent on the position of each electron in the laser spot.

To model the effect of this non-uniformity on the suppression of nuclear spin fluctuations, we divide the defect ensemble addressed by the laser spot in sub-ensembles. We approximate the Gaussian laser spot with a discrete set of concentric rings (up to at least $r = 2\sigma$), as shown schematically in figure 4.4a. We then assume that all donors in one ring experience the same laser intensity. Each ring now has its own probability distribution of Overhauser splittings $P(\delta)$ after two-laser feedback. To determine the overall nuclear spin configuration for the whole ensemble, we take a weighted sum of the $P(\delta)$'s of the separate sub-ensembles. Since we are interested in the light-ensemble interaction, the weight is the fraction of laser light a sub-ensemble receives, which is the area of its ring multiplied by the local intensity and normalized by the total laser intensity. As we discuss later in this section, this is not an exact description, but a good approximation for the collective ensemble transmission.

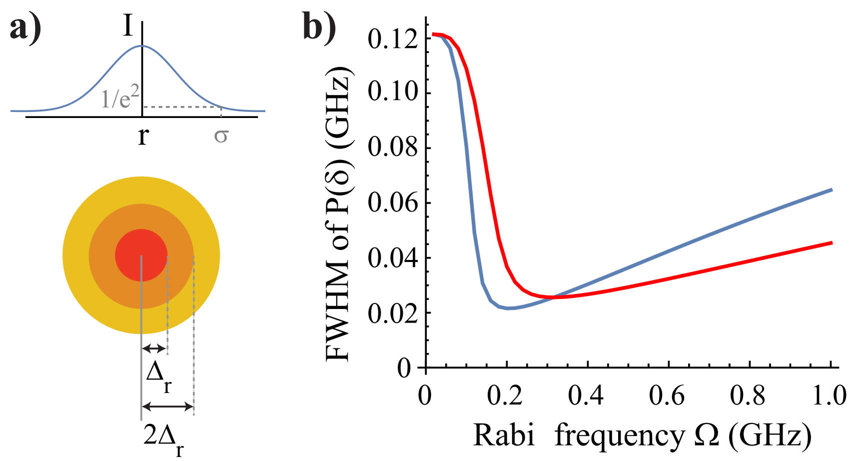

Figure 4.4: **a**, Intersection of a Gaussian intensity profile. For simulation purposes, the Gaussian profile is approximated as multiple concentric rings with constant intensity (we used ≈ 20 rings). **b**, Suppression of nuclear spin fluctuations, compared between pump lasers with a uniform intensity profile (blue line) and with a Gaussian TEM_{00} profile (red line) addressing an ensemble of bound-electrons. The lines show the full-width-half-max of the steady-state distribution of Overhauser shifts ($\mathrm{P}(\delta)$), after DNP pumping with two lasers at blue-detuned CPT conditions ($\Delta = 4$ GHz) and Rabi frequency Ω. For the Gaussian spot, Ω is the Rabi frequency at the center of the laser spot. The intensity profiles of the two laser fields overlap, leading to equal Rabi frequencies $\Omega_1 = \Omega_2$ at each electron.

Figure 4.4b shows the full-width-half-max (FWHM) of the distribution of Overhauser splittings after DNP feedback as a function of Rabi frequency Ω of the two driving lasers. We simulated this for both a laser spot with uniform intensity (blue line) and a Gaussian spot (red line). For uniform intensity, the ensemble is driven homogeneously and a single $P(\delta)$ is calculated for the steady-state distribution of nuclear spin polarization. The FWHM of 120 MHz at $\Omega = 0$ resembles the thermal distribution of nuclear spin polarization at 4.2 K. The distribution rapidly becomes narrower with increasing Rabi frequency, due to feedback on the nuclear spin polarization which drives the Overhauser splittings towards the stable point at $\delta = 0$, where DNP vanishes since the lasers are at two-photon-resonance and the electron spin polarization is at its equilibrium value. Feedback with uniform intensity is most effective at $\Omega \approx 0.2$ GHz, giving a distribution that is six times narrower than its thermal equivalent. For higher Rabi frequencies, the steady-state configuration of the nuclear spin broadens again, due to power broadening of the response of the electron spin polarization on Overhauser splitting (as in figure 3.1c) which diminishes the effective driving force around $\delta = 0$ for the narrowing of the nuclear spin configuration. An equal trend is found for a Gaussian laser spot, and gives a slightly broader distribution at the narrowest point ($\Omega \approx 0.35$ GHz), since only part of the ensemble is driven under ideal conditions. Remarkably, at higher Rabi frequencies the Gaussian spot shows less power broadening than the top-hat.

4.4.2 Feedback with unequal Rabi frequencies for the driving lasers

While a Gaussian transverse intensity profile causes the ensemble to experience a range of intensities, the field components of the two lasers are still equally strong at each individual donor. On the contrary, standing waves in the GaAs epilayer will cause the lasers to have unequal intensity along the propagation direction, as discussed earlier in this chapter. We will now study the effect of unequal Rabi frequencies on two-laser DNP feedback. To gain insight in the dynamics of the combined electron-nuclear spin system under asymmetric driving conditions, we simulate the situation where an ensemble of donor electrons is addressed with two lasers which are unequal but uniform in intensity. In other words: The laser fields have a top-hat profile and fixed ratio of I_2/I_1 throughout the film, and we study the behavior as a function of I_2/I_1.

Figure 4.5a shows the electron spin polarization $\langle S_z \rangle - \langle \bar{S}_z \rangle$ for a single donor addressed by two lasers around the CPT condition. An Overhauser shift $\delta \neq 0$ breaks two-photon resonance and causes the electron spin to polarize, as discussed in chapter 3. For equal laser intensities (blue line), the electron spin polarization is symmetric and opposite in sign around $\langle S_z \rangle - \langle \bar{S}_z \rangle = 0$. Transfer of momentum from the electron spin to the nuclear spin ensemble causes a driving force on the Overhauser shift, indicated by the blue arrows. We see that the Overhauser shifts are driven towards a stable configuration at zero nuclear spin polarization for a range of δ around $\delta = 0$. As the driving lasers become asymmetric in intensity (red and yellow line), the electron spin polarization becomes asymmetric with

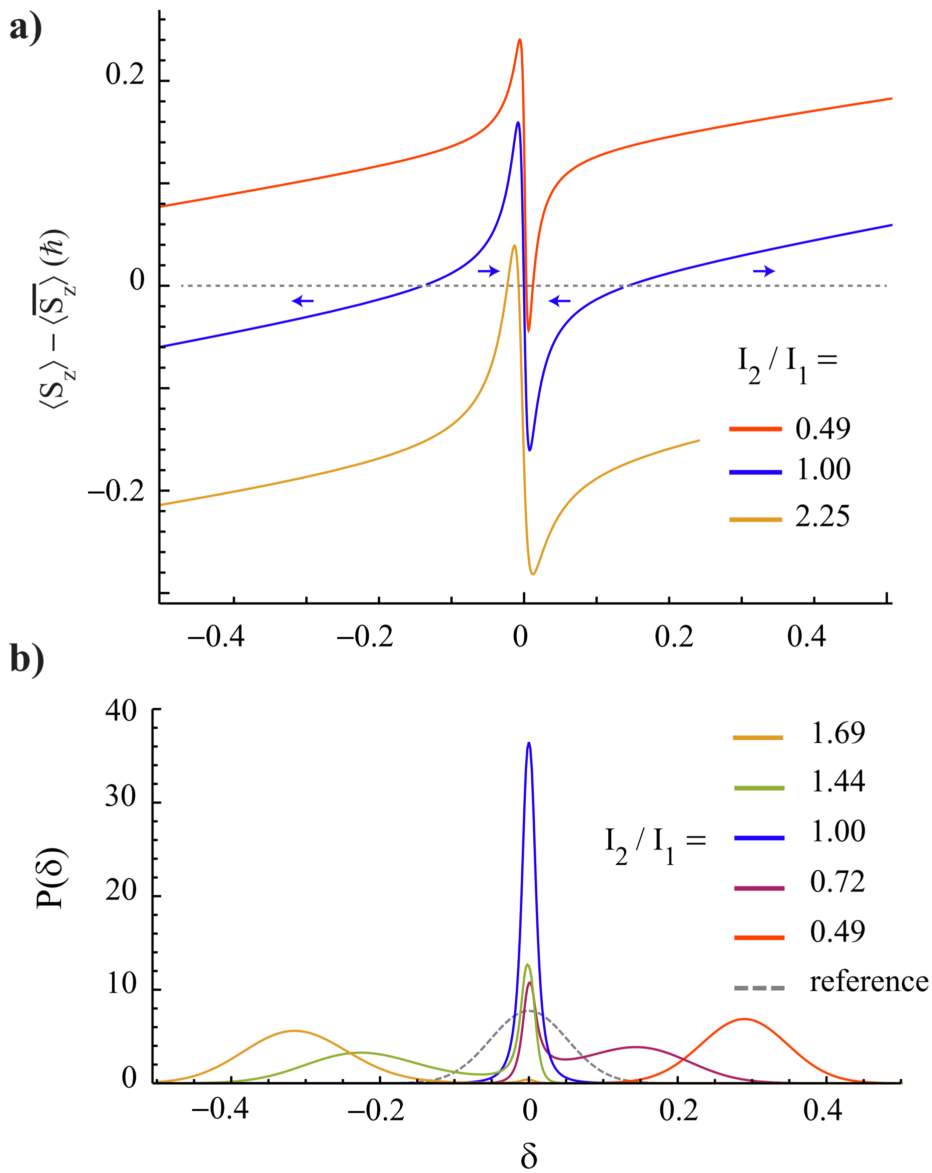

Figure 4.5: a, Out-of-equilibrium polarization $\langle S_z\rangle - \langle \bar{S_z}\rangle$ of a single electron spin, as a function of the Overhauser shift δ. The two driving lasers are at two-photon-resonance when $\delta = 0$. The blue (red and yellow) line shows the electron spin polarization for equal (unequal) laser intensities. **b**, Probability distribution $P(\delta)$ for the polarization of nuclear spin ensembles around donor-bound electrons, while two lasers at CPT condition are stabilizing the nuclear spin. Each line resembles a different ratio between the intensities of the lasers. The thermal nuclear spin configuration in the absence of stabilizing lasers is provided by the reference trace (dashed gray line).

δ. The stable point shifts very slightly away from $\delta = 0$. Moreover, the range of nuclear spin polarizations that experience a driving force towards this stable point becomes smaller.

We use these traces as non-linear driving terms to find the steady state solution of the stochastic behavior of the Overhauser shifts for the ensemble, described by a Fokker-Planck equation [47]. This yields the probability distributions of the nuclear spin polarization for asymmetric driving, shown in figure 4.5b. The thermal nuclear spin configuration (dashed gray line) is a Gaussian distribution centered around zero polarization. For equal intensity (blue line), the nuclear spin polarization is driven towards a distribution around the stable point at two-photon-resonance ($\delta = 0$) that is narrowed by a factor six as compared to the thermal distribution before feedback. For unequal intensities, only part of the nuclear spin ensembles is stabilized at zero polarization. The remaining ensembles are polarized and driven away from $\delta = 0$, appearing as additional broad lineshapes at finite polarization where the hyperfine rate of momentum transfer to the nuclei equals depolarizing relaxation and diffusion rates. Note that the feature at $\delta = 0$ has similar linewidth for all (a)symmetric driving intensities. What changes is the number of nuclear spin ensembles that occupies this stable point, which becomes less with increasing asymmetry.

4.4.3 CPT-lineshape dependence on non-uniform laser intensities

We now extend our study by looking at the transmittance of a 10-μm thick GaAs layer with a donor density of 3×10^{13} cm^{-3}, addressed by a distribution of asymmetric Rabi frequencies. The probability of a donor experiencing a specific combination of intensities I_1 and I_2 is described by a probability density function $P(I_1, I_2)$, as described in appendix A. Using the distributions of Overhauser shifts $P(\delta)$ for all sub-ensembles (as those in figure 4.5), we calculate the total sample transmission around CPT conditions. The equations governing the CPT lineshapes are described in the supplementary information. The interference of laser light inside the film that causes the standing wave pattern and non-uniform intensity, simultaneously gives rise to a Fabry-Perot (FP) effect in transmission, that shows up as an oscillation with laser frequency, as shown in figure 4.3a (top panel). For convenience, the influence of FP-oscillations on the calculated transmission signal are not accounted for, since they would make it harder to compare CPT lineshapes. That is, concerning the influence of FP-effects, we only account for the effect it has on the distribution $P(I_1, I_2)$ which drives the lambda systems.

The transmittance T_α of a medium has an exponential relation with the absorption coefficient α and the depth of propagation d, given by the Lambert-Beer law: $T_\alpha = e^{-d\alpha}$. As a consequence of the exponential relation, a CPT lineshape as observed in transmission scans has a smaller FWHM than its counter-image in α (which includes the complete behavior of our composite electron-nuclei system and is a direct probe of $P(\delta)$). However, we simulate in a regime ($\alpha d \approx 0.7$) where the mismatch between the lineshapes in absorption coefficient and transmission is negligible. Only for values of αd an order of magnitude higher than our typical values, one starts to find a few percent difference in FWHM. We can therefore safely ignore this effect in the following paragraphs.

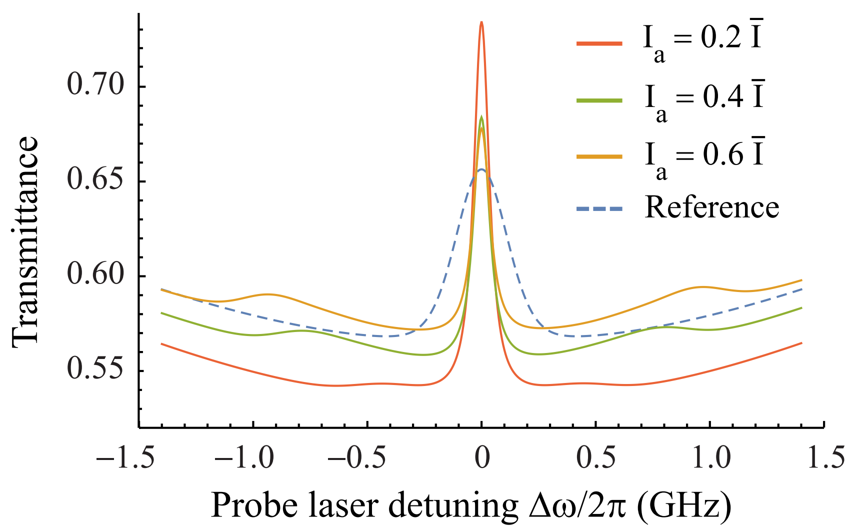

Figure 4.6: Calculated CPT traces in transmission for a 10-μm thick GaAs layer with a donor density of 3×10^{13} cm^{-3}, before (dashed line, labeled 'reference') and after DNP feedback, with an electron ensemble that feels an intensity distribution given by a standing wave pattern. Each trace shows the CPT lineshape for a different amount of intensity variation throughout the ensemble, provided by the amplitude I_a of the standing wave pattern, expressed as a fraction of the average intensity $\bar{I}$ (giving a $\bar{I} - I_a$ to $\bar{I} + I_a$ peak-to-peak modulation). $\bar{I}$ is equal for all traces and chosen such that it corresponds to a Rabi frequency of 0.2 GHz. A top-hat profile was used for the transverse intensity distribution. We used $I_a = 0.6\bar{I}$ for the reference trace.

Figure 4.6 shows simulated CPT lineshapes as observed in transmission after DNP feedback, with ω_2 kept fixed and ω_1 scanned around two-photon resonance, for three standing wave patterns with different modulation amplitudes and a transverse intensity profile that is constant (top-hat). The standing wave pattern with the largest amplitude (yellow line) has a modulation similar to that in a GaAs film on sapphire (compare with figure 4.3b). As a reference, the CPT lineshape before feedback is provided for the same intensity pattern ($I_a = 0.6\bar{I}$). CPT after DNP feedback shows a central peak with a factor ~3 narrowed lineshape as compared to the reference lineshape: a signature of improved inhomogeneous dephasing time for the electron spin ensemble. However, broad side humps appear around $\Delta\omega/2\pi = 0.8$ GHz, slightly increasing transmission across the whole scan range. These humps indicate CPT conditions for donor electrons with Overhauser shifts that are driven away from $\delta = 0$ during DNP pumping (as in figure 4.5). Decreasing the amplitude of the standing wave pattern gradually lowers the amount of donors with (slightly) polarized nuclear spin baths and increases the occupancy of the stable configuration at $\delta = 0$, thereby increasing the transmission at the central CPT peak.

Finally, we simulate CPT transmission traces for a distribution of laser intensities $P(I_1, I_2)$ that incorporates both a standing wave pattern and a transverse Gaussian profile. Figure 4.7 presents transmission traces for a GaAs film on sapphire as used in our experiments, for different combinations of an aperture on GaAs and anti-reflection coating at the GaAs-sapphire interface to improve the uniformity of the laser intensity. Six cases are presented: the transverse intensity profile being either a Gaussian or a top-hat with constant intensity (i.e. the limit of an ideal aperture), combined with three standing waves ranging from an intensity oscillation amplitude of $I_a/\bar{I} = 0.6$ for a GaAs film on sapphire without AR-coating to a constant intensity ($I_a = 0$) for an ideal AR-coating. The average laser intensity $\bar{I}$ in the standing wave pattern at the center of the laser spot is equal for all cases, and corresponds to a Rabi frequency $\Omega = 0.2$ GHz.

For every case we compare the CPT lineshapes before (dashed blue line) and after DNP feedback (orange line). All traces show the broad optical lineshape and an enhanced CPT transmission peak at zero detuning, associated with two-photon resonance, with peak height expressed as h and h_{ref}, respectively, for the trace after DNP-pumping and the reference trace at thermal equilibrium. The factor h/h_{ref} by which the peak height has changed after pumping is given in each panel. The top two panels, for samples without anti-reflection coating, barely show an increase in peak height after pumping. Instead, the transmission is slightly increased at regions outside the CPT transmission window ($|\Delta\omega/2\pi| >$ 0.3 GHz), due to a range of asymmetric intensities in part of the donor ensemble, driving the Overhauser shift away from $\delta = 0$ and causing side bumps as in figure 4.6. When the standing wave amplitude is reduced, the side

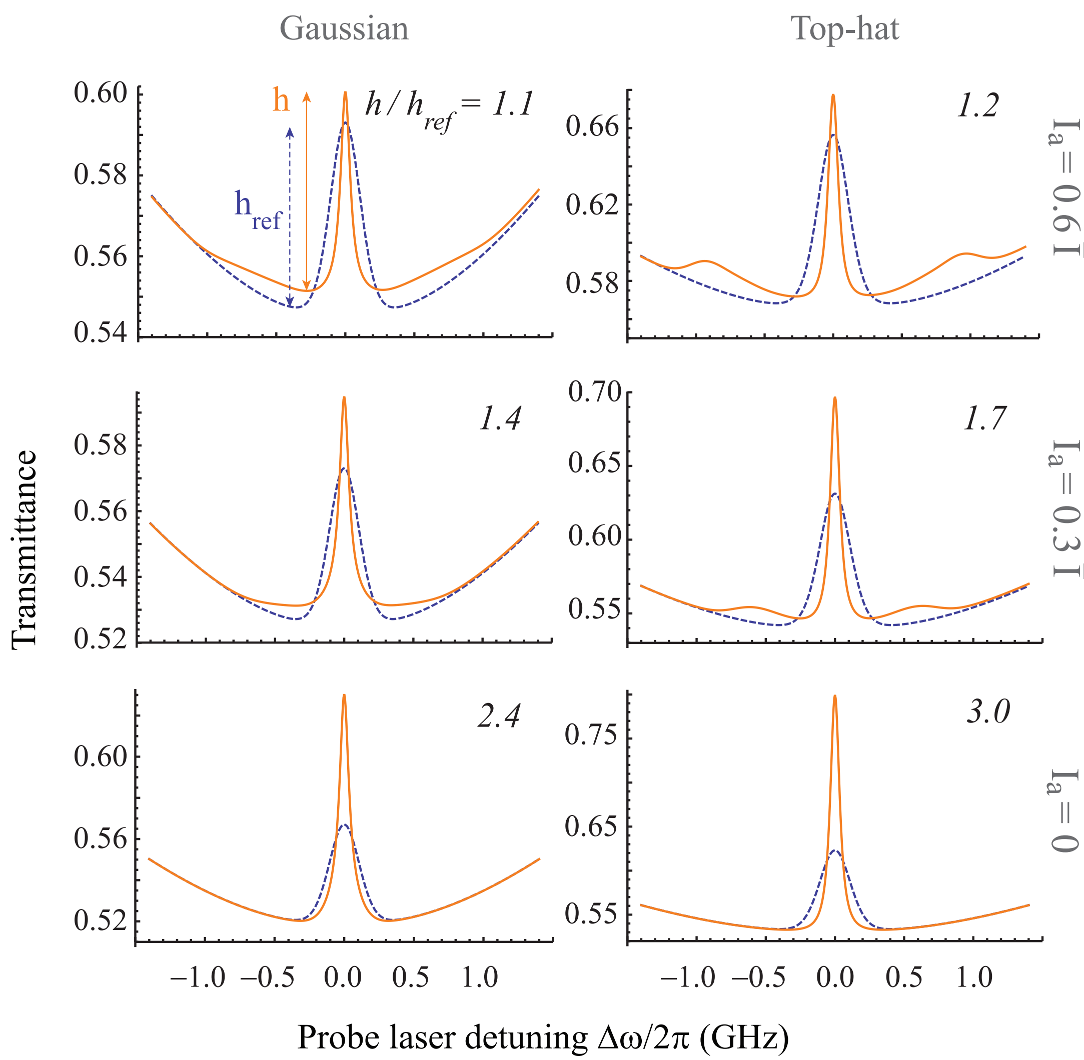

Figure 4.7: Calculated transmission traces as in figure 4.6, showing CPT before (dashed line) and after (yellow solid line) DNP pumping with $\Omega = 0.2$ GHz, for different combinations of an anti-reflection (AR) coating and/or aperture to improve laser uniformity. Three values for the standing wave are simulated: $I_a/\bar{I} = 0.6$ (no AR-coating), 0.3 and 0 (ideal AR-coating). Hence, the top-left panel shows CPT for a sample without any improvements and the bottom-right panel shows CPT for a uniform intensity distribution. The transmission traces were simulated with identical intensities as used during DNP pumping. The top-left panel indicates the height of the central CPT peak h (h_{ref}) for the trace after (before) DNP pumping. Each panel includes in the top-right corner the factor h/h_{ref} by which the peak height is increased.

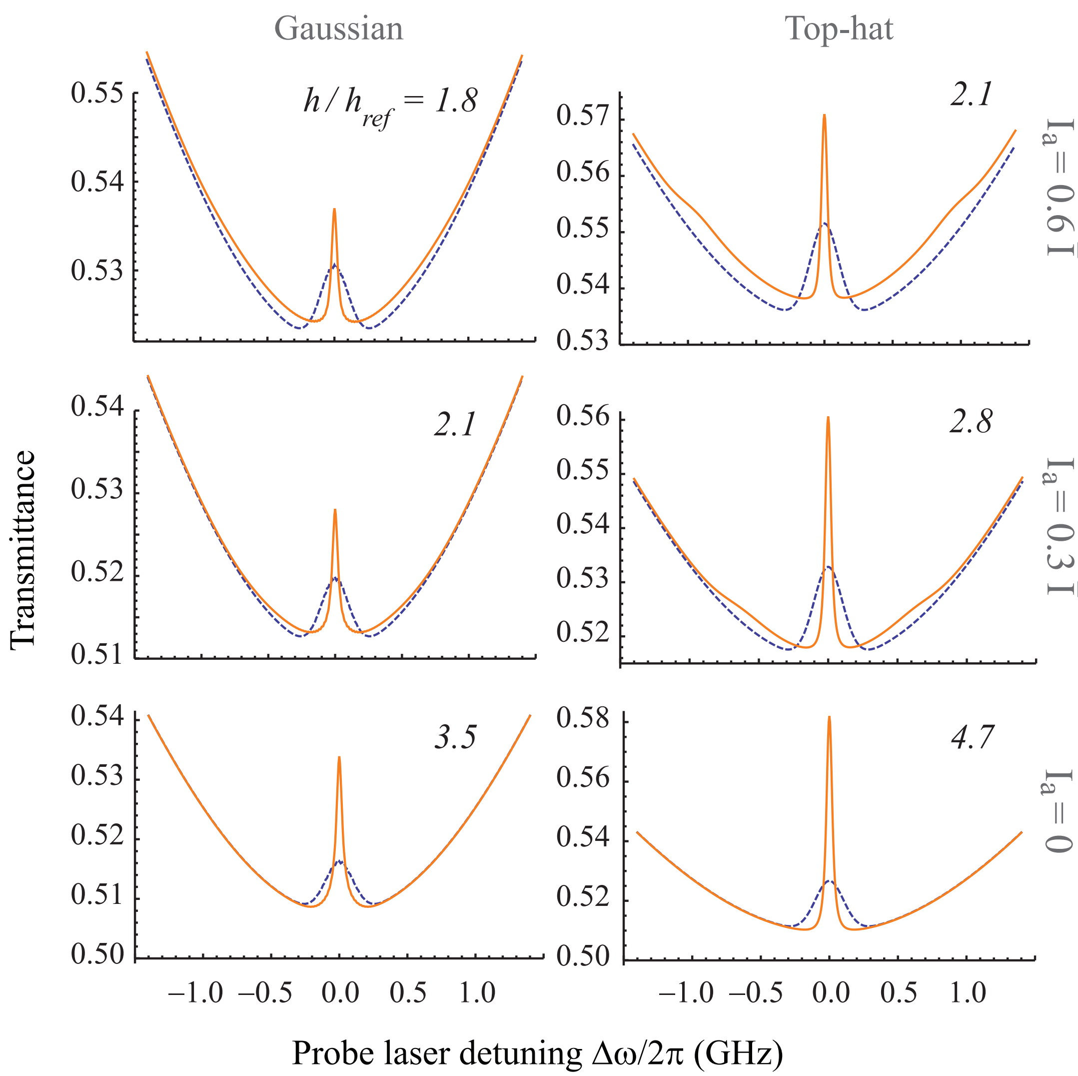

Figure 4.8: Calculated transmission traces showing CPT before (dashed line) and after (solid line) DNP pumping with equal intensity distributions, as in figure 4.7. In contrast to figure 4.7, the transmission traces after pumping are simulated with intensities that are a factor 0.16 of those during pumping.

bumps become less pronounced and the peak height after pumping grows. In the absence of standing waves, the peak height increases by a factor ∼3 after pumping. Also, transmission outside the CPT window has become identical before and after DNP-pumping, indicating that all nuclear spin ensembles are now driven towards zero polarization. The reason for this trend is of course the reduction of asymmetric laser intensities with decreasing amplitude of the standing wave oscillations.

Going from a Gaussian intensity to a top-hat profile has only a small effect on the change in peak height. However, the absolute CPT peak heights are a factor two smaller for the Gaussian profile. This is due to the outer regions of the Gaussian spot, where the intensity during CPT scans is high enough to significantly contribute to the transmission signal, but too low to induce CPT. Note that for the top-left panel, the narrowed central peak and the increased transmission in the adjacent regions agree qualitatively with the experimental observations presented in figure 4.1.

When we look at the linewidth of the central CPT peak, we observe a factor ∼3 narrowing after DNP-pumping as compared to the reference trace for all the panels alike. Neither using apertures to shape the Gaussian beam profile into a uniform top-hat, nor reducing the standing wave amplitude improves the sharpness of the CPT lineshape, while we know from earlier sections that the underlying distribution of nuclear spin polarizations has narrowed by a factor ∼6 after feedback, at least for the ideal case of a top-hat with $I_a = 0$. Since we already ruled out the effect of the exponential behavior of transmittance on the CPT lineshape, the reason for this mismatch must be sought in the intensities with which we take transmission traces. We included an analysis on the influence of CPT laser intensity on the linewidth in transmission in the supplementary information. We conclude that taking CPT with equal intensities as for ideal pumping ($\Omega = 0.2$) causes power broadening of the two-photon resonance of individual bound-electrons, which prevents us from measuring the lowest values for the linewidth of the underlying $P(\delta)$.

Figure 4.8 shows identical simulations as figure 4.7, with the only difference that CPT transmission traces are taken with lower intensities, namely a factor 0.16 of those used in figure 4.7. CPT is now a factor ∼4.5 narrower after DNP pumping, indicating that the effect of power broadening is reduced. Remarkably, the difference in peak height between before and after pumping is much larger than with higher CPT intensities, for all six cases. For the case with a Gaussian profile and $I_a/I_{bar} = 0.6$, the peak height already doubles after pumping and for the ideal case we get a factor 5 increase in peak height. We still do not observe the factor ∼6 narrowing as observed in $P(\delta)$. Further lowering the intensities with which CPT scans are performed will completely eliminate power broadening, although we should note that that will also deteriorate the CPT peak height and hence the signal-to-noise ratio when measuring CPT in experiments, especially for the CPT lineshape before DNP pumping.

Overall, we assess the behavior as observed in figures 4.7 and 4.8 as follows:

Our simulations on DNP pumping with distributions of asymmetric pump intensities explain the lack of transmission increase for the CPT peak and also partly the low narrowing factor found in our experimental results. Shaping the laser fields into top-hat profiles thus far seems of less importance than the prevention of asymmetric driving-laser intensities. Therefore, finding a sample spot where the anti-reflection coating works optimal has priority over the application of apertures, especially since a gold film with apertures could prove problematic in finding a reasonable sample spot. Although the top-left transmission trace in figure 4.7 looks similar to the experimental traces in figure 4.1, we still obtain a much more pronounced narrowing in the simulations. Since the experimental traces were taken with CPT intensities that were much lower than the pumping intensities, we can not attribute this difference to power broadening. We cannot explain this remaining mismatch in the narrowing factor of the CPT peak with non-uniform laser intensities and attribute it to a value of $\overline{\Gamma}_h/\Gamma_d$ used in simulations that is different from the real situation. Earlier simulations [42] found an empiric relation between the increase in inhomogeneous spin dephasing time and $\overline{\Gamma}_h/\Gamma_d$, as can be found in the supplementary information. Using this relation, we see that narrowing of $P(\delta)$ by a factor $\sim$2 indicates that $\overline{\Gamma}_h/\Gamma_d \approx 0.001$, an order of magnitude lower than initially assumed and used in our simulations.

4.4.4 Simulation conclusions

Our simulations lead us to conclude the following: with values as tabulated in table 4.1 for the strength of the hyperfine interaction in D^0X and for the diffusion rate of angular momentum between the nuclear spin at the donor and the bulk nuclear spin bath, simulations show a factor $\sim$6 increase in electron spin dephasing time, for ideal driving circumstances. Non-uniform laser intensities with spatial distributions that overlap for the two lasers, as for Gaussian beam profiles, only slightly deteriorate this. In this situation, DNP feedback still focuses all Overhauser splittings into a low entropy distribution around zero polarization, but with a driving force that is at the optimal achievable level for only part of the electron ensemble.

Intensity distributions where the intensity patterns of the lasers do not overlap, as for standing waves in our samples, pose a more severe problem. Donor systems that are driven asymmetrically in part polarize the surrounding nuclear spin, much like single-laser DNP in D^0X. On the ensemble level, part of the nuclear spin is successfully driven towards zero polarization; the rest is polarized into the broad side bumps. The sub-ensemble of electrons with Overhauser fields in the narrow distribution around $\delta = 0$ now has an increased spin coherence time. However, this does not yield a CPT peak with transmittance that is close to the ideal value of 1, since two-photon resonance for the coherent sub-ensemble overlaps with single-photon transitions for the less coherent other part of the ensemble. This is still compromising quantum information protocols that rely on the interaction of single photons with such an ensemble. For example, Raman photons correlated with spin flips in a solid-state ensemble can only exit when at CPT resonance with the laser field that induced the spin flips [9, 30]. Raman photons scattered by the coherent sub-ensemble have a high probability of being reabsorbed in a single photon transition by a donor-electron with a different ground-state splitting, as reflected by the non-ideal transmission at the center of the CPT peak. While the coherence of Raman photons that do exit the sample is unaffected, their yield is low, limiting practical applications.

To obtain CPT that is simultaneously spectrally sharp and has a transmittance close to unity, $P(\delta)$ needs to be driven towards a configuration that is more than a factor $\sim$6 narrower as compared to its thermal state. In order to make this happen, the ratio $\overline{\Gamma}_h/\Gamma_d$ has to be increased, by choosing a material with less nuclear spin, by preventing nuclear spin diffusion (as in self-assembled InAs quantum dots in GaAs [39]), or by changing the experimental conditions. In the case of the D^0 system, lowering the magnetic field decreases the mismatch between electron spin and nuclear spin precession frequencies [75], which enhances Γ_h.

On the other hand, increasing the magnetic field could potentially decrease the nuclear-spin diffusion rate Γ_d during pumping. Figure 3.5 showed how nuclear spin diffusion is suppressed by the Knight field caused by the electron spin which is (partly) polarized during almost the whole CPT scan, except around two-photon resonance (see also figure 4.5a). Because DNP pumping is performed at two-photon resonance, it is not possible to maintain a substantial Knight field during DNP pumping by making the Rabi frequencies asymmetric. Even for asymmetric Rabi frequencies, DNP feedback still drives the nuclear spin configuration towards a point where $\langle S_z \rangle - \langle \overline{S_z} \rangle_{eq} = 0$, since this condition defines the stable point where the DNP rates are zero and where $P(\delta)$ converges to (close to $\delta = 0$). The thermal-equilibrium electron spin polarization $\langle \overline{S_z} \rangle_{eq}$ is approximately zero for high temperatures and/or small magnetic fields ($\hbar\omega_z < k_B T$), so in this case also $\langle S_z \rangle$ is zero at the stable point, resulting in a nullified Knight field. Increasing the magnetic field or lowering the temperature creates a non-zero $\langle \overline{S_z} \rangle_{eq}$, and hence a non-zero $\langle S_z \rangle$ for $\delta = 0$, resulting in a Knight field. This way, Γ_d is suppressed at the stable point for $P(\delta)$, which will increase the narrowing factor that can be achieved. Figure 4.14 in the supplementary info shows $\langle \overline{S_z} \rangle_{eq}$ as a function of magnetic field for D^0X at a temperature of 4.2 K.

For future research, it is interesting to look into the dependence of Γ_h and Γ_d on magnetic field, and perform blue-detuned DNP pumping experiments over a range of magnetic field values.

4.5 Intensity dependence of CPT lineshape narrowing

To validate the numerical explorations of the previous sections, we present here further experiments where we vary the relative and absolute values of the two pump laser intensities during DNP feedback and study the resulting narrowing of the CPT lineshape.

Figure 4.9a shows transmission traces after blue-detuned pumping periods of 5 minutes, for different ratios of pump laser intensities. I_2 was kept constant at 6.5 Wcm^{-2}, while I_1 was varied with steps of 1.4 Wcm^{-2}. Intensities during spectral recording of CPT peaks were $I_1 \approx 0.5$ Wcm^{-2} and $I_2 \approx 0.2$ Wcm^{-2} for all traces, and a reference trace before pumping (thin gray line) is shown for comparison. The trace with the most asymmetric pump intensities (light-blue, same as in figure 4.1 bottom panel) is the only trace with a narrower CPT lineshape than the reference trace, indicating suppressed fluctuations of the nuclear spin polarization. Increasing the value of I_1 result in a CPT lineshape with lower peak height and increased transmission at negative detuning from the central CPT peak ($\Delta\omega_1/2\pi \in [-250, -50]$ MHz). This corresponds to a shift in nuclear spin polarization towards positive δ, for part of the electron ensemble. Combined with the simulations presented in figure 4.5b, where it was shown that part of the nuclear spin polarizes towards positive delta when Rabi frequencies $\Omega_2/\Omega_1 < 1$ (or in our simulations when $I_2/I_1 < 1$, since we assumed equal optical transition dipole moments $\mu_1 = \mu_2$ there), this suggests that $\Omega_1 \approx \Omega_2$ for the light-blue trace and $\Omega_2/\Omega_1 < 1$ for the other traces. Besides providing an indication for the optimal ratio of laser intensities, the results in figure 4.9a validate the trends predicted by our model for asymmetric driving lasers.

We can use the dependence of the CPT lineshape on relative laser intensities to make a estimation of the ratio μ_2/μ_1 of the transition dipole moments in D^0X. If the pump intensities that result in narrowing ($I_2/I_1 = 4.6$) correspond to equal Rabi frequencies $\Omega_1 \approx \Omega_2$, it follows that $\mu_1 \approx \sqrt{4.6}\ \mu_2 \approx 2.1\ \mu_2$. If we take the same approach for the measurements on a different sample, as presented in

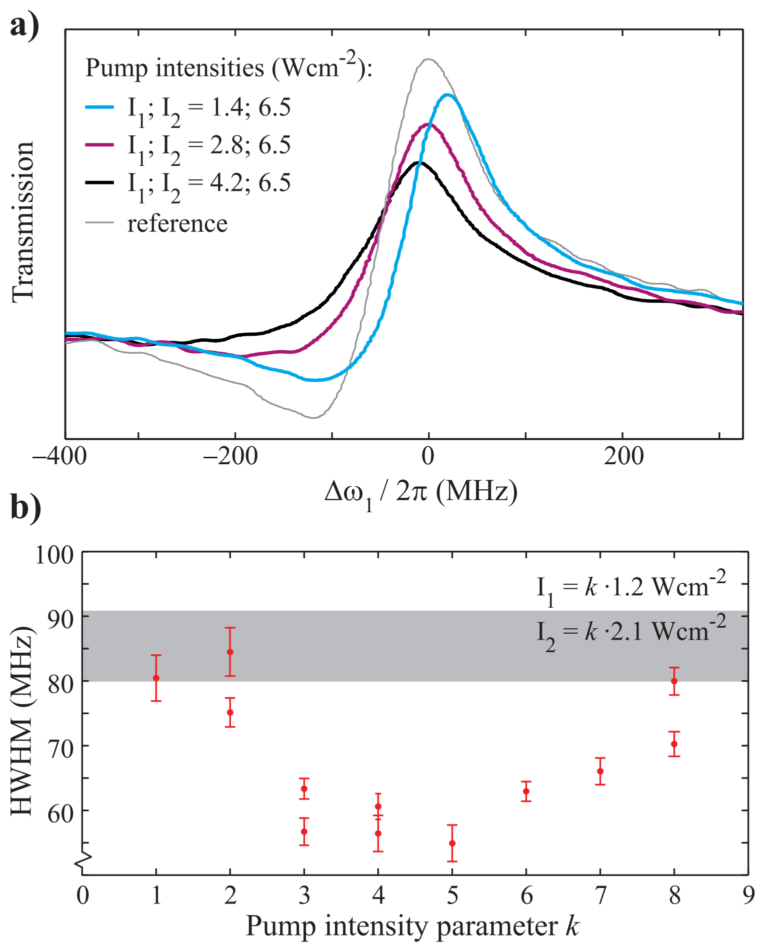

Figure 4.9: **a**, CPT traces after blue-detuned DNP pumping for a period of 5 minutes at a single-photon detuning of $\Delta = 6$ GHz, with varying laser intensities. The reference trace (thin gray line) was taken without a pump period, representing the ensemble equilibrium distribution of the nuclear spin polarization. The intensity during pumping $I_2 \approx 6.5$ Wcm^{-2} (for the laser with frequency ω_2 in figure 3.1) was equal for all traces, while pumping intensity I_1 was varied, as shown in the legend. Laser ω_1 was scanned to probe the CPT lineshapes. Intensities during the measurement of CPT traces were equal for all traces, with $I_1 \approx 0.5$ Wcm^{-2} and $I_2 \approx 0.2$ Wcm^{-2}. **b**, Half-width-half-max of CPT lineshapes as a function of pump intensity (in multiples of $I_1 \approx 1.2$ Wcm^{-2} and $I_2 \approx 2.1$ Wcm^{-2}). The CPT lineshapes were fit with a single Gaussian. The error bars show the 95%-confidence intervals of these fits. All CPT traces were taken with $I_1 \approx 0.6$ Wcm^{-2} and $I_2 \approx 2.2$ Wcm^{-2}. The gray bar indicates the region wherein reference traces without DNP pumping lie.

the top panel of figure 4.1, we obtain $\mu_1 \approx 1.4\ \mu_2$. Earlier work on experimental photoluminescence data on CPT in the same system by Fu *et al.* [18] implicates that $\mu_1 \approx 10\ \mu_2$. While these values agree on which transition has the bigger dipole moment, the results do not yet establish a precise value for the ratio μ_2/μ_1.

Figure 4.9b presents experimental results on the dependence of CPT lineshape narrowing as a function of absolute laser intensity, for the intensity ratio near the optimal value (here kept constant at $I_2/I_1 \approx 2$). The half-width-half-max of CPT lineshapes is fit after DNP pumping periods where I_1 and I_2 are varied. All CPT traces were taken at the same laser intensities $I_1 \approx 0.6$ Wcm^{-2} and $I_2 \approx 2.2$ Wcm^{-2}. We see that narrowing of the CPT lineshape as compared to the equilibrium situation (depicted by the gray bar) only occurs for a small range of laser intensities. The trend of the linewidth as a function of pump laser intensity agrees with the simulations presented in figure 4.4b, except for the factor of narrowing.

4.6 Build-up of the narrowed CPT lineshape

At the end of chapter 3, we presented results on the build-up and decay of the split CPT lineshape after red-detuned DNP pumping. The dynamics for red- and blue-detuned driving are of course governed by the same equations, with at the basis the rate of change of the Overhauser shift for a single electron (equation 3.3), which includes the DNP and nuclear spin diffusion rates Γ_h and Γ_d. These rates are different for the red- and blue-detuned pumping, especially since the hyperfine DNP rate Γ_h drops sharply around two-photon resonance at $\delta = 0$ [75], which influences the blue-detuned narrowing but not so much the red-detuned splitting of $P(\delta)$. Furthermore, the amount of angular momentum that is exchanged between the electron spins and the nuclear spin bath to go from the thermal situation to the split nuclear spin configuration is different than the amount to go to the narrowed distribution. In this short section, we therefore check the evolution of the CPT lineshape during build-up.

Figure 4.10 shows the time evolution of the CPT linewidth under pumping conditions that narrow the lineshape. These results were obtained with the same sample as in figure 4.9b, without anti-reflection coating, and with pump intensities $I_1 = 6$ Wcm^{-2} and $I_2 = 11$ Wcm^{-2}, corresponding to pump intensity parameter $k = 5$ in figure 4.9b. CPT transmission traces were taken after pumping periods with increasing duration and the CPT peaks were fit with a single Gaussian function to obtain the half-width-half-max of the lineshape. Each data

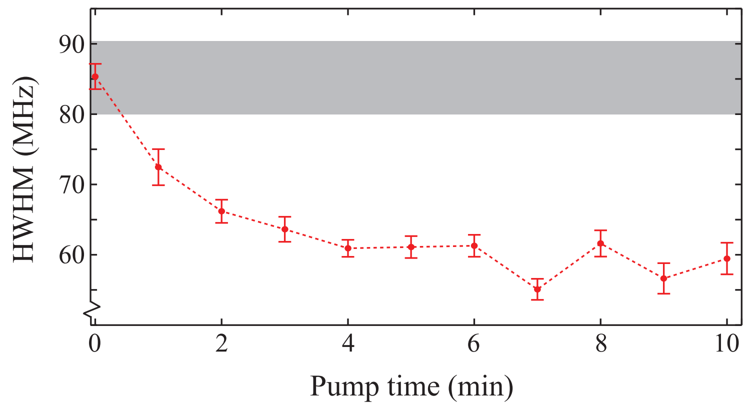

Figure 4.10: **a**, Half-width-half-max of CPT lineshapes similar as in figure 4.9b, showing the evolution of the CPT lineshape with DNP pump duration. Each datapoint was preceded by a new pump period, at intensities that show the thinnest lineshape in figure 4.9b ($I_1 \approx 6.0$ Wcm^{-2} and $I_2 \approx 10.5$ Wcm^{-2}). The error bars show the 95%-confidence intervals of the fits. The CPT traces were taken with $I_1 \approx 0.6$ Wcm^{-2} and $I_2 \approx 2.2$ Wcm^{-2}. The gray bar indicates the region wherein reference traces without DNP pumping lie.

point was preceded by a new pump period (and before that first a dark period of 5 minutes, to let the nuclear spin configuration relax to thermal equilibrium). Surprisingly, the CPT linewidth stabilizes after ~4 minutes, which is equal to the build-up time found for the splitting observed for red-detuned driving in chapter 3. To understand the independence of this timescale, further analysis of the role of the Knight field during build-up for donor-systems that are still at $\delta \neq 0$ (i.e. far away from the stable points where $\langle S_z \rangle \neq 0$) is necessary.

Acknowledgements

We thank Maarten Degen for valuable discussions and for his contribution to simulations on DNP feedback with non-uniform intensity distributions, as part of his master-thesis research.

Supplementary Information

Power broadening of CPT lineshapes

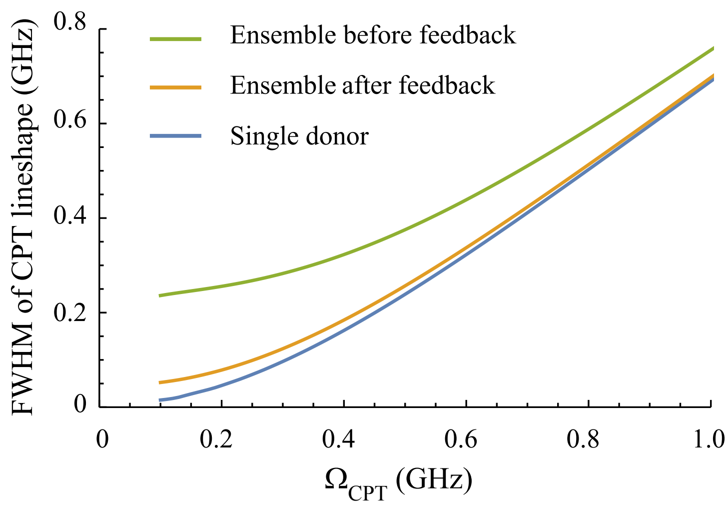

Figure 4.11: FWHM of the CPT lineshape observed in transmission for a 10 μm thick GaAs layer with a donor density of 3×10^{13} cm^{-3} as a function of the Rabi frequency Ω_{CPT} during the CPT scan (Ω_{CPT} is equal for both lasers). As a reference, the CPT lineshape of a single electron in absence of nuclear spins is simulated (blue line). It shows power broadening at high Ω_{CPT}, and dictates the lower limit of the CPT linewidth for an ensemble of donor electrons. In the limit where $\Omega_{\mathrm{CPT}} = 0$, its FWHM directly reflects the homogeneous coherence time of a single electron spin. The (green) yellow line shows the CPT width (before) after two-laser feedback with both lasers at $\Omega = 0.2$ GHz, for an ensemble of donor electrons. Here, uniform Rabi frequencies were assumed, i.e. the laser intensity profile is described by a top-hat and no standing waves occur.

Transmission of an ensemble of optical impurities addressed by a distribution of laser intensities

We take an ensemble of optical impurities, which is addressed by two non-uniform laser fields. The non-uniformity of fields is described by the intensity probability distribution $P(I_1, I_2)$. The normalized transmission of two lasers with total intensity I_0 before a sample with thickness z, is:

$$T_{trans}(\omega_1, \omega_2) = \frac{1}{I_0} \iint P(I_1, I_2) \left[I_1 \, e^{-z\alpha_1(\Omega_1, \Omega_2, \omega_1, \omega_2)} + I_2 \, e^{-z\alpha_2(\Omega_1, \Omega_2, \omega_1, \omega_2)} \right] dI_1 dI_2,$$

(4.1)

where α_i is the non-linear absorption coefficient for laser i, given by:

$$\alpha_i(\Omega_1, \Omega_2, \omega_1, \omega_2) = \frac{\omega_i}{c} \int P(\delta)_{\Omega_1\Omega_2}\ \mathrm{Im}\left[\chi_i(\Omega_1, \Omega_2, \omega_1, \omega_2, \delta)\right]\, d\delta \tag{4.2}$$

with χ_i determined by a density matrix approach [38]. $P(\delta)_{\Omega_1\Omega_2}$ is the probability distribution for the nuclear spin polarization after DNP feedback with the specific pumping Rabi frequencies Ω_1 and Ω_2.

Hyperfine relaxation rate Γ_h

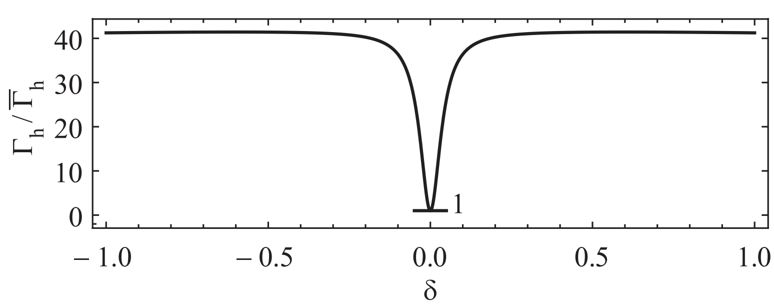

Figure 4.12: Figure adopted from [41]. Modulation of the hyperfine relaxation rate Γ_h by the Overhauser shift δ under conditions of two-laser driving. The simulations parameters are as in table 4.1.

Dependence of $T_2^*/\bar{T}_2^*$ on $\overline{\Gamma}_h/\Gamma_d$

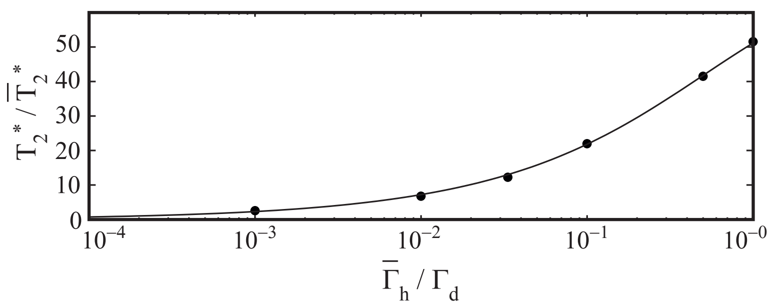

Figure 4.13: Figure adopted from [41]. Simulations on the suppression of nuclear spin fluctuations and the resulting increase in the inhomogeneous electron spin dephasing time, for six values of Γ_h/Γ_d.

Equilibrium electron spin polarization with magnetic field

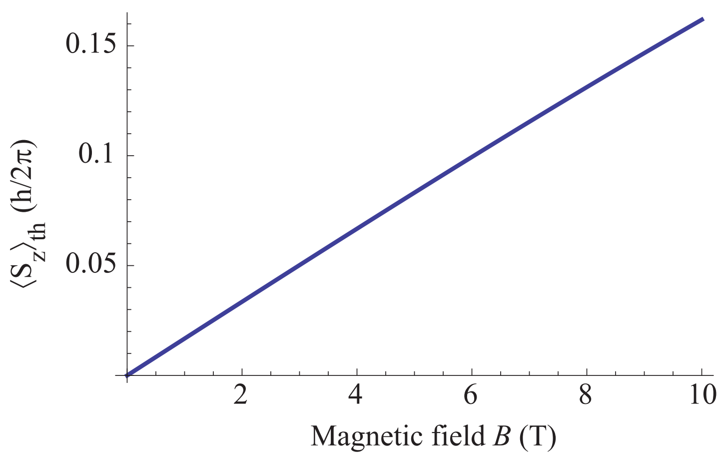

Figure 4.14: Thermal equilibrium electron-spin polarization for D^0 in GaAs as a function of external magnetic field B at a temperature of 4.2 K. The formula for this graph is given by equation 4.3

$$\langle S_z \rangle_{eq} = \frac{1}{2} \tanh\left(\frac{g\mu_B B}{2k_B T}\right) \tag{4.3}$$

Chapter 5

Fabrication and characterization of samples for uniform ensemble-light interaction

Abstract

This chapter treats the fabrication and characterization of gallium arsenide epilayers on sapphire that allow for uniform optical addressing of an ensemble of impurity-bound spins with a homogeneous strain environment. We show how *differential interference contrast microscopy* at 300 K and spatial single-laser transmission scans at 4.2 K can be used to produce a spatial image of strain homogeneity in the GaAs layer. We analyze the effect of fabrication inaccuracies on the reflectance of a $\lambda/4$ anti-reflection coating and how it effects the formation of standing waves in the GaAs epilayer. Fabry-Perot oscillations in experimental transmission traces are used to quantify the reflectance at the GaAs-sapphire interface, showing a reduction in reflectance from 0.11 to less than 0.02. To further improve the homogeneity of laser intensity throughout the addressed ensemble of impurity spins, apertures are fabricated on top of the GaAs layer to shape the transverse laser intensity from a Gaussian profile into a top-hat profile with uniform intensity. We discuss three different fabrication methods and compare their results.

This chapter is based on reference 1 on page 133

5.1 Introduction

The measurements on D^0-D^0X ensembles in this thesis were performed on two types of samples. The first type, used in the experiments presented in chapter 3, consisted of a 10-μm thick GaAs epilayer, adhered to a sapphire substrate that was wedged to suppress Fabry-Perot (FP) effects. The layer was deposited on sapphire to facilitate transmission experiments. The fabrication of these samples is described extensively in reference [41]. The first type of samples showed substantial Fabry-Perot dispersion in the transmitted laser light due to FP effects in the GaAs layer, which acted as a weak optical cavity. The presence of standing waves makes it impossible to address an ensemble of optical defects with uniform laser intensity. To get rid of this effect, we fabricated a second type of sample, with anti-reflection coatings on the sapphire substrate (see also figure 4.2, coatings were ordered commercially [76]). Furthermore, on some samples gold films with apertures were fabricated, to shape laser fields with a Gaussian transverse intensity profile into top-hat profiles, further increasing the intensity uniformity in the ensemble.

Another problem associated with the uniform addressing of an ensemble of optical impurities arises due to lattice or strain inhomogeneity in the semiconductor host material. Optical dipole transitions experience a Stark shift of their resonance frequency in the presence of a non-zero electric field [77]. Hence, an inhomogeneous electric field throughout an ensemble of optical impurities causes broadening of the optical transitions. This reduces the interaction between the ensemble and a monochromatic light source, since the ensemble absorption is spread out over a range of frequencies. Also, more specifically, it deteriorates the precision of laser detuning from exact optical resonance, which compromises our two-laser feedback technique used in chapters 3 and 4. In cleanly grown insulating GaAs, strain is the main source of spatial electric-field modulations, because it deforms the crystal lattice and modifies the charge environment at the D^0-system. While advances in wafer growth have made it possible to obtain near-perfect mono-crystalline GaAs with negligible strain, subsequent fabrication steps and sample handling inevitably induce strain to a certain extent. The effect of strain on the donor-bound exciton system in GaAs was studied extensively by Karasyuk *et al.* [78].

This chapter describes how we deal with these material and laser-field non-uniformities in order to address an ensemble of donor-bound electrons as uniformly as possible. We describe the design and fabrication of GaAs epilayers on sapphire with an anti-reflection coating at their interface, shown schematically in figure 5.1. We explain the microscopy and spectroscopy techniques used to find strain-free regions in our samples and to quantify Fabry-Perot effects at the position of our laser spot. Lastly, we discuss three methods to fabricate apertures on top of the GaAs layers and show results of these methods. The technique of epitaxial lift-off [79, 80], used for the transfer of a 10-μm thick GaAs layer from its substrate to a piece of sapphire, is described in detail in appendix B.

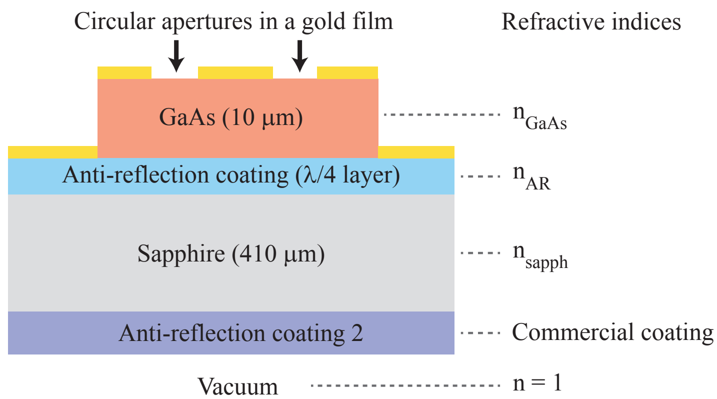

Figure 5.1: Schematic representation of a GaAs epilayer deposited on a sapphire substrate. The sapphire has anti-reflection coatings on both sides to prevent the formation of standing-wave modes inside the GaAs layer and the sapphire, for laser light incident from the top (see also figure 4.2). A gold film with circular apertures is fabricated on top of the GaAs layer.

5.2 Anti-reflection coatings on sapphire substrate

For the sapphire substrates with AR-coating, 410-μm thick sapphire wafers with c-plane [0001] orientation were used. The sapphire was epi-polished on both sides, to ensure optical flatness. A sapphire-to-air anti-reflection coating was deposited on the back side of the sapphire, to prevent standing waves in the sapphire. The reflectance of the sapphire-air interface was measured by the coating manufacturer to be less than 0.2 % for wavelengths of 780-840 nm at room temperature. Hence, we neglect the formation of standing waves in the sapphire and we will focus on the AR-coating at the GaAs-sapphire interface. Figure 5.1 indicates the refractive indices of the layers involved. A single $\lambda/4$-layer is used for the anti-reflection coating, with ideal refractive index $n_{AR} = \sqrt{n_{GaAs} n_{sapph}}$ and thickness $d = \lambda/4n_{AR}$ [81]. Such an ideal interface has exactly zero reflectance for incoming light with wavelength λ in vacuum and low reflectance for a wavelength window of tens of nanometers around λ. For our purposes $\lambda = 817$ nm, since the principal optical transitions of D^0X lie around this wavelength for magnetic fields between 0-10 T.

For the refractive index of GaAs and sapphire at a temperature of 4.2 K, we find literature values of $n_{GaAs} \approx 3.54$ [82, 83] and $n_{sapph} \approx 1.76$ [84]. Both values have an uncertainty smaller than 1%. Additional uncertainty arises since in practice the fabricated AR-coating will deviate slightly from the ideal design in its thickness and refractive index. We simulate the effect of these uncertainties and fabrication errors in the $\lambda/4$-layer on its reflectance. Figure 5.2 shows numerical simulations on the reflectance of the GaAs-sapphire interface. The displayed value is the average reflectance for wavelengths between 807-827 nm. Each red error bar shows the average and standard deviation of 10^4 calculations, where n_{GaAs}, n_{AR}, n_{sapph} and thickness d each have a random deviation from their ideal value, ranging between $-\varepsilon$ and ε. The blue line shows the worst case of 10^4 simulations for each value of ε.

Simulations on blue-detuned two-laser DNP feedback on donor-bound electrons in chapter 4 showed that in order to successfully drive all Overhauser shifts towards a narrow distribution around zero nuclear spin polarization, the two laser intensities should not differ more than $\approx 10\%$ throughout the GaAs layer (see for example figure 4.5b). In the notation of figure 4.3, this requires that $I_{max}/I_{min} \leq 1.1$ and that the reflectance of the interface should be lower than approximately 0.05% (to retrieve this value, a zoomed-in version of figure 4.3b was used). As visible in figure 5.2, this requirement is satisfied for fabrication errors with $\varepsilon < 1\%$. As discussed above, the refractive index for GaAs and sapphire is known with enough precision. The thickness of the AR-coating has to be controlled with nanometer accuracy and its refractive index should be 2.50 ± 0.025. While these accuracies are achievable, the room for error is small and the coating behavior has to be checked. We show later in this chapter how the amplitude of Fabry-Perot oscillations in the transmission signal is used to quantify the reflectance at the GaAs-sapphire interface.

5.3 Characterization of GaAs epilayers using DIC microscopy

GaAs layers were deposited by epitaxial lift-off (ELO) on the AR-coated sapphire, where they adhere by van der Waals bonding. During the wet-chemical ELO process, the surfaces of the (coated) sapphire and the GaAs layers that

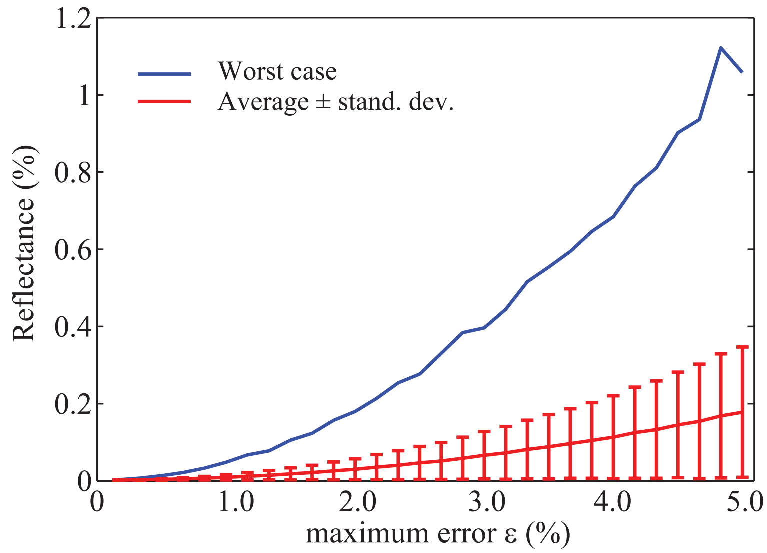

Figure 5.2: Simulations on the effect of fabrication errors in the AR-coating on the reflectance of the GaAs-sapphire interface. Random deviations from the ideal coating are included for the refractive indices n_{AR}, n_{GaAs} and n_{sapph} and the thickness d of the coating, with a magnitude ranging between $-\varepsilon$ and ε. The red line shows the average value of 10^4 simulations for each datapoint, with the error bars depicting the standard deviation. The blue line shows the worst case for each value of ε. The calculated reflectance is the average value for wavelenghts between 807-827 nm.

bond together are exposed and particles can contaminate the interface, preventing strain-free adhesion. Furthermore, the transfer of the 10-μm GaAs layer to sapphire is done manually, and residual strain can be present in the GaAs layer after deposition. While single-laser transmission spectroscopy at 4.2 K can resolve strain variation in the sample, cooling down samples to cryogenic temperatures and finding a reasonable micron-sized spot on a millimeter-sized sample is tedious work. Therefore, a simple and fast method is necessary to perform preliminary checks on the quality of the sample and determine which parts of the sample look strain-free. As we show below here, optical microscopy in both normal mode and differential interference contrast mode can provide sufficient preliminary information on sample quality, prior to more detailed spectroscopy.

Various microscope techniques have been developed to use the phase of light to extract information about height differences in the propagation direction, so called *phase contrast* techniques. One of these techniques is *differential interference contrast* (DIC) microscopy, where height gradients on the studied sample are converted into optical contrast [85]. DIC microscopy uses a birefringent prism to separate polarized light into two bundles that are focused on a sample with a small lateral offset. The spots reflect on the sample and are recombined at the same birefringent prism, where the two bundles interfere. If the sample surface has a height gradient in the direction of the bundle offset, the two bundles experience a difference in optical path length and will interfere with a phase difference. The DIC image that is observed through the microscope looks three-dimensional, with shadow-like features as if the sample is illuminated under an angle in the direction of the bundle offset. For a complete analysis of the height gradients on a sample, two DIC image have to be combined with the bundle offset in two orthogonal directions on the sample. However, for our analysis a single DIC image suffices.

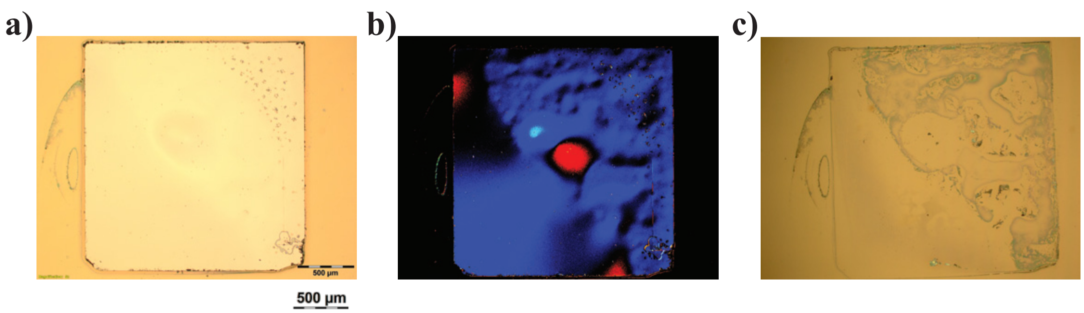

Figure 5.3: Images of ELO layers from an optical microscope. **a**, Bright-field image of a 2×2 mm GaAs layer deposited by epitaxial lift-off on a sapphire substrate. **b**, The same layer, imaged in differential interference contrast (DIC) mode. Changes in contrast are observed as color gradients. **c**, After the GaAs layer was removed by ultrasonication, a bright-field image shows clean sapphire at the regions that show up homogeneous in DIC imaging. Dirt between the sapphire and GaAs is revealed at the regions with strong color gradients.

Figure 5.3 correlates the contrast changes seen in DIC imaging with dirt at the GaAs-sapphire interface. Panel **a** shows a bright-field microscope image of a square piece of epitaxial GaAs deposited on sapphire. Some residual contamination is stuck on top of the GaAs after the wet-chemical ELO process (top-right of the square) and the center of the GaAs shows slight changes in color. In panel **b**, we use DIC imaging to obtain height information from the same GaAs layer. Two very distinct regions are revealed: The bottom-left part where the contrast is homogeneous and the top-right part where the contrast changes a lot with position. Subsequent attempts to remove the residual dirt on top of the GaAs by ultrasonication resulted in removal of the GaAs layer, uncovering the sapphire underneath. A bright-field image that was taken of the uncovered sapphire is shown in panel **c**, revealing the reason for the difference in contrast in the DIC image: The part that showed up as homogeneous in the DIC image shows clean sapphire, while the top-right region reveals a lot of dirt between the GaAs and the sapphire that led to the height gradients that showed up in the DIC image. Strain will most likely be inhomogeneous in such a region, as we verify in the following section.

5.4 2D spatial laser spectroscopy on GaAs epilayers

If microscope images at room temperature indicate that (part of) the GaAs layer has good adhesion to the sapphire and shows homogeneous regions, we insert the sample in a confocal microscope dipstick and cool it down to 4.2 K. In order to measure the strain inhomogeneity with much more detail and spatial resolution than the microscope images, we use a single frequency-scanning laser with micron spot-size at the GaAs layer to study the transmission spectrum. If the crystal lattice is strained, the GaAs band gap, and with it the free- and bound-exciton resonances (X and D^0X), shift towards lower energies [78]. Hence, the spectral position of these resonances in the laser transmission spectrum quantify the amount of strain in the laser spot. Furthermore, the linewidth of the free exciton absorption and the appearance of sharp D^0X transitions provide a good measure of strain *homogeneity* throughout the laser spot. A single-laser spectral transmission scan at zero magnetic field is shown in figure 5.4a, with the free- and bound-exciton absorptions labeled. The spectral position and the relatively narrow linewidth (compared to, for example, [86, 87]) of $X_{n=1}$ and the appearance of two (explained by Karasyuk *et al.* [88]) sharp D^0X absorptions indicate a low-strain region with little inhomogeneity.

It would take very long to map the amount of strain for the whole sample with laser frequency scans as described above. Instead, we pick three tell-tale laser frequencies, as depicted by the colored arrows in figure 5.4a. For each of these, we fix the laser at that frequency, scan the laser spot over the sample surface and record the transmission. The laser transmission at these wavelength is very sensitive to shifts and broadening of the free-exciton transitions, and hence to local strain. The results are shown in figure 5.4b-e. Figure 5.4b shows sample transmission for the laser frequency at the narrow transmission window in between the $X_{n=2}$ and $X_{n=3}$ exciton absorptions. High transmission indicates regions of low strain, because there the exciton lineshapes become narrower and

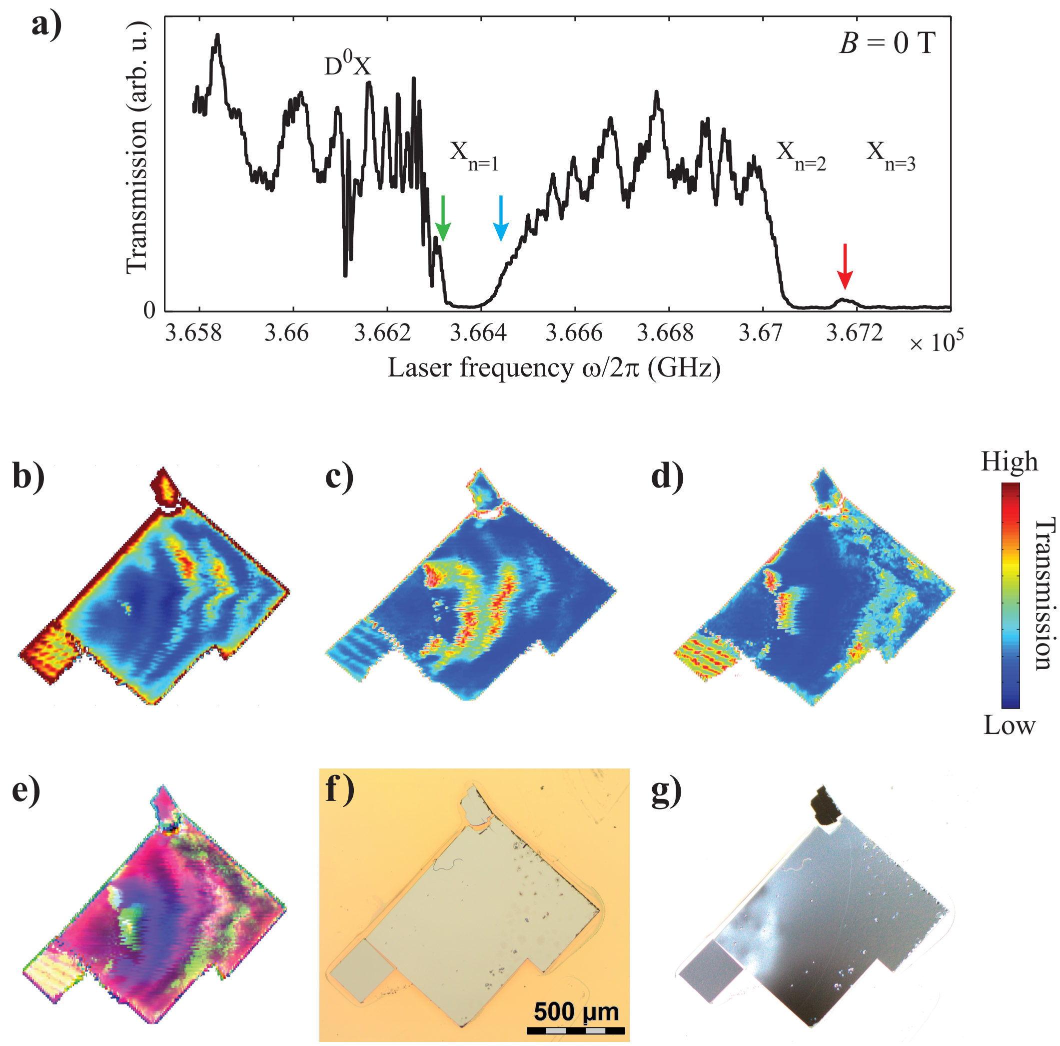

Figure 5.4: Spatial single-laser spectroscopy at $T = 4.2$ K (**b-e**) and microscope images at $T = 300$ K (**f-g**) of a 10-μm thick GaAs layer on sappire with anti-reflection coatings. **a**, Single-laser transmission frequency-scan for a micron-sized sample spot at $T = 4.2$ K. **b**, Spatial transmission scan, with a single laser fixed at the narrow transmission window between the strongly absorbing $n = 2$ and $n = 3$ free exciton lines (indicated by the red arrow in **a**), where n is the principal quantum number. **c** (**d**), Same as **b**, with the laser fixed at the high (low) frequency side of the $n = 1$ free exciton absorption (indicated by the blue (green) arrow in **a**). **e**, Graphical representation of the scans in **b**,**c** and **d** combined, using RGB channels (with data from **b** in the red, **c** in the blue and **d** in the green channel). **f**, Bright field microscope image. **g**, Difference interference contrast microscope image.

the laser absorption decreases.

Figure 5.4c and 5.4d show similar scans, for laser frequencies fixed at the high- and low-energy tail of $X_{n=1}$, respectively. Combined, these two scans distinguish between the amount of strain and the strain homogeneity: Regions that show high transmission in both scans signal a narrow exciton lineshape and hence homogeneous strain (for example, at the small bottom-left piece, as verified by the results in figure 5.4b). Regions with high transmission in figure 5.4c, but low transmission in figure 5.4c, indicate a shift of the exciton resonance towards lower energy, which is due to an increased amount of (possibly homogeneous) strain (for example, the middle of the big sample piece). In figure 5.4e, the results of the three spatial scans are combined in the red/green/blue (RGB) color channels of the figure. Regions with a color towards white are the most promising, since they show high transmission in all three scans. The small square of the bottom-left, that broke off from the main piece during fabrication, shows the lowest, most homogeneous strain. Also regions in the middle and right part of the main piece light up.

Figure 5.4f shows a microscope bright-field image at room temperature. The GaAs surface is contaminated by debris on the right side of the main piece. While a contaminated surface is not expected to enhance transmission, it seems that the contaminated part is correlated with the region of (seemingly) increased transmission as observed in figure 5.4d. We hypothesize that the debris scatters laser light, increasing the amount of light that is detected via reflections in the measurement volume. It is unclear why this does not show up in figure 5.4b and 5.4c. Figure 5.4g shows a DIC image, also at room temperature. Severe height gradients are visible at the left side of the main piece. This region indeed shows low transmission in all spatial scans. The border of this region lights up in figure 5.4e. A spectral scan (as in figure 5.4a) at this position showed no free-exciton resonance whatsoever, possibly because it was severely broadened or shifted out of range of the scanning laser. We conclude that the small bottom-left sample piece has the least amount of strain and should be further investigated for Fabry-Perot effects.

Note that we used micro-positioners [89] for the spatial scans to move the sample through the focus of a fixed laser beam. Since these positioners have a scan velocity that varies slightly over time and shows hysteresis with scan direction, the resulting images had to be post-processed to overlap with the actual sample geometry. Artifacts of this processing not being perfect are visible in the images as shaky edges of the sample and sample regions.

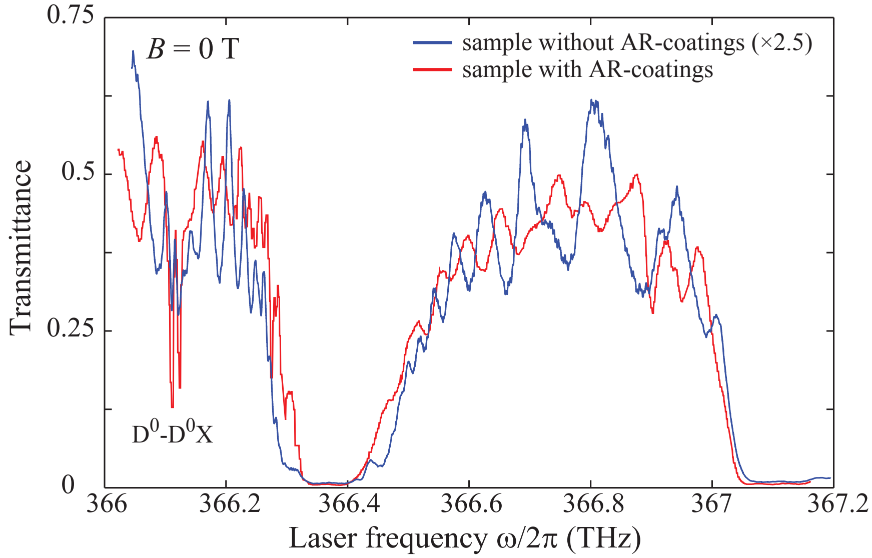

Figure 5.5: Fabry-Perot oscillations in the single-laser transmission signal for samples with (red line) and without anti-reflection coatings (blue line) at $B = 0$ T.

5.5 Single laser spectroscopy to quantify FP-effects

Figure 5.5 shows single-laser transmission scans at zero magnetic field, for a sample with (red line, measured on the small sample piece in figure 5.4) and without an anti-reflection coating at the GaAs-sapphire interface (blue line). Besides the strong free-exciton absorption and the two D^0X transitions at 366.1 THz, a Fabry-Perot modulation of the transmission signal with laser frequency is visible, due to self-interference of the laser light in the GaAs layer. The first thing to note is that the overall transmittance has increased more than twofold by the application of anti-reflection coatings. For convenience, we have multiplied the transmittance for the blue line with a factor 2.5, to compare the Fabry-Perot oscillations, which have a much smaller magnitude for the red line. Around the spectral lines of D^0X, the ratio between maximum and minimum transmittance of the FP-oscillation is reduced from almost 2 to less than 1.3. Figure 4.3b indicates that the reflectance of the GaAs-sapphire interface is thus reduced to a value smaller than 2 percent. Also, the visibility of the D^0X-transitions is much better and the absorption more pronounced when using an AR-coating. While the use of an anti-reflection coating looks promising, the value of I_{max}/I_{min} is not suppressed to below 1.1 as required to uniformly address the bound-electron ensemble. Characterization of more samples has to be performed to investigate whether better sample areas can be realized and observed.

5.6 Aperture fabrication on GaAs epilayers

While (ideal) AR-coatings can remove non-uniformity of the laser intensity in the propagation direction normal to the sample surface, it leaves the transverse intensity profile unaffected. The spatial divergence and wavefront of light beams are described by solutions of the Helmholtz equation, and have in general a non-uniform intensity profile at the wavefront in the far field. For our cryogenic experiments as described above, light from a single-mode optical fiber is focused by a confocal microscope on the sample surface. Hence, the spatial mode of the incident laser light on the sample surface is a TEM_{00} mode with a Gaussian transverse intensity profile. As described in chapter 4, this yields non-uniform driving of the spin-ensemble dynamics, which compromises our two-laser feedback control on the nuclear spin bath and decreases the transmittance of our lasers at CPT conditions. This is mainly due to the dominance of single-photon absorption over two-photon resonance in the outer regions of the Gaussian beam where the laser intensity is low.

We designed a mask with circular apertures on top of the GaAs layer, to shape the Gaussian transverse intensity profile into a top-hat profile (for the near field) with an approximate constant intensity, by blocking the outer regions. As mask material we chose gold, because it is softer than most opaque materials that can be evaporated. This will keep the amount of strain induced in the GaAs layer minimal. The optical absorption depth of gold gives $\approx 99\%$ absorption for a 70 nm film. Since the previous sections have shown that the uniformity of laser light inside the GaAs layer and the homogeneity of the optical transitions in the ensemble are strongly dependent on sample position, it would be beneficial to have control over the positions of apertures in the gold film. Table 5.1 lists the three different fabrication techniques we used to produce apertures, all with their own (dis)advantages. Their fabrication steps are described in detail in appendix B.

Table 5.1: Fabrication techniques for circular apertures in a gold film on GaAs.

Technique	**Position**	**Success**	**Edge roughness**
deposition (neg.-resist)	user-defined	no	N/A
deposition (microspheres)	random	yes	< 100 nm
wet-etching (pos.-resist)	user-defined	yes	$\sim$200 nm

The first technique uses a layer of negative-tone e-beam resist on top of the

GaAs layer. Circular regions of the resist are cross-linked by electron-beam lithography (EBL), and used as a deposition mask for the gold film. After the remaining resist is removed in a wet lift-off step, we should be left with a gold film with circular apertures. Since the patterning is done with EBL, we have a high level of control over the size and position of the apertures. However, this method did not successfully yield apertures, due to problems with the lift-off step.

The second technique also uses a deposition mask for the evaporation. Silicon nitrite microspheres with a diameter between 10-20 μm were deposited manually on top of the GaAs layer by pinching a tweezer covered in microspheres above the sample. The spheres adhere well to the surface by van der Waals forces. If necessary, the density of microspheres on the surface was reduced by an ultrasonication step. After the deposition of microspheres, a gold film was deposited via evaporation, while the spheres acted as a shadow mask. Subsequently, the microspheres were washed away in demineralized water. This yielded round apertures in the gold film. Figure 5.6a shows a scanning electron microscope (SEM) image of apertures realized with this technique. In the center of the image one microsphere is visible that did not wash away successfully. Some apertures are connected, which renders them useless for our optical purposes. However, isolated apertures are found over the sample surface. Figure 5.6b shows a detail of the side of an aperture. A gradual change in contrast in the radial direction indicates a transition region of $\sim$100 nm width where the gold film goes from zero to maximum thickness. The edge profile as seen from above looks smooth, its roughness is much smaller than 100 nm. The fabrication of apertures using microspheres is less invasive and cuts down the number of fabrication steps as compared to techniques using polymer resist masks, at the cost of less control over aperture size and position. An atomic force microscope can be used to move individual microspheres to desired positions, but this slows down the fabrication substantially.

The third fabrication technique uses a wet-etch step to etch circular openings in a gold film which is deposited directly onto the GaAs layer. Circular apertures are written into a positive-tone resist mask using EBL, after which a dilution of an iodine/potassium-iodide mixture is used to etch the gold away. After removal of the resist layer, a gold film with apertures is left. Figure 5.6c shows a SEM image of such an aperture. An advantage over fabrication using microspheres is that the position and size of the aperture are highly controllable. The edge profile of apertures fabricated with wet-etching, as shown in figure 5.6d, has a roughness with grains up to 200 nm. We hypothesize that an anisotropic etch speed along grain boundaries in the gold causes this edge roughness. For apertures with diameters larger than a few micrometers, we expect no substantial non-uniformity of the laser intensity in the near field.

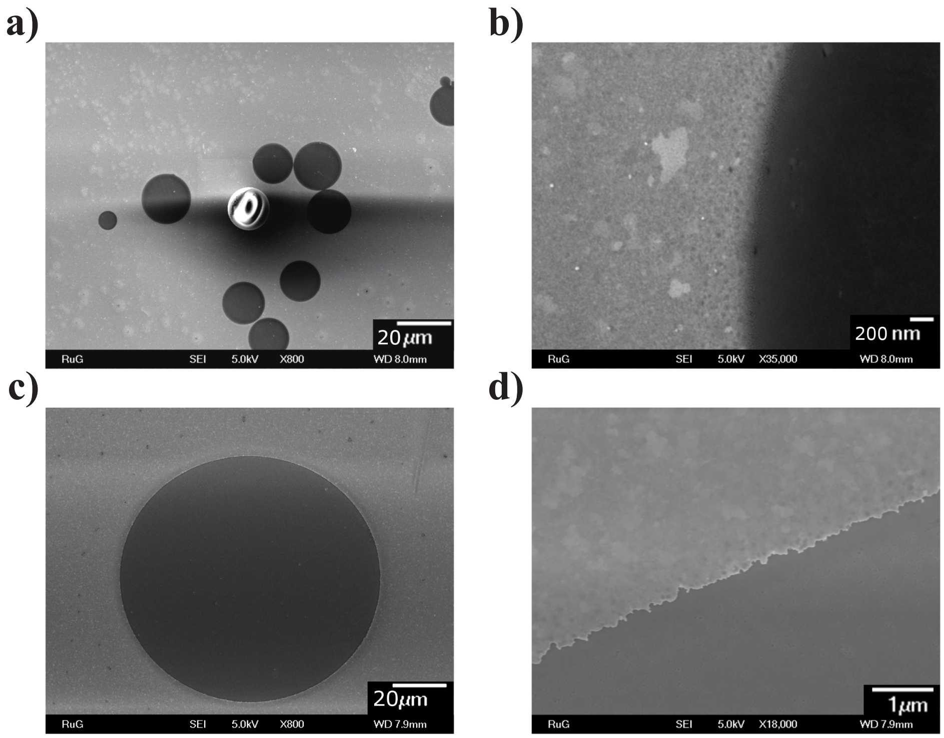

Figure 5.6: SEM images of a gold film with apertures on GaAs. **a**, Apertures created using silicon nitrite microspheres as a shadow mask for deposition of a gold film. **b**, Detail of an aperture in **a**. **c**, Aperture created using a wet etch step to remove part of a 30 nm gold film. **d**, Detail of the aperture in **c**.

5.7 Conclusion

Uniform light-matter interactions with an ensemble of quantum-systems rather than a single system poses a challenge in solid state environments, due to multiple inhomogeneities that render the light field and/or the environment of the quantum-systems spatially non-uniform. While nuclear-spin fluctuations are intrinsic to GaAs (and other non-zero nuclear-spin elements) and have to be suppressed by controlling their dynamics, inhomogeneous strain and modes of the light field in the sample are not and can therefore be removed by careful sample design. We have shown that the formation of standing waves can be suppressed with anti-reflection coatings and we quantified the vulnerability to fabrication error. We also provided two successful methods to fabricate apertures on GaAs epilayers, that serve different requirements. For the analysis of strain in the GaAs layer, DIC microscopy proofs to provide a quick qualitative method. Further quantitative information can be obtained with spatial laser scans that probe the broadening and shifts of the free-exciton absorption lines. While the presented results in this chapter were all obtained in GaAs, the conclusions are valid for all layered semiconductor materials that have one or more sharp spectral lines that shift due to strain.

Acknowledgments

The section on aperture fabrication in this chapter is based on work performed together with Maarten Degen, who worked on this for his master thesis research. We thank him for his persistence in trying different fabrication methods. We also thank Duc Van Nguyen of the Netherlands Institute for Space Research for diamond-sawing our sapphire wafers. Also thanks to Saurabh Roy, for teaching us how to work safely with acids. Many thanks to Sander Onur, for his help with epitaxial lift-off and his idea for the usage of microspheres for aperture fabrication. And lastly, thank to Mehdi Sedighi Ghozotkhar for letting us use his microspheres.

5.8 Supplementary information

After the analysis of the data as presented in this chapter, further measurements were performed on a new sample that yielded the best suppression of standing waves thus far. Figure 5.7 shows microscope images and single laser transmission scans for this sample. The same fabrication protocol was used as for the sample presented in figure 5.4, and a bright-field microscope image of the resulting 2×2 mm piece of epitaxial GaAs on anti-reflection coated sapphire is shown in figure 5.7a. In figure 5.7b, a DIC image of the sample clearly distinguishes flat regions with good adhesion of the epilayer to the sapphire (point A) and regions of bad adhesion where the GaAs epilayer is bulging (points B and C). Figure 5.7c shows single laser transmission scans at zero magnetic field for the three labeled spots in figure 5.7b.

The trace corresponding to position A shows a sharp $n = 1$ free-exciton absorption and the D^0X absorptions are visible, which indicates a homogeneous spot. Subsequent two-laser spectroscopy and CPT measurements (not shown

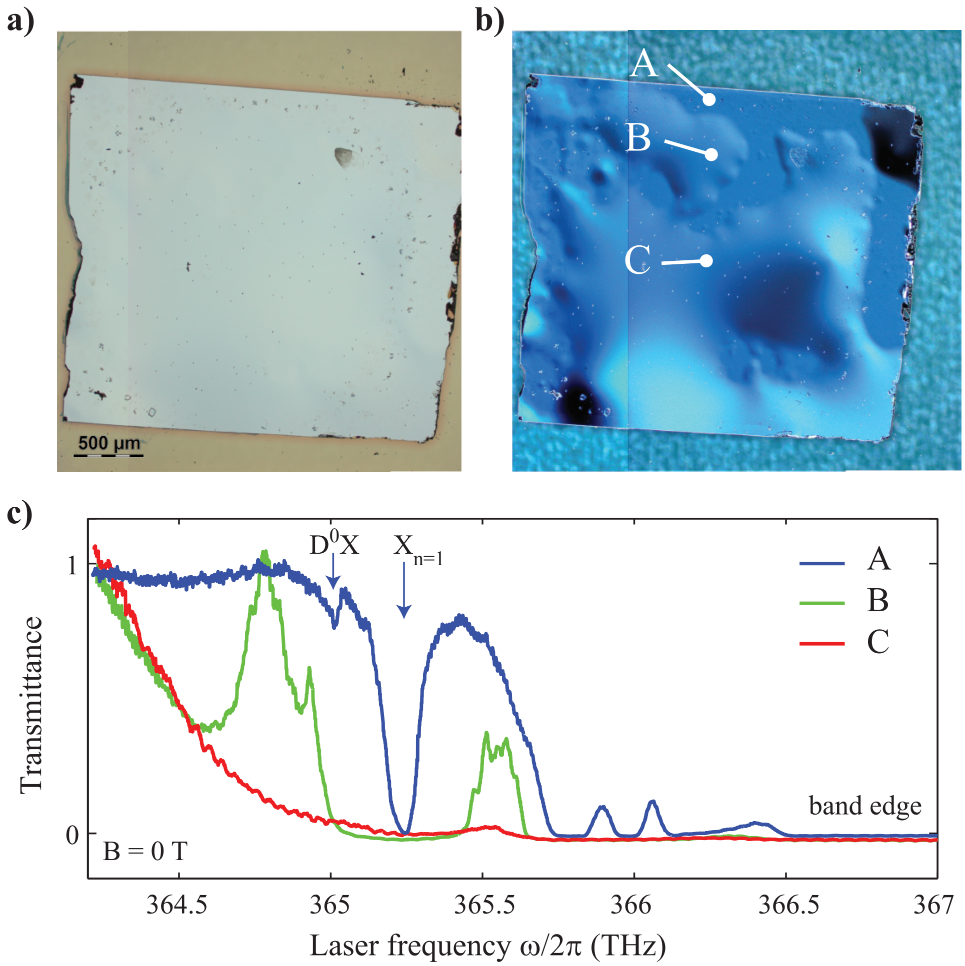

Figure 5.7: **a**, Bright-field microscope image of a 10-μm-thick GaAs epilayer on anti-reflection coated sapphire. **b**, Differential interference contract microscope image of the same sample. **c**, Single laser transmission scans, taken at the three points indicated in **b**.

here) confirmed the homogeneity of the ensemble within the laser spot. However, all spectral features are shifted to lower frequencies as compared to previous samples (compare with figure 5.5) by more than a terahertz, which suggests a high level of strain. The Fabry-Perot oscillations with frequency that were dominant in previous datasets are almost completely suppressed, affirming the good adhesion of the GaAs epilayer and the correct performance of the anti-reflection coating.

To put this spectrum of a homogeneous sample spot in contrast, we add two traces taken on sample positions B and C, where we expect a lot of inhomogeneity based on the DIC microscope image. The trace corresponding to B shows strongly broadened free-exciton lineshapes. Furthermore, since the GaAs epilayer does not adhere to the sapphire, the transmittance shows a severe Fabry-Perot oscillation. At sample spot C the inhomogeneity is even worse, and no recognizable features are observed.

Chapter 6

Analysis of optical differential transmission signals from co-propagating fields in a lambda system medium

Abstract

We analyze theoretically and experimentally how nonlinear differential transmission spectroscopy of a lambda system medium can provide quantitative understanding of the optical dipole moments and transition energies. We focus on the situation where two optical fields spatially overlap and co-propagate to a single detector. Nonlinear interactions give cross-modulation between a modulated and non-modulated laser field, yielding differential transmission signals. Our analysis shows how this approach can be used to enhance the visibility of relatively weak transitions, and how particular choices in the experimental design minimize systematic errors and the sensitivity to changes in laser field intensities. Experimentally, we demonstrate the relevance of our analysis with spectroscopy on the donor-bound exciton system of silicon donors in GaAs, where the transitions from the two bound-electron spin states to a bound-exciton state form a lambda system. Our approach is, however, of generic value for many spectroscopy experiments on solid-state systems in small cryogenic measurement volumes where *in-situ* frequency or polarization filtering of control and signal fields is often challenging.

This chapter is based on arXiv:1409.7679

6.1 Introduction

Laser spectroscopy is a main research tool to study electronic states of materials, across research fields ranging from atomic physics to cellular biology. In modern optics, nonlinear behavior of a medium is of primary interest, often studied with multiple laser fields which spatially overlap. In such cases, the presence of a strong control laser field makes it challenging to extract the signal from a weak probe field, in particular when further constraints enforce co-propagation of these fields. In practice one cannot always rely on spectral or polarization filtering (for example in cryogenic measurement volumes [17, 63, 90]) and in these cases low-frequency intensity modulation combined with lock-in detection techniques provides a means to separate a signal from co-propagating fields. Such modulation techniques, otherwise known as *optomodulation spectroscopy* [91], also improve the signal to noise ratio [92], as signals become less sensitive to external light and $1/f$ noise sources.

With this modulation technique applied to a nonlinear medium, the susceptibilities as seen by the control and probe fields become time dependent. This yields cross-modulation, where modulation of the incident intensity of one field influences the transmitted intensity of another field, giving rise to so-called differential transmission signals. Notably, for this paper the notion of differential transmission refers to this slow modulation of a susceptibility with continuous-wave lasers, effectively comparing two different steady-state conditions. The modulation timescale is orders of magnitude slower than the intrinsic electronic dynamics of the medium (that can be directly studied in pump-probe experiments with ultrafast pulsed lasers [93, 94, 95, 96], sometimes called *transient differential spectroscopy*).

Low-frequency intensity modulation has already been applied in a variety of optical experiments with differential signals from transmission, reflection or luminescence. Textbooks on nonlinear spectroscopy qualitatively discuss the benefits of studying crosstalk signals from modulation techniques in saturation spectroscopy [92, 97, 98]. Generically, the advantages lie in enhancing the visibility of weak transitions, and it was applied in experimental work on quantum wells [95], donor centers in semiconductors [17, 96], quantum dots [14, 91, 99, 100], and other atomic-like systems [101]. However, a detailed analysis of the differential signals is mostly not presented, despite the fact that this is essential for optimal design of these experiments, interpretation of the results, and insight into systematic errors that may occur.

We present here an analysis of the signals from differential transmission spectroscopy (DTS) on a medium with three-level lambda systems, based on both model calculations and experimental results. We show how DTS can dramatically enhance the spectroscopic visibility of weakly absorbing transitions, and how this enhancement depends on the involved optical dipole moments. We also investigate how the method can provide quantitative information about these dipole moments (which are key ingredients if one also wishes to unravel the combined DTS signal from two co-propagating fields into the separate transmission components). Further, our analysis shows how in two-laser experiments (where one laser is fixed and one is used for spectroscopic scanning) choosing which laser is modulated makes a key difference for being robust against unintentional intensity variations in the applied fields. Similarly, we show how the spectroscopic lines of a transition can show an apparent frequency shift. We show quantified results for this shift and describe the best approach for minimizing this systematic error.

Transition energies and lineshapes found with DTS can be qualitatively compared with results obtained with other methods [92, 98]: Photoluminescence excitation (PLE) yields very similar information as DTS, but can be challenging to implement since the PLE signal is emitted in all directions which makes collecting the signal with sufficient efficiency challenging. Also, sharp spectral filtering has to be applied to remove pump excitation light in order to see weak optical transitions. Time- and spectrally resolved photoluminescence (PL) can provide information on the dipole moments, while fitting single-laser absorption lines can also uncover the dipole moments (provided the absorption is strong enough and the concentration of optically-active centers in the sample is known). For weakly absorbing transitions, DTS is useful to enhance signals as compared to PLE and PL, and simultaneously it provides information on the dipole moments.

The relevance of our analysis is demonstrated with spectroscopy experiments on donor-bound exciton centers in Si-doped insulating gallium arsenide. While our experiments and part of our calculations thus focus on one particular material system and experimental arrangement, the analysis and methods that we present here are of generic value for spectroscopy experiments on media with multi-level systems, e.g. in the upcoming field of solotronics [102].

The paper is organized as follows. Section 6.2 presents simulations of DTS on a three-level lambda system medium. We introduce a model to calculate differential signals and describe it both at the macroscopic scale of the measurement setup and in terms of the microscopic electron dynamics. Subsequently, this model is used to analyze the benefits of differential transmission and how possible disadvantages can be minimized. Section 6.3 provides experimental results of DTS on silicon donor centers in gallium arsenide, demonstrating the effects described by our model.

6.2 Simulations

6.2.1 Model

We model a setup where two continuous-wave laser fields co-propagate through a medium, as shown in figure 6.1a. One field, depicted by its angular frequency ω_{mod}, is undergoing on-off modulation at frequency f_{mod} by a chopper. The other field, with angular frequency ω_{c}, is not modulated and hence has a constant intensity. A photodiode after the sample converts the total transmitted power into an electrical signal, and a lock-in amplifier isolates the signal component at frequency f_{mod}.

The modulation is orders of magnitude slower than the electronic dynamics in the medium and is assumed to have a square on-off envelop. This leads to two steady-state situations with transmittance $T^{\mathrm{on}}_{\omega_{\mathrm{mod}}}$ for the modulated field and transmittances $T^{\mathrm{on}}_{\omega_{\mathrm{c}}}$ and $T^{\mathrm{off}}_{\omega_{\mathrm{c}}}$ for the constant field. If the probed medium has nonlinear components in the susceptibility, *i.e.* the susceptibility depends on the presence of laser fields, $T^{\mathrm{on}}_{\omega_{\mathrm{c}}}$ and $T^{\mathrm{off}}_{\omega_{\mathrm{c}}}$ are in general not equal. Consequently, the transmittance of the constant field is time-dependent with frequency f_{mod} in the form of amplitude modulation of its transmission. This transfer of amplitude modulation from one field to another via the susceptibility will be called cross-modulation, and the contribution of the constant field to the transmission at frequency f_{mod} will be called differential transmission. The frequency component at f_{mod} of the total transmitted power thus consists of two parts and is given by

$$P_{f_{\mathrm{mod}}} = \underbrace{P_{\mathrm{mod}}\, T^{\mathrm{on}}_{\omega_{\mathrm{mod}}}}_{\text{normal transmission}} + \underbrace{P_{\mathrm{c}}(T^{\mathrm{on}}_{\omega_{\mathrm{c}}} - T^{\mathrm{off}}_{\omega_{\mathrm{c}}})}_{\text{differential transmission}} \tag{6.1}$$

where P_{mod} (P_{c}) is the power of the modulated (constant) field, and where P_{mod} and P_{c} are incident on the medium while $P_{f_{\mathrm{mod}}}$ is measured after the medium. We will focus on scenarios with $P_{\mathrm{mod}} < P_{\mathrm{c}}$ to ensure a prominent role for the differential transmission. Figure 6.1b illustrates the transmitted power for the individual fields and the total transmitted power, for qualitatively different levels of cross-modulation. If cross-modulation is absent, the contribution of differential transmission in Eq. (6.1) is zero, and the lock-in signal consists purely of

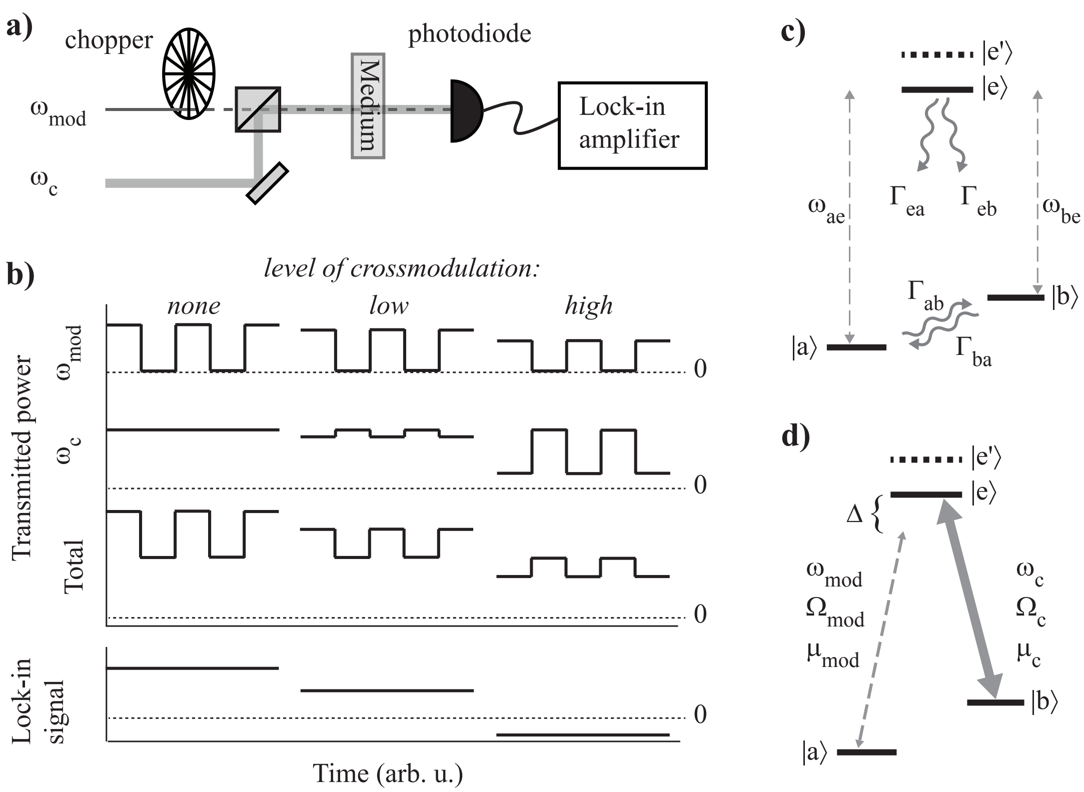

Figure 6.1: **a**, Experimental setup for differential transmission spectroscopy. Two overlapping laser fields, of which one is modulated by a chopper, co-propagate through the medium. Transmitted light is converted into an electrical signal by a photodiode. A lock-in amplifier filters out the signal component at the modulation frequency. **b**, Schematic illustration of the transmitted power of both laser fields, and the resulting lock-in signal. Signals are plotted for three levels of cross-modulation. **c**, Four-level Λ system with optical transitions from ground states $|a\rangle$ and $|b\rangle$ to excited states $|e\rangle$ and $|e'\rangle$. The transitions of $|a\rangle$ and $|b\rangle$ to $|e\rangle$ with energies $\hbar\omega_{ae}$ and $\hbar\omega_{be}$ are shown. Population relaxation rates Γ_{ij} are depicted by curly arrows. **d**, The modulated and constant laser, with frequency $\omega_{\rm mod}$ and $\omega_{\rm c}$ respectively, couple to the transitions with dipole moment $\mu_{\rm mod}$ and $\mu_{\rm c}$, resulting in Rabi frequencies $\Omega_{\rm mod}$ and $\Omega_{\rm c}$. One laser is coupled resonantly, while the other (in this figure the modulated laser) is scanned over resonance by changing the detuning Δ.

the normal transmission of the modulated field. For increasing levels of cross-modulation, the contribution of the differential transmission to the lock-in signal increases. When the differential transmission is larger than the normal transmission, and of opposite sign (which is the case for lambda systems), the total transmitted power shows a 180° phase shift. This shift manifests itself in the lock-in signal either as a negative signal or a 180° phase shift, depending on lock-in operation settings (for examples see figure 6.4 and figure 6.5c, respectively).

The medium of interest consists of lambda systems, as shown in figure 6.1c. Two ground states $|a\rangle$ and $|b\rangle$ have optical transitions to common excited states $|e\rangle$, $|e'\rangle$, *etc.* There is no optical transition between $|a\rangle$ and $|b\rangle$. Relaxation parameters Γ_{ij} describe both spontaneous emission rates from the excited states to the ground states and thermalization of population in the ground states. Furthermore, all states except $|a\rangle$ undergo pure dephasing γ_b, γ_e, *etc.* For the sake of simplicity, the simulations will be restricted to three-level lambda systems, without loss of validity. The experimental results in Sec. 6.3, however, show multiple excited states.

Differential transmission spectroscopy is modeled with two laser fields coupled to the optical transitions with transition dipole moments μ_{mod} and μ_{c}, see figure 6.1d. One field is held resonant with its transition frequency, while the other is scanned over the resonance by changing its detuning Δ. It is assumed that each laser couples only to one transition. The lasers drive transitions between the levels at Rabi frequencies Ω_{mod} and Ω_{c}. When two lasers drive a lambda system at high Rabi frequencies, effects related to coherent population trapping (CPT) appear as a narrow spectral feature around two-photon resonance within a single-photon absorption line [17, 38, 41]. In principle, our analysis is capable of taking these effects into account. However, in the present manuscript we show examples where the CPT feature is not visible, since it is not essential to the spectroscopic analysis we aim for.

The population in $|e\rangle$ spontaneously decays to both ground states, with relaxation rates Γ_{ea} and Γ_{eb}. Hence, a field present at transition ω_{ae} (ω_{be}) will effectively pump population to state $|b\rangle$ ($|a\rangle$), increasing the absorption coefficient for the field at transition ω_{be} (ω_{ae}). In Eq. (6.1) this results in the contribution $(T^{\text{on}}_{\omega_{\text{c}}} - T^{\text{off}}_{\omega_{\text{c}}})$, which is always negative for lambda systems. The amount of population pumped from one ground state of the lambda system to the other depends on the ratio of relaxation rates Γ_{ea} and Γ_{eb}. The relaxation rate of a transition is related to its electric dipole moment μ by

$$\Gamma = \frac{2n\omega^3\mu^2}{3\epsilon_0 h c^3} \tag{6.2}$$

where n is the bulk refractive index. The branching ratio Γ_{ea}/Γ_{eb} is given by

$$\frac{\Gamma_{ea}}{\Gamma_{eb}} = \frac{\omega_{ea}^3\mu_{\text{mod}}^2}{\omega_{eb}^3\mu_{\text{c}}^2} \approx \left(\frac{\mu_{\text{mod}}}{\mu_{\text{c}}}\right)^2, \quad \text{for } \omega_{ae} \approx \omega_{be} \tag{6.3}$$

The ratio $\mu_{\rm mod}/\mu_{\rm c}$, which we will call *relative dipole moment*, is the main parameter that determines the amount of cross-modulation and differential transmission (figure 6.2).

The transmittances are determined by the imaginary part of the susceptibility by

$$T(\omega) = \exp(-\frac{z\omega}{c}\mathrm{Im}[\chi(\omega)]) \tag{6.4}$$

where z is the sample thickness and c is the speed of light. For each field $\chi(\omega)$ is calculated by

$$\chi_i(\omega) = \frac{2N\mu_i^2\sigma_i(\omega)}{\epsilon_0\hbar\Omega}, \qquad i = 1,2 \tag{6.5}$$

where N is the number density of lambda systems in the material. The slowly oscillating part of the transition's coherence σ_i is obtained from the steady-state solution of the master equation for the density operator

$$\frac{d\hat{\rho}}{dt} = -\frac{i}{\hbar}[\hat{H},\hat{\rho}] + \hat{\mathcal{L}}(\hat{\rho}) \tag{6.6}$$

where $\hat{H}$ is the Hamiltonian of the laser-driven system in figure 6.1d (using a standard approach [38]). The Lindblad operator $\hat{\mathcal{L}}$ includes all relaxation and decoherence rates. We solve the master equation numerically, applying the rotating wave approximation [38].

6.2.2 Results

Table 6.1: Simulation parameters

$\Gamma_{ea}+\Gamma_{eb}$	1 GHz	Γ_{ba}	0.37 MHz
γ_e	5 GHz	z	10 μm
γ_b	5 GHz	N	10^{13} cm^{-3}

The simulations presented below were obtained with parameters that resemble our experimental system, see Table 6.1. However, our model yields qualitatively similar results for a large range of parameters.

Figure 6.2a shows DTS traces for three different values for the relative dipole moment. The absolute values of the dipole moments were varied in a manner that keeps the total relaxation rate $\Gamma_{ea}+\Gamma_{eb}$ from the excited state the same for the three cases. The solid lines present results of Eq. (6.1) normalized to

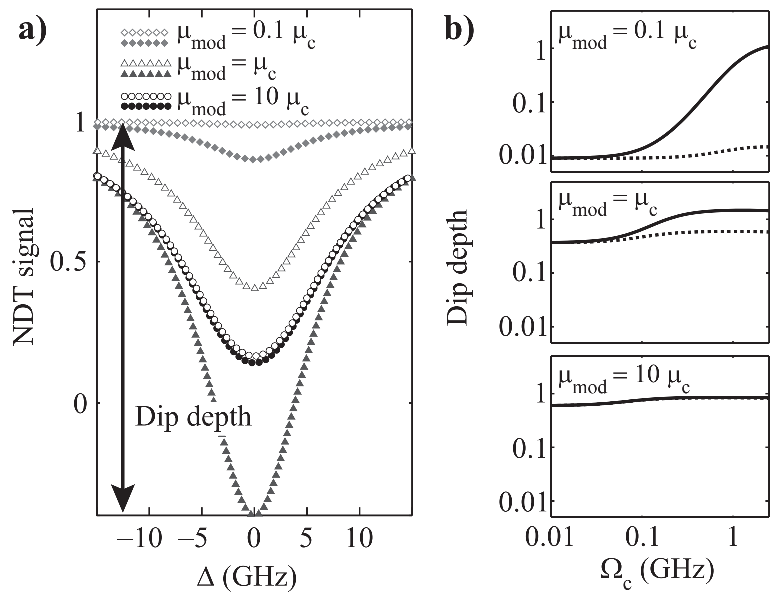

Figure 6.2: Simulation of normalized differential transmission (NDT) for three different relative dipole moments $\mu_{\mathrm{mod}}/\mu_{\mathrm{c}}$. **a**, NDT while scanning the modulated beam over the resonance, with $\Omega_{\mathrm{mod}} = 10$ MHz and $\Omega_{\mathrm{c}} = 0.5$ GHz. The traces show the total signal (solid symbols) as seen by the lock-in, which consists of normal transmission of the modulated field and differential transmission of the constant field due to cross-modulation. The open symbols show the contribution of the normal transmission. **b**, Enhanced transition visibility as a function of Rabi frequency of the constant laser, with $\Omega_{\mathrm{mod}} = 10$ MHz. The full lines show the dip depth of the total signal, while the dashed lines show only the normal transmission of the modulated field.

P_{mod}, and represent the total signal as seen by the lock-in. The dashed lines present (on the same scale) the normal transmission of the modulated laser, such that the difference with the solid lines signifies the magnitude of the differential transmission part. The Rabi frequencies are $\Omega_{\mathrm{mod}} = 10$ MHz for the modulated laser and $\Omega_{\mathrm{c}} = 0.5$ GHz for the constant laser, for all three cases. A normalized measure of the visibility of an optical transition in spectroscopy, which we will call *dip depth*, can be assigned to each scan as shown for the deepest scan. Figure 6.2b shows the dip depth as a function of Ω_{c}, again comparing the total lock-in signal with the normal transmission part.

The visibility of the transition is strongly enhanced by cross-modulation for lambda systems with a small relative dipole moment (shown for $\mu_{\mathrm{mod}}/\mu_{\mathrm{c}} = 0.1$ in the top panel of figure 6.2b). At high Ω_{c}, the differential transmission is two orders of magnitude larger than the normal transmission. For systems with a large relative dipole moment (bottom panel figure 6.2b), differential transmission is negligible, since the amount of cross-modulation is low. The absorption of the modulated laser is sufficient to have a good transition visibility at both low and high Ω_c. Here the presence of a strong non-modulated laser only slightly enhances the absorption of the modulated beam and hence the dip depth. In the intermediate case where $\mu_{mod}/\mu_c = 1$, the differential transmission approximately doubles the dip depth (middle panel figure 6.2b). For a range of μ_{mod}/μ_c values, strong cross-modulation can increase the dip depth to values greater than 1. This yields a negative DTS signal, as can be seen in figure 6.2a (solid trace for $\mu_{mod}/\mu_c = 1$) and in the top two panels of figure 6.2b at high Ω_c. Whether this occurs, depends on both the relative and absolute dipole moments. For smaller absolute dipole moments the results are very similar to figure 6.2, with smaller dip depths.

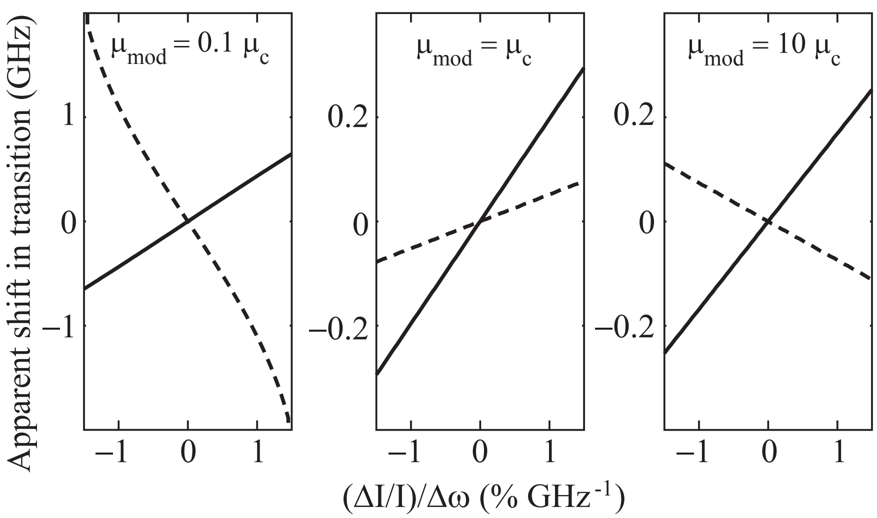

Figure 6.3: Apparent shift in the observed transition frequency due to intensity changes during spectroscopy scans for three different relative dipole moments (note different vertical scale for the left panel). The apparent shift is the difference between the lowest point in a spectroscopic dip and the real transition frequency. $(\Delta I/I)/\Delta\omega$ is the percentage change in laser intensity per GHz scan range. Full (dashed) lines show the apparent shift while scanning the constant (modulated) laser. Results for $\Omega_{mod} = 10$ MHz and $\Omega_c = 0.5$ GHz.

Optical transitions in spectroscopy are observed as peaks or dips against a background signal. When this background has a slope or even additional structure, it is harder to distinguish transitions. Moreover, this causes an offset for the lowest (highest) point of a dip (peak) that should identify the transition frequency. In addition, as we analyze below here, one can have apparent shifts in the transition frequency when the intensity of the scanning laser is not constant while scanning over the resonance. For this latter effect, the causes can be in the experimental setup (for example changes in laser power during frequency scans) or fundamental to the sample (for example due to Fabry-Perot cavity effects inside the sample, for an experimental example see figure 6.5a).

We modeled the effect of intensity changes on the observed transition frequency, comparing the apparent shift when scanning the modulated or the constant laser. We change the intensity of the scanning laser linearly with frequency. The unit of this intensity change is percentage per GHz scan range, with the intensity at the transition center defined as 100%. The lowest point in the DTS signal (in simulated traces, in appearance similar to the related experimental results in figure 6.5c) is taken to be the spectroscopic position of the scanned transition. Figure 6.3 shows the apparent shift as a function of linear power changes during scanning, for different relative dipole moments. Full (dashed) lines show the results for scanning the constant (modulated) laser. Errors in the transition frequency on the order of a GHz can be obtained for realistic changes in intensity over scan range. The error is largest for small relative dipole moments. However, this error can be suppressed a factor of three by scanning the constant laser. On the contrary, larger relative dipole moments show an enhanced spectroscopic error when the constant laser is scanned. Scanning the constant laser always results in a transition shift with the same sign as the intensity change (solid lines in the three panels). The sign of the error when scanning the modulated laser is less straightforward and depends on the competition between opposite shifts in the normal and differential transmission parts of Eq. (6.1).

To derive quantitative information on the relative and absolute strength of the optical transition dipole moments from such DTS data, a single DTS trace does not provide sufficient information. Instead, one needs to take data for a range of Ω_{mod} and Ω_{c} values, and fit the observed trends in dip depth to traces as in figure 6.2. If not known from independent measurements, the fitting should also yield parameters for the decay and dephasing parameters, and the optical Rabi frequencies. The nonlinear behavior of the overall system allows for such a multi-parameter fitting analysis. Notably, this approach is thus also needed if one wishes to unravel the combined DTS signal from two co-propagating fields into the separate transmission components.

6.3 Experiments on Si donors in i-GaAs

6.3.1 Material and methods

We used DTS as a spectroscopic technique to find the optical transitions in lambda systems provided by silicon donors in epitaxial insulating gallium arsenide. We studied epitaxially grown samples of 10 μm thickness and with a donor concentration of $\sim 3 \times 10^{13}$ cm^{-3}. The samples were studied at a temperature of 4.2 K and an applied magnetic field B of several Tesla. At such low donor concentration and temperature the donor centers are not ionized, thus providing an ensemble of localized electrons (so-called D^0 systems). These electrons have selectively-addressable optical transitions from the two Zeeman-split spin $S = \frac{1}{2}$ levels of the D^0 ground state to a donor-bound exciton complex (D^0X system). The D^0X system consists of two electrons and one hole bound at the donor side. This system has several energy levels in a frequency window of tens of GHz due to interactions between the particles, quantum confinement around the donor site and Zeeman shifts from the spin of the three particles [17, 88]. In our study the propagation of optical fields was in Voigt geometry. Two co-propagating laser fields with linear polarization were guided to the sample through a single mode fiber, and we had a detector directly behind the sample for recording DTS signals.

For applying the DTS technique and getting the results in figures 6.4 and 6.5, one laser was fixed at the optical transition in the spectrum from the D^0 spin-down state to the lowest level $|e\rangle$ of the D^0X complex (see figures 6.1c and 6.1d), while the other laser was scanned to probe the transitions from the D^0 spin-up state to the sequence of levels $|e\rangle$, $|e'\rangle$ *etc.* Strictly speaking, this two-laser driving only truly addressed a three-level lambda system when probing level $|e\rangle$. However, for the subsequent levels $|e'\rangle$, ... the two-laser approach counteracts optical pumping into one of the D^0 spin states, and for the investigation of how this yields cross-modulation signals it can for each transition be analyzed using our three-level modeling. For the examples presented here, the polarization of the fixed laser was parallel to the magnetic field, and that of the scanning laser either parallel or orthogonal [17].

6.3.2 Results

Figure 6.4 presents experimental DTS traces, taken with the constant laser fixed as described in the previous paragraph and the modulated laser scanning over the transition from the D^0 spin-up state to the third level in the D^0X complex.

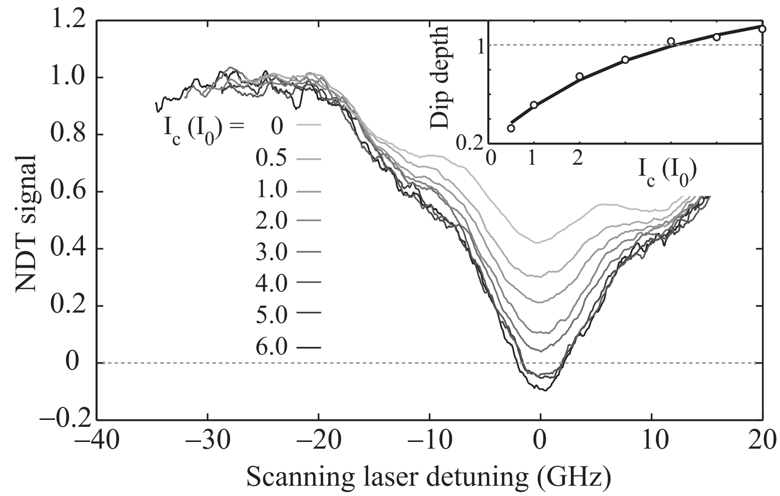

Figure 6.4: Normalized differential transmission (NDT) on a lambda system of the donor-bound exciton complex in GaAs:Si at $B = 3.94$ T. The constant laser is kept resonant, while the modulated laser is scanned over the other transitions of the lambda system. Increasing the intensity of the constant laser I_c enhances the transition visibility ($I_0 = 0.7$ mW cm^{-2}). For large I_c, the dip depth becomes greater than one. We fit the dip depth of the experimental traces with our model, using the dipole moments and laser spot size as fit parameters. The inset shows the experimentally found dip depths (circular symbols) and the resulting fit (full line), with $\mu_\mathrm{mod} = 1.38\ e \cdot \mathrm{nm}$ and $\mu_\mathrm{c} = 2.15\ e \cdot \mathrm{nm}$.

Resonance with this D^0–D^0X transition appears as a dip in transmission. The NDT signal is presented as a function of the detuning from resonance, and is normalized at the value at off-resonance detuning. Between traces, the intensity of the constant laser is increased. Since the spot size of the lasers was uncertain in this specific experiment, I_c is provided as a multiple of I_0 (with the value 0.7 mW cm^{-2}, found by fitting, see below). The transitions visibility increases with I_c, and the NDT signal drops below zero for the highest intensities. Strong variations in the laser intensity show as additional wiggles on the NDT signal. These variations are caused by a weak Fabry-Perot effect inside the sample, experienced by the scanning laser. To find the dip depth as a function of I_c, we subtract the background signal, as observed with the constant laser blocked ($I_c = 0$), from the other traces. For the present case this yields a good approximation for differential transmission contribution to the full DTS signal (see also discussion of figure 6.5 below). Comparing the dip depth of the traces to the analysis of figure 6.2 indicates a relative dipole moment $\mu_\mathrm{mod}/\mu_\mathrm{c} \lesssim 1$. This makes the differential transmission part the dominant term in Eq. 6.1 (see also figure 6.2b), justifying this approach. The absolute values of the dipole moments cannot be reliably extracted from a single trace of figure 6.4 since calculated traces with different parameters can be of similar shape. However, a fit that accounts for the full evolution of the dip depth as a function of I_c does yield a unique set of parameters, and we use this to find the absolute values of the dipole moments. The inset of figure 6.4 shows the resulting dip depths (circles) and a fit from our model (line, a trace similar to the solid lines in figure 6.2b). The corresponding fit parameters are $\mu_{\rm mod} = 1.38\ e \cdot {\rm nm}$, $\mu_{\rm c} = 2.15\ e \cdot {\rm nm}$ and $I_0 = 0.7\ {\rm mW\ cm^{-2}}$.

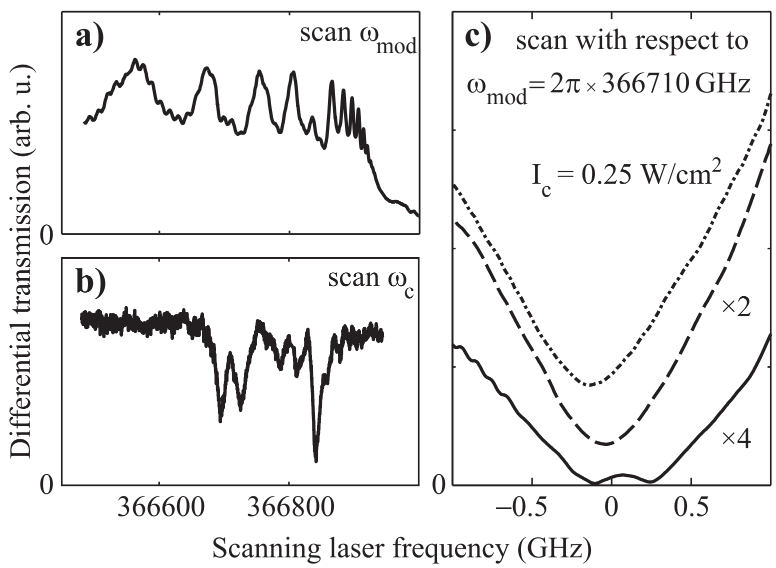

Figure 6.5: Experimental data of differential spectroscopy on donor-bound electrons in GaAs at $B = 6.41$ T, produced by scanning **a** the modulated laser or **b** the constant laser. In **a**, the spectroscopic features are imposed on a strongly varying background (in this specific case due to a weak Fabry-Perot interference in the sample). The approach used for **b**, is less influenced by Fabry-Perot interference. Here the various spectroscopic lines (corresponding to a set of donor-bound exciton states) appear on a flat background. **c**, Close-up of the spectroscopic line at $\approx$366710 GHz, for different constant laser intensities, obtained with the approach of **a**. Both the visibility and the apparent spectroscopic position of the transition are changing with laser intensity. The signal crosses zero for the highest intensity (here plotted as a positive signal for which it was noted that the lock-in signal had a 180 degree phase change).

The influence of intensity variations in the scanning laser on the DTS signal can be minimized by scanning the constant laser, as illustrated by comparing figure 6.5a and figure 6.5b. These panels show DTS scans, that differ by which laser was scanned. In figure 6.5a, the modulated laser is scanned. Its intensity undergoes significant variations due to the weak Fabry-Perot interference in the sample (which is chirped due to the very strong free-exciton absorption line at ~367000 GHz). Since the modulated laser is scanned, these variations contribute to the normal transmission, and when scanning near a resonance also to the differential transmission via cross-modulation. This severely deteriorates the visibility of the transitions. Conversely, in figure 6.5b the constant laser is scanned while the modulated laser is fixed at resonance. The constant laser scans over the same Fabry-Perot pattern as in figure 6.5a, but the resulting intensity variations do not contribute to the DTS signal when the scanning laser is off-resonance. Transitions now appear on a flat background. Notably, one can clearly recognize at least six D^0–D^0X resonance lines in the data. This technique hence provides clear high resolution spectroscopy data, not cluttered with the underlying Fabry-Perot pattern. To obtain a trace as in figure 6.5b from measured data as in figure 6.5a, one could investigate the approach where the varying background signal is subtracted (and this is used for figure 6.5c). This approach uses an additional scan where the constant laser is blocked. This yields the varying background, but also (and this is undesirable) reflects transitions that give absorption in single-lasers scans (that is, transitions that are visible despite the optical pumping by this single laser). Subtracting this trace from a trace as in figure 6.5a thus only yields an approximate form for the data as in figure 6.5b.

Figure 6.5c shows traces taken with the approach as for figure 6.5a, zooming in on one particular transition. The intensity of the constant laser is varied between traces. An apparent shift in the transition frequency of hundreds of MHz can be observed with increasing intensity. Additionally, the dip depth exceeds 1 at the highest value for I_c (here shown as a lock-in phase flip). We ran simulations for the apparent transition shift as in figure 6.3, obtaining a realistic value for $(\Delta I/I)/\Delta\omega$ from the Fabry-Perot pattern in figure 6.5a. The simulated shifts agreed with the experimental shift within a factor two.

6.4 Conclusion

We have analyzed how low-frequency amplitude modulation in two-laser spectroscopy yields differential signals for lock-in detection with a single photodiode. We applied this to DTS studies of a medium with lambda systems. Cross-modulation provides a very useful tool for enhancing the visibility of transitions that are otherwise difficult to observe. We quantified this enhancement and showed how the resulting spectroscopy provides information about the underlying dipole moments. Scanning the right laser can reduce signal disturbance from laser-field intensity changes, and minimize the spectroscopic error due to these effects. Experimental DTS results on GaAs:Si show the relevance and validity of our model. We envision that our modeling can be used for spectroscopy on a wider range of systems with multiple levels in the ground and excited state.

Appendix A

Standing waves in thin films and n(λ) around D^0X

A 10 μm thin film of GaAs on sapphire, as used for the experiments in this thesis, will show reflections at the vacuum-GaAs and GaAs-sapphire interface. In experiments where light is propagating in the direction normal to these interfaces, standing wave patterns occur in the GaAs film, due to the interference of forward and backward propagating waves. At the same time, this interference gives rise to fluctuations in the transmitted light after the film as a function of wavelength, known as Fabry-Perot oscillations [103]. The phase between the propagating and counter-propagating wave is determined by the ratio of the film thickness d and the laser wavelength in the film λ. The minimum and maximum intensity of the standing wave and their spatial positions within the film depend on the laser wavelength λ_0 and the refractive index n of the film, since these factors determine λ. In this appendix, we derive the equations that describe standing waves in and the Fabry-Perot oscillations behind a weak cavity. We then derive the probability distribution for laser intensity at an arbitrary position in the film. Finally, we use the derived equations to fit experimental traces of the absorption of the free exciton and Fabry-Perot oscillations around its wavelength. This yields the refractive index around the D^0X spectral lines.

A.1 Formation of standing waves in a thin film

We describe the case where a monochromatic wave with vacuum wavelength λ_0 propagates in the x-direction with angular frequency $\omega = \frac{2\pi c}{\lambda_0}$ and wavenumber $k = \frac{2\pi n}{\lambda_0}$, where n is the refractive index of the medium it propagates in:

$$\tilde{E}_0 = E_0 \; e^{i(kx-\omega t)}.$$

This wave is incident on a film with thickness L and refractive index n_{film}, where the propagation direction is normal to the film, as shown in figure A.1. The medium before (behind) the film has refractive index n_i (n_f). The wave reflects at the film's interfaces, resulting in a series of overlapping waves (shown with a vertical offset in the figure for clarity) that propagate alternating in the forward ($\tilde{E}_1$, $\tilde{E}_3$, ...) and backward direction ($\tilde{E}_2$, $\tilde{E}_4$, ...).

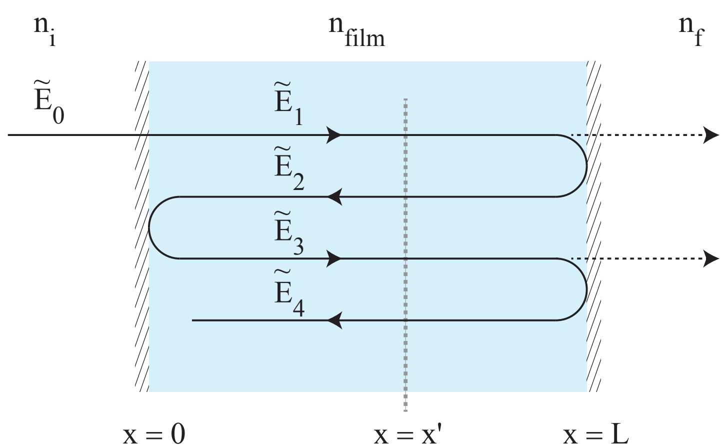

Figure A.1: Schematic picture of the reflections of a light wave inside a film of thickness L with reflective interfaces. Arrows depict the direction of propagation, which is normal to the film. The subsequent waves are displayed with a vertical offset for clarity, in reality they overlap. Upon incidence with an interface, part of the light is transmitted to the media surrounding the film, here shown for the interface with medium n_f (dashed arrows).

The reflection and transmission coefficients at the interfaces are given by Fresnel's equations:

$$
\begin{aligned}
r_i &= \frac{n_i - n_{film}}{n_i + n_{film}}, \\
r_f &= \frac{n_f - n_{film}}{n_f + n_{film}}, \\
t_i &= \sqrt{1 - r_i^2}, \\
t_f &= \sqrt{1 - r_f^2},
\end{aligned}
$$

where r_i and r_f are reflection coefficients for waves reaching the interfaces from the inside of the film. To calculate the total field at position x' in the film, we define the path-length δ from x' to the end of the film and back as $\delta = 2(L - x')$. The full-round trip Δ between the two interfaces is given by $\Delta = 2L$. An expression for the total field at $x = x'$ is given by the sum of all waves:

$$
\begin{array}{rcl}
\tilde{E}(x',t) & = & \tilde{E}_1(x',t) + \tilde{E}_2(x',t) + \tilde{E}_3(x',t) + ... + c.c. \\
& = & \begin{array}{lclcl} E_0 t_i e^{i(kx'-\omega t)} & + & E_0 t_i r_f e^{i(k[x'+\delta]-\omega t)} & + \\ E_0 t_i r_i r_f e^{i(k[x'+\Delta]-\omega t)} & + & E_0 t_i r_i r_f^2 e^{i(k[x'+\delta+\Delta]-\omega t)} & + \\ E_0 t_i r_i^2 r_f^2 e^{i(k[x'+2\Delta]-\omega t)} & + & E_0 t_i r_i^2 r_f^3 e^{i(k[x'+\delta+2\Delta]-\omega t)} & + ... + c.c. \end{array} \\
& = & E_0 t_i e^{i(kx'-\omega t)}(1 + r_f e^{ik\delta}) \sum_{n=0}^{\infty} r_i^n r_f^n e^{ikn\Delta} + c.c. \\
& = & E_0 t_i e^{i(kx'-\omega t)} \frac{(1+r_f e^{ik\delta})}{1-r_i r_f e^{ik\Delta}} + c.c.
\end{array}
$$

where for the last step we used the fact that:

$$\sum_{n=0}^{\infty} a^n = \frac{1}{1-a}, \qquad \text{for} \quad |a| < 1.$$

To calculate the intensity instead of the electric field, we use $I(x') \propto |\tilde{E}(x',t)|^2$ and we substitute I_0 for E_0^2:

$$I(x',k) = I_0 t_i^2 \frac{1 + 2r_f \cos(k\delta) + r_f^2}{1 - 2r_i r_f \cos(k\Delta) + r_i^2 r_f^2} \tag{A.1}$$

where I_0 is the intensity of the laser field before entering the film. To calculate the Fabry-Perot oscillations in transmission behind the film, we sum the transmitted forward propagating waves (dashed arrows in figure A.1):

$$E_{trans} = E_0 t_i t_f e^{i(kx'-\omega t)} \sum_{n=0}^{\infty} r_i^n r_f^n e^{ikn\Delta} + c.c.$$

leading to:

$$I_{trans}(k) = I_0 t_i^2 t_f^2 \frac{1}{1 - 2r_i r_f \cos(k\Delta) + r_i^2 r_f^2} \tag{A.2}$$

We observe that the I_{trans} is independent of position, which agrees with the fact that behind the film no spatial standing waves occur.

A.2 Distribution $P(I_1, I_2)$ in a GaAs film with standing waves

We now look at the probability distribution of the intensities of two lasers throughout the film. The intensity of a single laser field with fixed wavelength is given by equation A.1. For convenience, we rewrite it as a function of the average intensity $\bar{I}$ and the amplitude of the spatial intensity oscillation I_a:

$$\bar{I} \equiv I_0 t_i^2 \frac{1 + r_f^2}{1 - 2r_i r_f \cos(k\Delta) + r_i^2 r_f^2}, \tag{A.3}$$

and

$$I_a \equiv I_0 t_i^2 \frac{2r_f}{1 - 2r_i r_f \cos(k\Delta) + r_i^2 r_f^2}, \tag{A.4}$$

leading to:

$$I(x) = \bar{I} + I_a \ \cos(2\pi x/\lambda), \tag{A.5}$$

and the inverse function:

$$x(I) = \frac{\lambda}{2\pi} \cos^{-1}\left[\ \frac{I - \bar{I}}{I_a}\ \right] \tag{A.6}$$

Here, λ is the laser wavelength inside the cavity. We will now look at the probability density function for the intensity felt by an optical defect at an arbitrary position in the cavity. The intensity pattern is spatially periodic and we will look at the position interval in the cavity of $x \in [0, \lambda/2]$, since over this interval the intensity obtains all possible values. The probability density function for the position of an arbitrarily placed defect is given by:

$$P(x) = \frac{2}{\lambda}, \qquad \text{for } x \in [0, \lambda/2] \tag{A.7}$$

We can now derive the probability density function $P(I)$ for the laser intensity by [104]:

$$P(I) = P(x)\ \left|\frac{\partial x}{\partial I}\right| = \frac{1}{\pi I_a}\left[1 - \left(\frac{I - \bar{I}}{I_a}\right)^2\right]^{-\frac{1}{2}}, \tag{A.8}$$

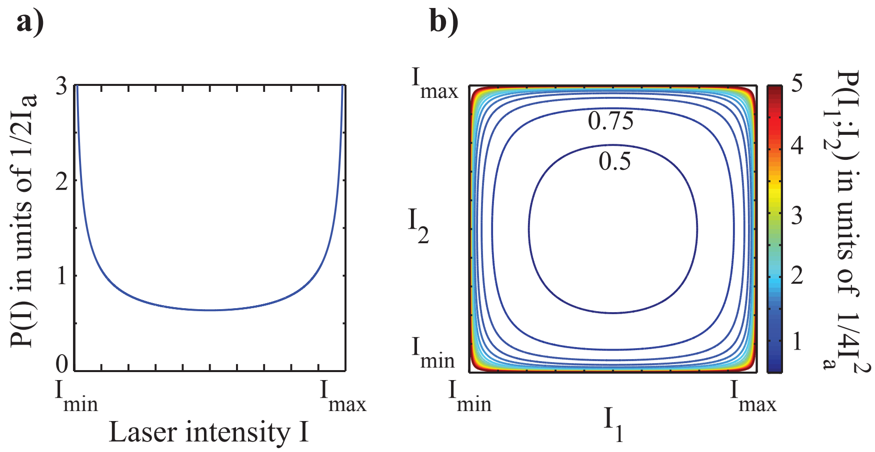

Figure A.2: **a**, Probability density function of the laser intensity at arbitrary position in a standing wave that varies sinusoidally between I_{min} and I_{max}. As expected for a sinus, the intensity is likely to lie around the extremes I_{min} or I_{max}. The function is normalized by $2I_a = I_{max} - I_{min}$. **b**, Contour plot of the probability density function of two laser intensities I_1 and I_2, for the case where $P(I_1)$ and $P(I_2)$ have no correlation, i.e. $P(I_1; I_2) = P(I_1) \times P(I_2)$. Contour lines are shown for multiples of 0.25.

which is plotted in figure A.2a. Here $I_{min} = \bar{I} - I_a$ and $I_{max} = \bar{I} + I_a$.

We now proceed with the combined probability density function $P(I_1; I_2)$, where I_1 and I_2 are the intensities of the field components at frequency ω_1 and ω_2 for two overlapping laser fields. Writing down $P(I_1; I_2)$ of finding a certain combination of I_1 and I_2 in overlapping intensity patterns of two lasers is in general not as simple as multiplying two density functions for a single laser, since $P(I_1)$ and $P(I_2)$ could be correlated. For example, if the two lasers have the same wavelength, their standing wave patterns overlap throughout the whole sample, thus being maximally correlated. However, the laser wavelengths λ_1 and λ_2 for the specific case of a 10-μm GaAs film described in chapter 4, have a separation that is approximately equal to the free spectral range of the GaAs cavity. In other words: the longest wavelength fits N times in the film and the shortest wavelength fits approximately $N + 1$ times. For $N \gg 1$, this means that the intensity patterns at an arbitrary position are equally likely to be in-phase as out-of-phase. In conclusion, we assume that the correlation between the patterns is roughly zero and we can write:

$$P(I_1, I_2) = P(I_1) \times P(I_2) = \frac{1}{\pi^2 I_a^2} \left[1 - \left(\frac{I_1 - \bar{I}}{I_a}\right)^2\right]^{-\frac{1}{2}} \left[1 - \left(\frac{I_2 - \bar{I}}{I_a}\right)^2\right]^{-\frac{1}{2}}, \tag{A.9}$$

which is plotted in figure A.2b.

A.3 Refractive index n around $\mathbf{D^0X}$

The main contribution to $n(\lambda)$ is the bulk refractive index of GaAs, which we will call n_0. The strong absorption of the free exciton $X_{n=1}$ modifies the refractive index, which causes n to be dispersive around the bound-exciton transitions of D^0X. In this section, we fit $n(\lambda)$ around the free exciton absorption, using experimental transmission traces. We fit the absorption line shape and the Fabry-Perot pattern simultaneously, for both zero and finite magnetic field. For simplicity, we assume n_0 constant and the effect of the D^0X absorption lines on $n(\lambda)$ negligible.

Both the absorption and dispersion are fit to the spectrum on the red side of the $X_{n=1}$-absorption, since at the blue side the situation is more complex due to the vicinity of higher energy X-features and the tail of the bandgap, which can be seen in figure A.3. The free exciton consists of six separate transitions, which are degenerate at zero magnetic field in the absence of strain. We therefore approximate the total free exciton susceptibility with a single Lorentzian oscillator. The susceptibility of a Lorentzian oscillator is given by:

$$\chi = \chi_0 \frac{(\nu_0 - \nu)\nu_0}{(\nu - \nu_0)^2 + \Delta\nu^2} \tag{A.10}$$

where χ_0 is the low frequency (electrostatic) susceptibility, ν_0 is the resonance frequency of the oscillator and $\Delta\nu$ is the spectral width of the absorption lineshape in linear frequency. From the susceptibility, we can calculate the refractive index $n(\nu)$:

$$n(\nu) = n_0 + n_X(\nu) = n_0 + \mathrm{Re}\left[\sqrt{1+\chi}\right] \tag{A.11}$$

Combining equation A.10 and A.11 with A.2 provides us with a function to fit Fabry-Perot oscillations in transmission. Figure A.3 shows a single laser scan at zero magnetic field and the best fit using the equations above.

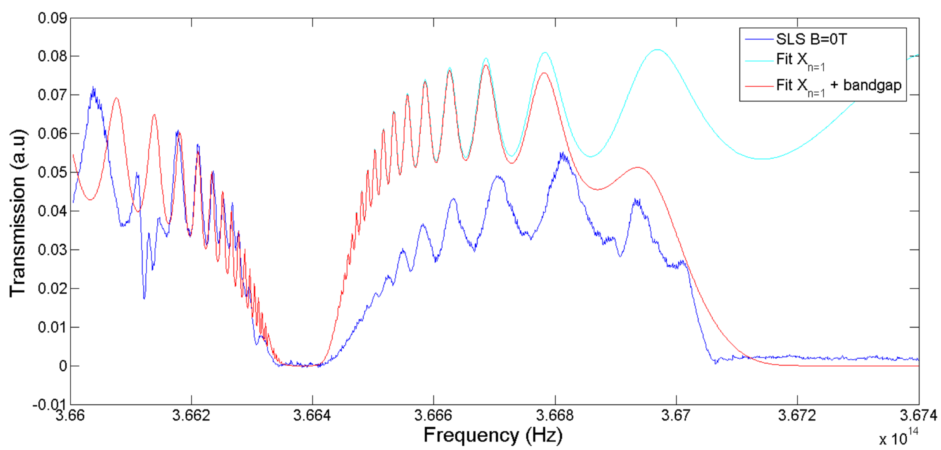

Figure A.3: Simultaneous fit of absorption and refraction.

Appendix B

Fabrication recipes

B.1 Cutting anti-reflection coated sapphire wafers

- Spin protective resist (side for GaAs-sapphire interface first):
  - Spin resist - 4000 rpm (1 min)
  - Bake-out in oven, 90 °C (4 min)
  - Repeat for other side
- Cutting:
  - Stick Sapphire to sticky polymer sheet with air-side
  - Diamond saw

B.2 Epitaxial Lift-Off of 10-μm thick GaAs epilayers

- Sapphire Preparation:
  - Clean in warm acetone (50 °C, 5 min)
  - Ultrasonic bath, setting 3 [105] (3 min)
  - Rinse in clean acetone in new beaker (30 s)
  - Rinse in IPA (30 s)
  - Spin dry
- Epitaxial lift-off (see figure B.1a):
  - Teflon pen in hydrofluoric acid 1% (24 h)
  - Rinse in DI water beaker 1 (3 min)

  - Rinse in DI water beaker 2 (3 min)
  - Rinse in DI water beaker 3 (3 min)

- Transfer to sapphire (see figure B.1b):
  - Submerge clean sapphire on teflon holder in beaker 3
  - Put teflon pen with ELO film on sapphire
  - Take out and remove excess water
  - Air dry (1 day)

- Cleaning:
  - Rinse in trichloroethylene (3 min)
  - Rinse in warm acetone (5 min)
  - Rinse in IPA (30 s)
  - Blow dry with nitrogen

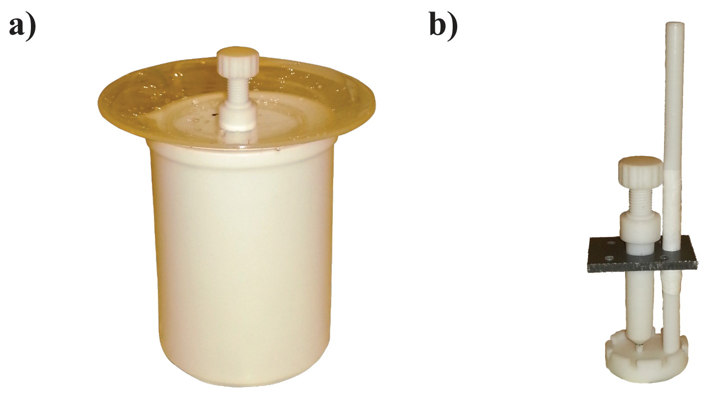

Figure B.1: **a**, Custom made tool for suspended submission of GaAs into hydrofluoric acid. The teflon pen is put through a hole in a polyethylene dish. **b**, Custom made tool for the drying step with the GaAs epilayer on Sapphire. Contact between sappire and the GaAs epilayer is made under water, to prevent dust particles at the interface of GaAs and sapphire.

B.3 Fabrication of gold films with apertures on GaAs epilayers

Positive-tone resist as a wet-etch mask

- Cleaning
  - Sonication in acetone, 35 °C, 10 min.
  - Rinse in IPA, 30 s
  - Blow dry with N_2 gun
- Gold deposition
  - Evaporation of gold, 5 nm, 1 Å/s
  - Evaporation of gold, 65 nm, 3 Å/s
- Spin coat resist
  - Pre-bake on hotplate, 180 °C, 90 s
  - Spin coat PMMA (0.27 μm), 4000 RPM, 60 s
  - Post-bake on hotplate, 180 °C, 90 s
- E-beam lithography
  - Beam voltage 30 kV
  - Aperture size 30 μm
  - Dose 450 μC cm^{-2}
- Development
  - Develop in IPA:MIBK (3:1), 60 s
  - Rinse in IPA, 30 s
  - Blow dry with N_2 gun
- Chemical wet-etch
  - etchant:H_2O (1:10), 120 s
  - gold etchant is KI/I_2, standard Sigma Aldrich
  - Rinse in DI water beaker 1, 60 s
  - Rinse in DI water beaker 2, 60 s

- Resist removal
  - Remove in acetone, room temperature, 60 s
  - Rinse in IPA, 30 s
  - Blow dry with N_2 gun

Recipe for apertures using SiN microspheres as shadow mask

- Cleaning
  - Sonication in acetone, 35 °C, 10 min.
  - Rinse in IPA, 30 s
  - Blow dry with N_2 gun
- Deposition of microspheres on GaAs 'stamp'
  - Put microsphere powder on tweezers
  - Pinch them above a piece of GaAs
  - Sonicate in dry beaker until coverage is optimal
- Transfer of microspheres to GaAs epilayer
  - Rotate GaAs stamp face down
  - Drop it on epilayer GaAs from a few mm height
- Gold deposition
  - Evaporation of gold, 5 nm, 1 Å/s
  - Evaporation of gold, 65 nm, 3 Å/s
- Removal of SiN microspheres
  - Rinse in DI water, 60 s
  - Blow dry with N_2 gun

References

[1] A. Einstein, B. Podolsky, and N. Rosen. Can quantum-mechanical description of physical reality be considered complete? *Physical Review*, 47:777–780, 1935.

[2] J. S. Bell. On the Einstein Podolsky Rosen paradox. *Physics*, 1:195–200, Aug 1964.

[3] D. Bohm and Y. Aharonov. Discussion of experimental proof for the paradox of Einstein, Rosen, and Podolsky. *Phys. Rev.*, 108:1070–1076, Nov 1957.

[4] Alain Aspect, Philippe Grangier, and Gérard Roger. Experimental tests of realistic local theories via Bell's theorem. *Phys. Rev. Lett.*, 47:460–463, Aug 1981.

[5] B. Hensen, H. Bernien, A. E. Dreau, A. Reiserer, N. Kalb, M. S. Blok, J. Ruitenberg, R. F. L. Vermeulen, R. N. Schouten, C. Abellan, W. Amaya, V. Pruneri, M. W. Mitchell, M. Markham, D. J. Twitchen, D. Elkouss, S. Wehner, T. H. Taminiau, and R. Hanson. Loophole-free bell inequality violation using electron spins separated by 1.3 kilometres. *Nature*, 526:682–686, 2015.

[6] Andrew Steane. Quantum computing. *Reports on Progress in Physics*, 61(2):117, 1998.

[7] W. Neuhauser, M. Hohenstatt, P. E. Toschek, and H. Dehmelt. Localized visible Ba^+ mono-ion oscillator. *Phys. Rev. A*, 22:1137–1140, Sep 1980.

[8] H. Kübler, J. P. Shaffer, T. Baluktsian, R. Löw, and T. Pfau. Coherent excitation of Rydberg atoms in micrometer-sized atomic vapour cells. *Nature Photonics*, 4:112–116, 2010.

[9] C. H. van der Wal, M. D. Eisaman, A. André, R. L. Walsworth, D. F. Phillips, A. S. Zibrov, and M. D. Lukin. Atomic memory for correlated photon states. *Science*, 301(5630):196–200, 2003.

[10] Jonas Bylander, Simon Gustavsson, Fei Yan, Fumiki Yoshihara, Khalil Harrabi, George Fitch, David G. Cory, Yasunobu Nakamura, Jaw-Shen

Tsai, and William D. Oliver. Noise spectroscopy through dynamical decoupling with a superconducting flux qubit. *Nature Physics*, 7:565//570, 2011.

[11] Daniel Loss and David P. DiVincenzo. Quantum computation with quantum dots. *Phys. Rev. A*, 57:120–126, Jan 1998.

[12] J. R. Petta, A. C. Johnson, J. M. Taylor, E. A. Laird, A. Yacoby, M. D. Lukin, C. M. Marcus, M. P. Hanson, and A. C. Gossard. Coherent manipulation of coupled electron spins in semiconductor quantum dots. *Science*, 309(5744):2180–2184, 2005.

[13] Clemens Matthiesen, Anthony Nickolas Vamivakas, and Mete Atatüre. Subnatural linewidth single photons from a quantum dot. *Phys. Rev. Lett.*, 108:093602, Feb 2012.

[14] R. J. Warburton, C. Schaflein, D. Haft, F. Bickel, A. Lorke, K. Karrai, J. M. Garcia, W. Schoenfeld, and P. M. Petroff. Optical emission from a charge-tunable quantum ring. *Nature*, 405:926–929, 2000.

[15] R. Hanson, F. M. Mendoza, R. J. Epstein, and D. D. Awschalom. Polarization and readout of coupled single spins in diamond. *Phys. Rev. Lett.*, 97:087601, Aug 2006.

[16] Olger V. Zwier, Danny OShea, Alexander R. Onur, and Caspar H. van der Wal. All-optical coherent population trapping with defect spin ensembles in silicon carbide. *Scientific Reports*, 5:10931, 2015.

[17] Maksym Sladkov, A. U. Chaubal, M. P. Bakker, A. R. Onur, D. Reuter, A. D. Wieck, and C. H. van der Wal. Electromagnetically induced transparency with an ensemble of donor-bound electron spins in a semiconductor. *Phys. Rev. B*, 82:121308, Sep 2010.

[18] Kai-Mei C. Fu, Charles Santori, Colin Stanley, M. C. Holland, and Yoshihisa Yamamoto. Coherent population trapping of electron spins in a high-purity n-type GaAs semiconductor. *Phys. Rev. Lett.*, 95:187405, Oct 2005.

[19] Michihisa Yamamoto, Shintaro Takada, Christopher Bauerle, Kenta Watanabe, Andreas D. Wieck, and Seigo Tarucha. Electrical control of a solid-state flying qubit. *Nature Nanotechnology*, 7:247–251, 2012.

[20] Ying-Dan Wang, A. Kemp, and K. Semba. Coupling superconducting flux qubits at optimal point via dynamic decoupling with the quantum bus. *Phys. Rev. B*, 79:024502, Jan 2009.

[21] F. R. Braakman, P. Barthelemy, C. Reichl, W. Wegscheider, and L. M. K. Vandersypen. Long-distance coherent coupling in a quantum dot array. *Nature Nanotechnology*, 8:432–437, 2013.

[22] P. Goy, J. M. Raimond, M. Gross, and S. Haroche. Observation of cavity-enhanced single-atom spontaneous emission. *Phys. Rev. Lett.*, 50:1903–1906, Jun 1983.

[23] D. M. Meekhof, C. Monroe, B. E. King, W. M. Itano, and D. J. Wineland. Generation of nonclassical motional states of a trapped atom. *Phys. Rev. Lett.*, 76:1796–1799, Mar 1996.

[24] Y. Louyer, D. Meschede, and A. Rauschenbeutel. Tunable whispering-gallery-mode resonators for cavity quantum electrodynamics. *Phys. Rev. A*, 72:031801, Sep 2005.

[25] G. Rempe, R. Lalezari, R. J. Thompson, and H. J. Kimble. Measurement of ultralow losses in an optical interferometer. *Opt. Lett.*, 17(5):363–365, Mar 1992.

[26] K. M. Birnbaum, A. Boca, R. Miller, A. D. Boozer, T. E. Northup, and H. J. Kimble. Photon blockade in an optical cavity with one trapped atom. *Nature*, 436:87–90, 2005.

[27] Yoshihiro Akahane, Takashi Asano, Bong-Shik Song, and Susumu Noda. High-q photonic nanocavity in a two-dimensional photonic crystal. *Nature*, 425:944–947, 2003.

[28] David Press, Stephan Götzinger, Stephan Reitzenstein, Carolin Hofmann, Andreas Löffler, Martin Kamp, Alfred Forchel, and Yoshihisa Yamamoto. Photon antibunching from a single quantum-dot-microcavity system in the strong coupling regime. *Phys. Rev. Lett.*, 98:117402, Mar 2007.

[29] Morten P. Bakker, Ajit V. Barve, Thomas Ruytenberg, Wolfgang Löffler, Larry A. Coldren, Dirk Bouwmeester, and Martin P. van Exter. Polarization degenerate solid-state cavity quantum electrodynamics. *Phys. Rev. B*, 91:115319, Mar 2015.

[30] L.-M. Duan, M. D. Lukin, J. I. Cirac, and P. Zoller. Long-distance quantum communication with atomic ensembles and linear optics. *Nature*, 414:413–418, 2001.

[31] Marlan O. Scully, Edward S. Fry, C. H. Raymond Ooi, and Krzysztof Wódkiewicz. Directed spontaneous emission from an extended ensemble of n atoms: Timing is everything. *Phys. Rev. Lett.*, 96:010501, Jan 2006.

[32] M. O. Scully and A. A. Svidzinsky. The super of superradiance. *Science*, 325:1510–1511, 2009.

[33] A. G. Radnaev, Y. O. Dudin, R. Zhao, H. H. Jen, S. D. Jenkins, A. Kuzmich, and T. A. B. Kennedy. A quantum memory with telecom-wavelength conversion. *Nature Physics*, 6:894–899, 2003.

[34] D. N. Matsukevich, T. Chanelière, S. D. Jenkins, S.-Y. Lan, T. A. B. Kennedy, and A. Kuzmich. Entanglement of remote atomic qubits. *Phys. Rev. Lett.*, 96:030405, Jan 2006.

[35] J. J. Longdell, E. Fraval, M. J. Sellars, and N. B. Manson. Stopped light with storage times greater than one second using electromagnetically induced transparency in a solid. *Phys. Rev. Lett.*, 95:063601, Aug 2005.

[36] Marko Lovrić, Dieter Suter, Alban Ferrier, and Philippe Goldner. Faithful solid state optical memory with dynamically decoupled spin wave storage. *Phys. Rev. Lett.*, 111:020503, Jul 2013.

[37] Pierre Jobez, Cyril Laplane, Nuala Timoney, Nicolas Gisin, Alban Ferrier, Philippe Goldner, and Mikael Afzelius. Coherent spin control at the quantum level in an ensemble-based optical memory. *Phys. Rev. Lett.*, 114:230502, Jun 2015.

[38] Michael Fleischhauer, Atac Imamoglu, and Jonathan P. Marangos. Electromagnetically induced transparency: Optics in coherent media. *Rev. Mod. Phys.*, 77:633–673, Jul 2005.

[39] Xiaodong Xu, Wang Yao, Bo Sun, Duncan G. Steel, Allan S. Bracker, Daniel Gammon, and L. J. Sham. Optically controlled locking of the nuclear field via coherent dark-state spectroscopy. *Nature*, 459(7250):1105–1109, June 2009.

[40] Bo Sun, Colin Ming Earn Chow, Duncan G. Steel, Allan S. Bracker, Daniel Gammon, and L. J. Sham. Persistent narrowing of nuclear-spin fluctuations in inas quantum dots using laser excitation. *Phys. Rev. Lett.*, 108:187401, May 2012.

[41] Alexander R. Onur. *Optical control of mesoscopic spin ensembles in gallium arsenide*. PhD thesis, Rijksuniversiteit Groningen, 2015.

[42] Alexander R. Onur and Caspar H. van der Wal. Two-laser dynamic nuclear polarization with semiconductor electrons: feedback, suppressed fluctuations, and bistability near two-photon resonance. *arXiv:1409.7576* (2014), 2014.

[43] M. I. Dyakonov and V. I. Perel. Optical orientation in a system of electrons and lattice nuclei in semiconductors-theory. *Zh. Eksp. Teor. Fiz.*, 65:362–375, 1973.

[44] Alexander V. Khaetskii, Daniel Loss, and Leonid Glazman. Electron spin decoherence in quantum dots due to interaction with nuclei. *Phys. Rev. Lett.*, 88:186802, Apr 2002.

[45] I. A. Merkulov, Al. L. Efros, and M. Rosen. Electron spin relaxation by nuclei in semiconductor quantum dots. *Phys. Rev. B*, 65:205309, Apr 2002.

[46] W. A. Coish and Daniel Loss. Hyperfine interaction in a quantum dot: Non-Markovian electron spin dynamics. *Phys. Rev. B*, 70:195340, Nov 2004.

[47] Jeroen Danon and Yuli V. Nazarov. Nuclear tuning and detuning of the electron spin resonance in a quantum dot: Theoretical consideration. *Phys. Rev. Lett.*, 100:056603, Feb 2008.

[48] D. Klauser, W. A. Coish, and Daniel Loss. Nuclear spin state narrowing via gate-controlled rabi oscillations in a double quantum dot. *Phys. Rev. B*, 73:205302, May 2006.

[49] G. Giedke, J. M. Taylor, D. D'Alessandro, M. D. Lukin, and A. Imamoglu. Quantum measurement of a mesoscopic spin ensemble. *Phys. Rev. A*, 74:032316, Sep 2006.

[50] Dimitrije Stepanenko, Guido Burkard, Geza Giedke, and Atac Imamoglu. Enhancement of electron spin coherence by optical preparation of nuclear spins. *Phys. Rev. Lett.*, 96:136401, Apr 2006.

[51] M. Issler, E. M. Kessler, G. Giedke, S. Yelin, I. Cirac, M. D. Lukin, and A. Imamoglu. Nuclear spin cooling using Overhauser-field selective coherent population trapping. *Phys. Rev. Lett.*, 105:267202, Dec 2010.

[52] V. L. Korenev. Multiple stable states of a periodically driven electron spin in a quantum dot using circularly polarized light. *Phys. Rev. B*, 83:235429, Jun 2011.

[53] Xiao-Feng Shi. Nuclear spin polarization in a single quantum dot pumped by two laser beams. *Phys. Rev. B*, 87:195318, May 2013.

[54] D. J. Reilly, J. M. Taylor, J. R. Petta, C. M. Marcus, M. P. Hanson, and A. C. Gossard. Suppressing spin qubit dephasing by nuclear state preparation. *Science*, 321(5890):817–821, 2008.

[55] Ivo T. Vink, Katja C. Nowack, Frank H. L. Koppens, Jeroen Danon, Yuli V. Nazarov, and Lieven M. K. Vandersypen. Locking electron spins into magnetic resonance by electron-nuclear feedback. *Nature Physics*, 5(10):764–768, October 2009.

[56] C Latta, A Högele, Y Zhao, AN Vamivakas, P Maletinsky, M Kroner, J Dreiser, I Carusotto, A Badolato, D Schuh, et al. Confluence of resonant laser excitation and bidirectional quantum-dot nuclear-spin polarization. *Nature Physics*, 5(10):758–763, 2009.

[57] Hendrik Bluhm, Sandra Foletti, Diana Mahalu, Vladimir Umansky, and Amir Yacoby. Enhancing the coherence of a spin qubit by operating it as a feedback loop that controls its nuclear spin bath. *Phys. Rev. Lett.*, 105:216803, Nov 2010.

[58] Thaddeus D. Ladd, David Press, Kristiaan De Greve, Peter L. McMahon, Benedikt Friess, Christian Schneider, Martin Kamp, Sven Höfling, Alfred Forchel, and Yoshihisa Yamamoto. Pulsed nuclear pumping and spin diffusion in a single charged quantum dot. *Phys. Rev. Lett.*, 105:107401, Sep 2010.

[59] Jack Hansom, Carsten H. H. Schulte, Claire Le Gall, Clemens Matthiesen, Edmund Clarke, Maxime Hugues, Jacob M. Taylor, and Mete Atatüre. Environment-assisted quantum control of a solid-state spin via coherent dark states. *Nature Physics*, 10:725–730, 2014.

[60] E Togan, Y Chu, A Imamoglu, and MD Lukin. Laser cooling and real-time measurement of the nuclear spin environment of a solid-state qubit. *Nature*, 478(7370):497–501, 2011.

[61] A. Greilich, A. Shabaev, D. R. Yakovlev, Al. L. Efros, I. A. Yugova, D. Reuter, A. D. Wieck, and M. Bayer. Nuclei-induced frequency focusing of electron spin coherence. *Science*, 317(5846):1896–1899, 2007.

[62] S. G. Carter, A. Shabaev, Sophia E. Economou, T. A. Kennedy, A. S. Bracker, and T. L. Reinecke. Directing nuclear spin flips in InAs quantum dots using detuned optical pulse trains. *Phys. Rev. Lett.*, 102:167403, Apr 2009.

[63] Maksym Sladkov, M. P. Bakker, A. U. Chaubal, D. Reuter, A. D. Wieck, and C. H. van der Wal. Polarization-preserving confocal microscope for optical experiments in a dilution refrigerator with high magnetic field. *Review of Scientific Instruments*, 82(4):043105, 2011.

[64] Susan M. Clark, Kai-Mei C. Fu, Qiang Zhang, Thaddeus D. Ladd, Colin Stanley, and Yoshihisa Yamamoto. Ultrafast optical spin echo for electron spins in semiconductors. *Phys. Rev. Lett.*, 102:247601, Jun 2009.

[65] D. Paget, G. Lampel, B. Sapoval, and V. I. Safarov. Low field electron-nuclear spin coupling in gallium arsenide under optical pumping conditions. *Phys. Rev. B*, 15:5780–5796, Jun 1977.

[66] A. Abragam. *The principles of nuclear magnetism.* Oxford University Press, 1961.

[67] C. H. Townes, Conyers Herring, and W. D. Knight. The effect of electronic paramagnetism on nuclear magnetic resonance frequencies in metals. *Phys. Rev.*, 77:852–853, Mar 1950.

[68] Daniel Paget. Optical detection of NMR in high-purity GaAs: Direct study of the relaxation of nuclei close to shallow donors. *Phys. Rev. B*, 25:4444–4451, Apr 1982.

[69] Changxue Deng and Xuedong Hu. Nuclear spin diffusion in quantum dots: Effects of inhomogeneous hyperfine interaction. *Phys. Rev. B*, 72:165333, Oct 2005.

[70] Zhe-Xuan Gong, Zhang-Qi Yin, and L-M Duan. Dynamics of the Overhauser field under nuclear spin diffusion in a quantum dot. *New Journal of Physics*, 13(3):033036, 2011.

[71] Jonathan Baugh, Yosuke Kitamura, Keiji Ono, and Seigo Tarucha. Large nuclear Overhauser fields detected in vertically coupled double quantum dots. *Phys. Rev. Lett.*, 99:096804, Aug 2007.

[72] D. J. Reilly, J. M. Taylor, J. R. Petta, C. M. Marcus, M. P. Hanson, and A. C. Gossard. Exchange control of nuclear spin diffusion in a double quantum dot. *Phys. Rev. Lett.*, 104:236802, Jun 2010.

[73] A. Greilich, A. Pawlis, F. Liu, O. A. Yugov, D. R. Yakovlev, K. Lischka, Y. Yamamoto, and M. Bayer. Spin dephasing of fluorine-bound electrons in ZnSe. *Phys. Rev. B*, 85:121303, Mar 2012.

[74] Y.M. Kim, D. Sleiter, K. Sanaka, D. Reuter, K. Lischka, Y. Yamamoto, and A. Pawlis. Optically controlled initialization and read-out of an electron spin bound to a fluorine donor in ZnSe. *Current Applied Physics*, 14(9):1234–1239, 2014.

[75] Bernhard Urbaszek, Xavier Marie, Thierry Amand, Olivier Krebs, Paul Voisin, Patrick Maletinsky, Alexander Högele, and Atac Imamoglu. Nuclear spin physics in quantum dots: An optical investigation. *Rev. Mod. Phys.*, 85:79–133, Jan 2013.

[76] Evaporated Coating Inc., http://www.evaporatedcoatings.com/.

[77] J. Stark. Beobachtungen ber den effekt des elektrischen feldes auf spektrallinien. i. quereffekt. *Annalen der Physik*, 348(7):965–982, 1914.

[78] V.A. Karasyuk, M.L.W. Thewalt, and A.J. SpringThorpe. Strain effects on bound exciton luminescence in epitaxial GaAs studied using a wafer bending technique. *physica status solidi (b)*, 210(2):353–359, 1998.

[79] Eli Yablonovitch, T Gmitter, JP Harbison, and R Bhat. Extreme selectivity in the lift-off of epitaxial GaAs films. *Applied Physics Letters*, 51(26):2222–2224, 1987.

[80] Piet Demeester, Ivan Pollentier, Peter De Dobbelaere, Catherine Brys, and Peter Van Daele. Epitaxial lift-off and its applications. *Semiconductor science and technology*, 8(6):1124, 1993.

[81] Bahaa EA Saleh and Malvin Carl Teich. *Fundamentals of photonics*. Wiley New York, 2007.

[82] Lukas Greuter, Daniel Najer, Andreas V. Kuhlmann, Sascha R. Valentin, Arne Ludwig, Andreas D. Wieck, Sebastian Starosielec, and Richard J. Warburton. Epitaxial lift-off for solid-state cavity quantum electrodynamics. *Journal of Applied Physics*, 118(7), 2015.

[83] P. Lautenschlager, M. Garriga, S. Logothetidis, and M. Cardona. Interband critical points of GaAs and their temperature dependence. *Phys. Rev. B*, 35:9174–9189, Jun 1987.

[84] Raymond L. Kelly. Program of the 1972 annual meeting of the optical society of america. *J. Opt. Soc. Am.*, 62(11):1336–1336, Nov 1972.

[85] D. B. Murphy. *Fundamentals of Light Microscopy and Digital Imaging*. Wiley-Liss, 2001.

[86] A. R. Goñi, K. Syassen, and M. Cardona. Effect of pressure on the refractive index of Ge and GaAs. *Phys. Rev. B*, 41:10104–10110, May 1990.

[87] A. Venu Gopal, Rajesh Kumar, A. S. Vengurlekar, A. Bosacchi, S. Franchi, and L. N. Pfeiffer. Photoluminescence study of excitonoptical phonon scattering in bulk GaAs and GaAs quantum wells. *Journal of Applied Physics*, 87(4):1858–1862, 2000.

[88] V. A. Karasyuk, D. G. S. Beckett, M. K. Nissen, A. Villemaire, T. W. Steiner, and M. L. W. Thewalt. Fourier-transform magnetophotoluminescence spectroscopy of donor-bound excitons in GaAs. *Phys. Rev. B*, 49:16381–16397, Jun 1994.

[89] Attocube micropositioners, type ANPx101 and ANPz101, with open-loop control.

[90] Alexander Hgele, Stefan Seidl, Martin Kroner, Khaled Karrai, Christian Schulhauser, Omar Sqalli, Jan Scrimgeour, and Richard J. Warburton. Fiber-based confocal microscope for cryogenic spectroscopy. *Review of Scientific Instruments*, 79(2), 2008.

[91] N. H. Bonadeo, A. S. Lenihan, Gang Chen, J. R. Guest, D. G. Steel, D. Gammon, D. S. Katzer, and D. Park. Single quantum dot states

measured by optical modulation spectroscopy. *Applied Physics Letters*, 75(19):2933–2935, 1999.

[92] W. Demtröder. *Laser Spectroscopy.* Springer, 2nd edition, 1998.

[93] T. S. Sosnowski, T. B. Norris, H. Jiang, J. Singh, K. Kamath, and P. Bhattacharya. Rapid carrier relaxation in $In_{0.4}Ga_{0.6}As/GaAs$ quantum dots characterized by differential transmission spectroscopy. *Phys. Rev. B*, 57:R9423–R9426, Apr 1998.

[94] U. Woggon, H. Giessen, F. Gindele, O. Wind, B. Fluegel, and N. Peyghambarian. Ultrafast energy relaxation in quantum dots. *Phys. Rev. B*, 54:17681–17690, Dec 1996.

[95] Shannon O'Leary, Hailin Wang, and John P. Prineas. Coherent zeeman resonance from electron spin coherence in a mixed-type GaAs/AlAs quantum well. *Opt. Lett.*, 32(5):569–571, Mar 2007.

[96] Carey Phelps, Shannon O'Leary, John Prineas, and Hailin Wang. Coherent spin dynamics of donor bound electrons in GaAs. *Phys. Rev. B*, 84:085205, Aug 2011.

[97] L. Allen and J. H. Eberly. *Optical Resonance and Two-Level Atoms.* Dover Publications, 2nd edition, 1987.

[98] R. W. Boyd. *Non-linear Optics.* Academic Press, 3rd edition, 2008.

[99] T. H. Stievater, Xiaoqin Li, T. Cubel, D. G. Steel, D. Gammon, D. S. Katzer, and D. Park. Measurement of relaxation between polarization eigenstates in single quantum dots. *Applied Physics Letters*, 81(22):4251–4253, 2002.

[100] K. L. Silverman, R. P. Mirin, and S. T. Cundiff. Lateral coupling of $In_xGa_{1-x}As/GaAs$ quantum dots investigated using differential transmission spectroscopy. *Phys. Rev. B*, 70:205310, Nov 2004.

[101] V. M. Acosta, K. Jensen, C. Santori, D. Budker, and R. G. Beausoleil. Electromagnetically induced transparency in a diamond spin ensemble enables all-optical electromagnetic field sensing. *Phys. Rev. Lett.*, 110:213605, May 2013.

[102] J. Kobak, T. Smoleski, M. Goryca, M. Papaj, K. Gietka, A. Bogucki, M. Koperski, J.-G. Rousset, J. Suffczyski, E. Janik, M. Nawrocki, A. Golnik, P. Kossacki, and W. Pacuski. Designing quantum dots for solotronics. *Nature Communications*, 5:3191, 2014.

[103] C. Fabry and A. Perot. Sur les franges des lames minces argentes et leur application a la mesure de petites paisseurs dair. *Ann. Chim. Phys.*, 12:459, 1897.

[104] http://mathworld.wolfram.com/probabilitydensityfunction.html.

[105] Ultrasonic bath PowerSonic, model P 500 D/S, manufacturer: Variclean.

Summary

This thesis describes experiments on and theoretical modeling of the coherent optical manipulation of donor-bound electron spins (D^0) in the semiconductor gallium arsenide. Random fluctuations of the nuclear spin polarization in GaAs are the dominant dephasing mechanism for electron spins in this material. We describe and demonstrate an all-optical method to stabilize the nuclear spins and enhance the dephasing time of localized spins.

For the reader with little knowledge of optics or semiconductor physics, we first present a short general section on the interaction of localized electrons with light. The more adept reader might wish to skip it and read the rest of the summary.

Interaction of localized electrons with light

All matter is made of atoms, which consist of a positively charged nucleus with a shell of negatively charged electrons. While the nucleus makes up the bulk of the atom's mass, the electrons are responsible for almost all interesting physical properties. They decide which atoms can bind to form molecules or crystal lattices. In materials where they are mobile, electrons give rise to electricity. The intrinsic magnetic moment of electrons, called the 'spin', determines the majority of a material's magnetic properties. Most relevant for this thesis, however, is the interaction of electrons with light, which determines how materials behave optically.

Light is an oscillation of the electromagnetic field, much like sound is an oscillation of air molecules. Where the frequency of air oscillations determine the pitch of a sound, the frequency of light (i.e.: the photon energy) determines its color. A given material absorbs or reflects light with a certain color if electrons inside can resonate with it, otherwise it transmits that color. Electrons that can move freely, resonate with light over broad frequency bands (this is the reason that metals are opaque or reflective for most colors). Restricting the movement results in more specific resonance frequencies in narrower bands. Entirely localizing (trapping) an electron in an increasingly smaller (nanometer-sized) potential well eventually leads to its energy becoming quantized, i.e. the electron can only attain very specific discrete energies, like the electron energy levels in isolated atoms. Therefore, it will display very sharp resonance peaks, and its dynamics can be carefully controlled if one is able to address the specific resonance frequencies.

Localized electrons come in many flavors and can be made artificially or are naturally present at impurity atoms, crystallographic faults, precipitates and many more. In semiconductors, where the bulk electrons are prohibited to have energies in a certain range (called the energy band gap), additional localized electrons are often energetically isolated from all other electron dynamics in the material. In that case, their quantum mechanical dynamics stay unperturbed for relatively long timescales (nanoseconds or longer). This makes them suitable as a memory for the storage of quantum mechanical information in solid-state matter, which is a fundamental building block for many promising quantum applications, like the quantum computer.

This thesis

In this thesis, we study ensembles of localized electrons in the semiconductor gallium arsenide for their potential as an optical quantum memory. To serve as an optically active quantum memory, a material system has to satisfy two conditions. It should have two long-lived undisturbed eigenstates that serve as the quantum bit and it should have strong interaction with one or more photon fields.

The electrons we study are trapped in the Coulomb potential around substitutional silicon impurity atoms. In their equilibrium ground-state, the only degree of freedom of these donor-bound electrons in GaAs is their spin orientation. In an external magnetic field, the two electron-spin states become degenerate and provide a long-lived two-level qubit. Optical transitions between these spin ground-states and a more complicated excited state (D^0X, with two electrons and a hole) are made by exciting an additional electron-hole pair in the Coulomb potential well.

A high degree of light-matter interaction, which is a prerequisite for deterministic storage of a single photon, can generally be achieved in two ways. The first solution is to incorporate a single quantum emitter in a highly reflective cavity, to enhance the time a photon spends at the position of the quantum system. This approach has grown very effective in the last decades and is preferred by many research groups in both atomic and solid-state optics. The other solution (the one we embraced) is to use ensembles of identical quantum emitters to increase the interaction with photons. If the environment of the ensemble is homogeneous enough, it behaves and can be manipulated as a single quantum system. As this thesis illustrates, a homogeneous ensemble is challenging to realize. However, we believe the relatively cheap and simple fabrication of ensembles, in combination with the growing knowledge on waveguide fabrication, has an important potential for the future upscaling of quantum-mechanical applications and quantum networks on-a-chip.

The storage time or *dephasing time* of localized spins in gallium arsenide (i.e. the time in which the spin is disturbed by its environment to such an extent that its phase is no longer clearly defined) is limited by the magnetic noise of nearby nuclei. Even at cryogenic temperatures and magnetic fields of several Tesla, nuclear spins in gallium arsenide are thermally distributed and show random fluctuations. For a single localized electron spin, temporal fluctuations limit the dephasing time to approximately 15 ns. Spatial fluctuations lower this to 2 ns for large ensembles of localized electron spins.

Multiple techniques have been developed to protect spin-based memory from deterioration by nuclear spin noise. Very successful and often used are spin-echo techniques that periodically flip the direction of the memory spin, to average out the disturbing effect of magnetic noise. However, these methods rely on carefully fabricated and controlled microwave coils and striplines, posing an additional challenge for the scale-up of quantum networks. Motivated by successes of all-optical techniques to improve the dephasing time of electron spins in InAs quantum dots, we developed an all-optical technique to suppress nuclear spin fluctuations around donor-bound electrons in GaAs.

Our technique uses the interplay of *coherent population trapping* (CPT) and *dynamic nuclear polarization* (DNP) to create a negative feedback that stabilizes the nuclear spin polarization. It uses two continuous-wave laser fields and is fully autonomous besides the need for laser intensity and wavelength stabilization. CPT is a two-photon process observed in quantum systems with two ground states and a common excited state, that appears when the difference frequency of two laser fields resonates with the ground-state splitting (a so-called two-photon resonance). At CPT, the absorption of both lasers is suppressed and the ground-state is put in a coherent superposition. Since CPT only appears exactly at two-photon resonance, it can be used to probe the distribution of ground-state splittings in an ensemble.

DNP is the phenomenon of polarizing the nuclear spin through the hyperfine interaction with an electron spin. When the electron spin is optically polarized, it will relax back to thermal equilibrium. In this process, there is a probability that angular momentum is transfered to the nuclear spin. This way, the nuclear spins that surround a localized electron can be polarized both positively and negatively, depending on the sign of the out-of-equilibrium electron-spin polarization. When two lasers are put on two-photon resonance with a detuning from the optical single-photon transitions, CPT yields a non-linear dispersion where small shifts in the ground-state splitting result in a strongly polarized electron spin proportional to these shifts. Nuclear spin fluctuations, influencing the electron-spin splitting through the hyperfine interaction, result in a polarized electron spin, giving rise to DNP with a direction that depends on the sign of the nuclear spin polarization.

In chapter 3 we show theoretically and in experiments how DNP with two lasers at two-photon resonance results in either a single or a double stable configuration for the nuclear spin polarization around D^0, depending on the sign of detuning from the optical transitions. We analyze the relaxation of the tuned nuclear spin environment and show signatures of control over the relaxation rate. In chapter 4, we focus on the blue-detuned case that yields a single stable point for the nuclear spin at zero polarization. We experimentally show a suppression of the nuclear spin fluctuations, doubling the localized electron-spin dephasing time. In order to explain why the enhancement is limited to a factor 2, we analyze the effect of non-uniform driving of ensemble dynamics at two-photon resonance. Due to self-interference of laser light inside the sample and the non-uniform transverse intensity profile of laser beams, ensembles are challenging to address homogeneously. Chapter 5 discusses and shows results of sample design and measurement techniques to obtain a homogeneous ensemble of donor-bound electrons in GaAs that can be addressed by a uniform laser field.

In chapter 6, this thesis also presents an in-depth analysis of the *differential transmission spectroscopy* (DTS) technique that was used to find the optical transitions of the D^0-D^0X complex. We show experiments on donor-bound electrons in GaAs and discuss how DTS enhances the visibility of weakly absorbing transitions. It is also discussed how DTS can provide quantitative information on the optical transition dipole moments and how particular choices in the experimental design minimize systematic errors and the sensitivity to changes in the laser field intensities.

Samenvatting

Deze thesis beschrijft experimenten op en theoretische modellen van de coherente optische manipulatie van elektronenspins gebonden aan donor-atomen (D^0) in de halfgeleider gallium arsenide. Willekeurige fluctuaties van de nucleaire spin polarisatie in GaAs zijn het dominante *dephasing*-mechanisme voor elektronenspins in dit materiaal. Wij beschrijven en demonstreren een volledig optische methode om de nucleaire spin te stabiliseren en daarmee de coherentietijd van gelokaliseerde elektronen te verhogen.

Voor de lezer met beperkte kennis op het gebied van de optica of vaste-stof fysica, presenteren we eerst een korte inleiding in het onderwerp van lichtinteractie met gelokaliseerde elektronen. De ervaren fysicus kan dit gedeelte overslaan.

Interactie van gelokaliseerde elektronen met licht

Alle materie is opgebouwd uit atomen, die op hun beurt bestaan uit een positief geladen atoomkern met een negatief geladen schil van electronen. Hoewel de atoomkern bijna het volledige gewicht van een atoom bepaalt, zijn de electronen verantwoordelijk voor vrijwel alle interessante fysische eigenschappen. Ze bepalen welke atoomsoorten kunnen binden tot moleculen en kristalroosters. In materialen waarin elektronen vrij kunnen bewegen, is hun lading de oorzaak van elektriciteit. Hun intrinsieke magnetische moment, de 'spin', zorgt voor het gros van magnetische materiaaleigenschappen. Voor dit proefschrift is echter het meest relevant, dat elektronen interacteren met licht, en zodoende bepalen hoe stoffen zich optisch gedragen.

Licht beweegt als een trilling door het elektromagnetisch veld, zoals geluid zich als een akoestische trilling van luchtdeeltjes door de lucht beweegt. Waar de trillingfrequentie van geluid de toonhoogte bepaalt, definieert de trillingfrequentie van licht (ofwel de energie van de fotonen) de kleur. Of een materiaal een bepaalde kleur licht absorbeert of doorlaat, hangt ervan af of elektronen in het materiaal met dezelfde frequentie als het licht kunnen resoneren, en zodoende effectief energie uit de lichtstraal kunnen overnemen. Elektronen die vrij kunnen bewegen, resoneren met licht over een grote bandbreedte (dit is de reden dat metaal de meeste kleuren licht reflecteert). Wanneer de bewegingsvrijheid van een elektron belemmerd wordt, kan het elektron slechts resoneren met licht in nauwe frequentiebanden. Als het elektron volledig gelokaliseerd wordt (gevangen raakt) in een gebied ten grootte van ongeveer een nanometer leidt dit tot quantisatie van de elektronenergie. Dit wil zeggen dat het elektron slechts hele specifieke trillingsenergieën kan hebben, net als de elektronen in een geïsoleerd atoom. Hierdoor heeft het elektron zeer scherpe resonantiepieken, en kan de trillingsmodus van het elektron met precisie gecontroleerd worden, mits het met exact de juiste kleur licht beschenen wordt.

Gelokaliseerde elektronen zijn er in vele kleuren en smaken. Ze kunnen kunstmatig aangebracht worden, maar zijn ook van nature aanwezig bij stapelfouten of vreemde atomen in kristalroosters, bij microscopische gebieden van één soort atoom in een materiaal van een andere soort, etcetera. In halfgeleiders is het voor elektronen onmogelijk om een energie te hebben in een gebied dat de *bandgap* wordt genoemd. Hierdoor zijn extra gelokaliseerde elektronen energetisch geïsoleerd van alle andere elektronen in dit materiaal. In dat geval wordt de trilling van het elektron nauwelijks verstoord en blijft de quantummechanische toestand van die trilling veel langer leven dan gewoonlijk, tot periodes langer dan een nanoseconde. Dit maakt gelokaliseerde elektronen zeer bruikbaar als opslag voor quantummechanische informatie, wat een fundamenteel onderdeel is van veel quantumtoepassingen, zoals de quantumcomputer.

Deze thesis

In deze thesis bestuderen we ensembles van gelokaliseerde elektronen in de halfgeleider gallium arsenide als potentieel medium voor een optisch gecontroleerde quantumopslag. Een geschikte optisch gecontroleerde quantumopslag beschikt over twee eigenschappen. Ten eerste dient het twee eigentoestanden te hebben die niet snel vervallen naar andere toestanden, om te dienen als quantum bit. Ten tweede moet het systeem sterke interactie hebben met één of meer fotonvelden.

De elektronen die wij bestuderen zitten gevangen in een Coulomb potentiaal rondom een substitutioneel silicium dopingatoom. In de energetisch laagste toestand, tevens de evenwichtstoestand, is de enige vrijheidsgraad van het elektron de oriëntatie van de elektronenspin. In een extern aangelegd magneetveld splitst de spintoestand in tweeën, wat ons de gewenste twee-level quantum bit oplevert.

Optische overgangen kunnen worden gemaakt tussen deze twee grondtoestanden en een meer complexe aangeslagen toestand (D^0X, bestaande uit twee elektronen en een gat).

Een hoge mate van interactie tussen materie en licht - voorwaarde voor deterministische opslag van enkele fotonen - kan bereikt worden op twee manieren. De eerste manier is het plaatsen van het materiële quantumsysteem in een holte waarin het licht heen en weer kaatst, waardoor de interactietijd van het foton met het quantumsysteem wordt verhoogd. Deze benadering is de afgelopen decennia geperfectioneerd en wordt veelvuldig gebruikt in zowel de atomaire als vaste-stof fysica. De andere manier (onze keuze) is het gebruik van ensembles van identieke quantumsystemen om de interactie met licht te verhogen. Indien de omgeving van het ensemble homogeen is, gedraagt het zich als een enkel quantum systeem en kan het als zodanig gemanipuleerd worden. Zoals deze thesis beschrijft, is het lastig om een volledig homogeen ensemble te realiseren. Wij geloven echter dat de relatief goedkope en simpele fabricage van ensembles, in combinatie met de groeiende expertise op het gebied van golfgeleiders, een belangrijke rol kan spelen in het opschalen van quantummechanische toepassingen en quantum netwerken op een enkele chip.

De opslagtijd of *dephasing* tijd van gelokaliseerde spins in gallium arsenide (dat is de tijd waarin een spin zodanig door zijn omgeving wordt verstoord dat de fase niet meer goed gedefinieerd is) wordt gelimiteerd door de magnetische ruis van nabije nuclei. Zelfs bij temperaturen dichtbij het absolute nulpunt en een magnetisch veld van meerdere Tesla's is de nucleaire spin thermisch verdeeld en vertoont het willekeurige fluctuaties. Voor een enkele gelokaliseerde elektronenspin zorgen fluctuaties in de tijd voor een dephasing tijd van ongeveer 15 ns. Fluctuaties over afstand verlagen dit getal nog verder voor ensembles tot 2 ns.

Er zijn verschillende technieken ontwikkeld om op spin gebaseerde quantum opslag te beschermen tegen verstoring door nucleaire spinruis. Zeer succesvol en veelgebruikt zijn zogeheten spin-echo technieken, waarbij de oriëntatie van de opslagspin periodiek gespiegeld wordt om het effect van magnetische ruis weg te middelen. Echter, dit soort technieken vereisen de fabricage en controle van microgolfspoelen op zeer kleine schaal, wat een extra complicerende factor is bij het opschalen van netwerken met zeer veel interacterende quantumsystemen. Gemotiveerd door successen in het volledig optisch verbeteren van de spin dephasing tijd in InAs quantum dots, hebben we een volledig optische methode ontwikkeld om de nucleaire spin fluctuaties rondom gelokaliseerde elektronen in GaAs te onderdrukken.

Onze techniek maakt gebruik van de wisselwerking tussen *coherent population trapping* (CPT) en *dynamic nuclear polarization* (DNP) om een negatieve terugkoppeling te creëren die de nucleaire spinpolarisatie stabiliseert. Het maakt gebruik van twee continuous-wave lasers en is volledig autonoom afgezien van de noodzaak om laser intensiteit en golflengte constant te houden. CPT is een twee-foton proces dat ontstaat in quantumsystemen met twee grondtoestanden met een gezamenlijke aangeslagen toestand wanneer de verschilfrequentie van de twee laservelden resonant is met de overgang tussen de twee grondtoestanden (een zogeheten twee-fotonresonantie). Op CPT resonantie wordt de absorptie van beide lasers onderdrukt en komt het quantumsysteem in een coherente superpositie van de twee grondtoestanden terecht. Omdat CPT alleen precies op twee-fotonresonantie verschijnt, kan het gebruikt worden om de waarschijnlijkheidsverdeling van overgangsfrequenties tussen de grondtoestanden bloot te leggen.

DNP is de verzamelterm voor processen waarbij de nucleaire spin wordt gepolariseerd via de hyperfijn interactie met een elektronenspin. Wanneer de elektronenspin optisch gepolariseerd wordt, zal het terugvallen naar de evenwichtstoestand. In dit verval is er een kans dat het impulsmoment wordt overgedragen aan de nucleaire spin. Op deze manier kan de nucleaire spin rondom gelokaliseerde elektronen in beide richtingen gepolariseerd worden, afhankelijk van het teken van de elektronenspinpolarisatie. Wanneer twee lasers de twee-fotonresonantie aandrijven, maar niet geheel resonant (*detuned*) zijn met de optische overgangen, onstaat er een non-lineaire dispersie waarbij kleine veranderingen in de splitsing van de grondtoestand een sterk gepolariseerde elektronenspin tot gevolg hebben.

In hoofdstuk 3 laten we theoretisch en experimenteel zien hoe DNP met twee lasers op twee-fotonresonantie resulteert in een enkele of een dubbele stabiele toestand voor de nucleaire spinpolarisatie rondom D^0, afhankelijk van de richting van detuning met de optische overgangen. We analyseren het verval van de gemanipuleerde nucleaire spin omgeving en laten aanwijzingen zien voor de controle van dat verval. In hoofstuk 4 richten we ons op het geval waarbij er één enkele stabiele toestand voor de nucleaire spin is. We laten experimenteel een ondrukking van de nucleaire spinruis zien, waarbij de dephasing tijd van de gelokaliseerde elektronenspins verdubbelt. Om te verklaren waarom deze verbetering slechts een factor twee is, analyseren we wat er gebeurt wanneer een elektronensemble niet uniform wordt aangedreven. Doordat laserlicht door reflecties met zichzelf interfereert en van nature een niet-uniforme transversale intensiteitsverdeling heeft, is het lastig om ensembles homogeen te adresseren. Hoofdstuk 5 bediscussieert en laat resultaten zien van sample-ontwerp en meettechnieken voor het verkrijgen van homogene ensembles van gelokaliseerde elektronen in GaAs die met een uniforme laserintensiteit beschenen kunnen worden.

In hoofdstuk 6 presenteren we verder een gedetailleerde analyse van de *differentiële transmissie spectroscopie* (DTS) techniek die gebruikt is voor het in kaart brengen van de optische overgangen in het D^0-D^0X complex. We laten experimentele resultaten zien en bediscussiëren hoe DTS de zichtbaarheid van zwak absorberende overgangen vergroot. Er wordt tevens uitgelegd dat DTS quantitatieve informatie kan verschaffen over de transitie dipoolmomenten en hoe bepaalde keuzes in de experimentele opzet systematische fouten en de gevoeligheid van de meting voor veranderingen in de laserintensiteit verminderen.

Acknowledgments

And suddenly it is there: the end of four-and-a-half years of lab building, measuring, failing equipment, making optimistic schedules, diverting from them within a week, motivation, discouragement, hope, despair, results and finally: a manuscript. It turned out differently from what I expected, but I am satisfied with it. It required some perseverance from my side, but it made a world of difference that I got support from some wonderful people, whom I will try to thank here.

First of all, I want to thank prof. Caspar van der Wal for his supervision and guidance. The often-heard complaint "my supervisor does not have time for me" is completely unknown to me. Caspar, your patience and positive attitude make you a very pleasant person to work for. At times where I got disappointed with research, you were always able to motivate me and make me appreciate my own competences.

To the first three people to fully read my manuscript - prof. Mete Atatüre, prof. Pepijn Pinkse and prof. Ronnie Hoekstra: thank you for taking precious time of your schedules to judge my dissertation. The knowledge that you would be reading this was a big motivation to cross the t's and dot the i's. I hope you enjoyed it.

Good equipment is a prerequisite for research, but the right team to operate it is far more important, and I was very lucky with the co-workers I had. Sander and Danny, the periods where we worked together in the lab were among the best times during my PhD. Combining our different skill sets to perform and interpret challenging experiments felt like being in an episode of the A-team. Alok, thank you for transferring some of your magic touch to me. Only you can truly appreciate the love/hate relationship I have with our laser setup. Olger, it was a great pleasure to be your scientific twin-brother. Just as your name, you are one-of-a-kind. Your sense of humor and ability to take a joke made our scientific trips together very memorable, with our road trip in Colorado being the climax. Good luck in Eindhoven at ASML! Gerjan, good luck with taking over Olger's beast, I believe you will take good care of it. Xu, you are one of the most likable persons I have ever met. Keep practicing your Dutch, you will get flawless.

During my project, I had the pleasure to be the daily supervisor of some very clever students in their bachelor and master research projects. Paul, Sébastien, Urvashi, Carmen, Henry, Feitze and Maarten, I hope I was able to help you as much as you helped me. Those of you who will continue their scientific career with a PhD, I wish a lot of students. Teaching and motivating others is very satisfactory, and students' fresh insights and sharp questions are vital to a healthy scientific group.

Keeping scientific labs running, requires technical coherence on timescales longer than a PhD project. Luckily, continuous knowledge is maintained through the minds and hands of our technicians: Johan, Bernard, Martijn, Tom and Herman, thank you for making my life a lot easier. Sorry for all the tools I returned too late. Wigger 'the wizard' Jonker, you never failed to amaze me with your intuition for electronics. You really deserve the nickname we secretly gave you. Thanks also to Duc Van Nguyen from SRON, the sapphire samples work quite well.

In general, my time at Physics of Nanodevices was very enjoyable, thanks to the pleasant, cooperative atmosphere. Such a positive atmosphere is fragile and can only be sustained by a collective effort of everyone involved, by helping each other when needed and by keeping feedback constructive. For these efforts I want to thank everyone currently and formerly in the group: prof. Bart van Wees, prof. Tamalika Banerjee, prof. Caspar van der Wal, Anna, Johan, Bernard, Martijn, Tom S., Herman, Jasper, Sander O., Alok, Sander K., Olger, Xu, Gerjan, Saurabh R., Sid, Juan, Arijit, Javaid, Gaurav, Ivan, Paul, Niko, Alexei, Subir, Timo, Danny, Aisha, Madhu, Ludo, Kumar, Mallik, Pep, Christian, Jing, Roald, Eric, Crystal, Talieh, Tom B., Michael, Saurabh S., Diederik and many others.

Thanks to our collaborators from Ruhr-Universität Bochüm - prof. Andreas Wieck, prof. Dirk Reuter, Arne Ludwig and Sascha Valentin - for their samples and quick responses to emails regarding fabricational issues and solid-state physics.

To the gentlemen of DSB, thanks for the pulleys and the grebe. I don't know what I would have done without them.

Mam en pap, your love and support have been invaluable. Thank you for exciting and stimulating my curiosity during my childhood, and for teaching me how to deal with life.

But most of all, I want to thank my wife, Fransien. Lieve Fran, if we had never

met, I would still be finishing my bachelor research. Throughout the years, you have become part of my conscience and motivation. Life is easier when you know yourself supported by a beautiful mind that thinks along with you. Dankjewel.

Jakko de Jong
Groningen, 16 September 2016

Curriculum Vitae

Jakko de Jong

18 May 1986	Born in Deventer, The Netherlands
1998-2004	Stedelijk Gymnasium Arnhem, Arnhem, The Netherlands
2004-2009	B.Sc. Applied Physics, Rijkuniversiteit Groningen Groningen, The Netherlands
2009-2011	M.Sc. Applied Physics, Rijkuniversiteit Groningen Groningen, The Netherlands
2012-2016	Ph.D. research at the Zernike Institute for Advanced Materials, University of Groningen, The Netherlands, under the supervision of prof. dr. ir. C. H. van der Wal. Subject: Optically addressing semiconductor electron-spin ensembles with tunable nuclear-spin environments.

List of publications

1. *Homogeneous GaAs epilayers for optical experiments: correlations between strain, spectroscopy and microscope imaging.* J. P. de Jong, A. R. Onur, M. Degen, D. Reuter, A. D. Wieck, C. H. van der Wal, *in preparation* (2016).

2. *Self-improving coherent population trapping by suppressing nuclear spin fluctuations around donor-bound electrons in GaAs.* J. P. de Jong, A. R. Onur, D. O'Shea, M. Degen, D. Reuter, A. D. Wieck, C. H. van der Wal, *in preparation* (2016).

3. *Stabilizing nuclear spins around semiconductor electrons via the interplay of optical coherent population trapping and dynamic nuclear polarization.* A. R. Onur*, J. P. de Jong*, D. O'Shea, D. Reuter, A. D. Wieck, C. H. van der Wal, *Physical Review B* **93**, 161204(R) (2016).

4. *Analysis of optical differential transmission signals from co-propagating fields in a lambda system medium.* J. P. de Jong, A. R. Onur, D. Reuter, A. D. Wieck, C. H. van der Wal, submitted (2014); available at arXiv:1409.7679.

5. *Odd and even Kondo effects from emergent localization in quantum point contacts.* M. J. Iqbal, Roi Levy, E. J. Koop, J. B. Dekker, J. P. de Jong, J. H. M. van der Velde, D. Reuter, A. D. Wieck, Ramón Aguado, Yigal Meir, C. H. van der Wal, *Nature* **501**, 79 (2013).

6. *Split-gate quantum point contacts with tunable channel length.* M. J. Iqbal, J. P. de. Jong, D. Reuter, A. D. Wieck, C. H. van der Wal, *Journal of Applied Physics* **113**, 024507 (2013).

7. *Thin film solar concentrators: simulations on geometric optimization* [translated from Dutch]. J. P. de Jong, *PCN Fotonica Magazine* 36e jaargang 4, pp. 17-21, (2011) (professional technical society journal).

* *Equal contributions*